DEVELOPMENT OF FUNCTIONAL NANOPARTICULATE MATERIALS:

Examination of the Functional and Structural Properties of Nanoparticulate Metal Complexes Prepared by Precipitation with Compressed Antisolvent Technology

by

Joseph G. Nguyen

Bachelor of Science in Chemistry
Creighton University, Omaha, NE, 2000
Master of Science in Education
Indiana University, Bloomington, IN, 2002

Submitted to the Department of Chemistry and the Faculty of the Graduate School of the University of Kansas in partial fulfillment of the requirements for the degree of Doctor of Philosophy

A. S. Borovik (Co-Advisor)

Cindy L. Berrie (Co-Advisor)

Heather Desaire

Robert C. Dunn

Bala Subramaniam

Date Defended: September 2, 2008

The Dissertation Committee for Joseph G. Nguyen certifies
that this is the approved version of the following dissertation:

DEVELOPMENT OF FUNCTIONAL NANOPARTICULATE MATERIALS:

Examination of the Functional and Structural Properties of Nanoparticulate Metal Complexes Prepared by Precipitation with Compressed Antisolvent Technology

A. S. Borovik (Co-Advisor)

Cindy L. Berrie (Co-Advisor)

Heather Desaire

Robert C. Dunn

Bala Subramaniam

Date Approved: September 3, 2008

ABSTRACT

Joseph G. Nguyen

Department of Chemistry, University of Kansas, September 2008

A diverse set of systems that interact with nitric oxide (NO) is important because of its adverse role in environmental chemistry and importance in mammalian biology. Towards this effort, nanomaterials that interact with NO have been developed because they can display beneficial and unique chemical and physical properties from their larger counterparts. While several nanomaterials have been developed that store and release NO, few systems composed entirely of metal complexes have been reported. The research described in this dissertation involves the development of nanomaterials that interact with NO. Molecule-based nanoparticulate metal complexes were prepared using precipitation with compressed antisolvent technology. Microscopy and powder x-ray diffraction were used to determine that the nanoparticles form lamellar structures during processing. These nanoparticulates also displayed enhanced reactivity towards NO and O_2 compared to their unprocessed analogs. The preparative routes towards the synthesis of immobilized metal complexes within silica particles are also discussed.

ACKNOWLEDGEMENTS

My success was a direct result of the support and words of encouragement coming from many people. First and foremost, I would like to thank my research advisor, Professor Andy Borovik, for his guidance and encouragement. I greatly appreciate the confidence he showed by allowing me to work on a new project. Always an educator, he has been an excellent role model and has provided several opportunities for me to be a better chemist and educator in my own right. If I become half the educator he is, success will definitely be in my future.

I would like to thank Dr. Chad Johnson and Professor Bala Subramaniam for a very successful collaboration. I appreciate all of our discussions, and I am especially grateful to Chad for his determination and hard work. In addition, I would like to thank Professor Reg Penner for taking time out of his busy schedule to talk about my science and provide helpful advice. I would also like to thank Dr. Jian-Guo Zheng, the Director of Nanomaterials Characterization and Fabrication Facility at the University of California – Irvine, Fan Yang, David Taggart, and Dr. Megan Bourg for their assistance in my microscopy studies, and ShengChin Kung for his assistance in my diffraction studies.

I have been fortunate to have the opportunity to work with some great people during my graduate career. Thanks to Dr. Leilani Zart (Welbes) and Tim Reed for taking the time to train me during my first few months in lab. Thanks to Dr. Paul Zinn for his countless suggestions concerning my project and endless enthusiasm for science – our conversations have always been great. Thanks to Ryan Shook and Dr. Meng-Yin "Billy" Yang, without your help, who knows how my dissertation would have turned out. I would also like to thank the other members of the Borovik and Subramaniam research groups for their help and friendship, especially Trenton Parsell and Drs. Sarika Sharma, Jhumpa Mukherjee, and Sara Palavicini. Finally, I would like to thank my undergraduate advisor, Professor Bruce Mattson at Creighton University, for being an inspiration and providing me some valuable advice.

I would like to thank the faculty and staff of the Departments of Chemistry at both the University of Kansas and the University of California – Irvine. I greatly appreciate my committee members, Professors Cindy Berrie, Heather Desaire, and Bob Dunn for agreeing to serve on my Final Defense Committee. My work could not be accomplished without the financial support from the National Science Foundation and the University of California – Irvine.

My success is a direct result of the tremendous support that I received from my family. My parents are the ultimate example of love because they have sacrificed their lives for their children to succeed. Since my siblings and cousins have always supported all of my decisions, they helped me build a foundation for all of my accomplishments. Even though my grandparents, aunts, uncles, and wife's family

might not have always understood all my decisions, they have always supported me in furthering my education, and I hope I have made them proud.

Finally and definitely not least, I want to thank my wife, Heather, for her flexibility and patience while I finished my degree at KU. She really did not want to move to California, but I thank her for having faith and "modifying" her plans in order for me to finish my schooling. Without her, I would not have been able to accomplish quite as much. She is my heart and soul, and I can never thank her enough.

Thành đạt mà tôi có được là do sự hỗ trợ lớn lao từ gia đình. Ba mẹ của tôi là một ví dụ điển hình về lòng thương con vì họ đã hy sinh cả cuộc đời để con cái được thành đạt. Các anh chị em của tôi luôn luôn hỗ trợ những quyết định của tôi. Tuy rằng ông bà, cô dì, chú bác và gia đình bên vợ có thể đã không luôn luôn hiểu rõ những quyết định của tôi, họ luôn hỗ trợ và động viên tôi tiến tới trên con đường học vấn, và tôi hy vọng rằng tôi đã làm họ tự hào.

Cuối cùng, tôi muốn cảm ơn Heather, người vợ yêu quý của tôi, đã kiên nhẫn và bền bĩ theo tôi khi tôi đang học ở Đại Học Kansas. Heather không muốn dọn về Cali lắm, nhưng tôi cảm ơn nàng đã tin tưởng và 'thay đổi' kế hoạch để tôi được làm xong luận án. Không có nàng, tôi khó có thể đạt được mọi thứ. Nàng là con tim và tinh thần của tôi, và tôi rất biết ơn nàng.

Dedicated to my parents with love.

They have sacrificed a lot of time and money

to give their children opportunities they never had.

Đề tặng ba mẹ với cả tình thương.

Ba mẹ đã hy sinh rất nhiều thời gian và tiền

bạc để các con có được những cơ hội chưa bao giờ có.

TABLE OF CONTENTS

LIST OF FIGURES

LIST OF SCHEMES

LIST OF TABLES

CHAPTER ONE

INTRODUCTION

Research into the chemistry of nitric oxide (NO) has increased greatly because of its importance in environmental chemistry and mammalian biology. There is ample evidence that a diverse set of systems is necessary to meet these many demands. Nanomaterials with size-dependent physical and chemical properties have shown promise in industrial and biotechnological applications. As such, the purpose of my research was to develop nanomaterials that interact with NO and study their chemical and physical properties.

Physical and Chemical Properties of Nitric Oxide

Nitric oxide (NO) is a simple, diatomic radical possessing unique and fascinating chemistry. It is a colorless gas at room temperature and pressure with a boiling point at 121 K.[1-2] The solubility of NO in water is slightly higher than dioxygen in water, but like O_2, it is more soluble in organic solvents.[2-3] Thus, the rates of NO reactions can be dramatically increased in hydrophobic environments, such as lipid membranes, compared to water.

Nitric oxide is highly reactive with halogens and species with unpaired electrons because of its radical nature.[2-3] The unpaired electron in this molecule resides in a π^* antibonding orbital (Figure 1-1), and molecular orbital theory predicts a net bond order of 2.5. The bond order is consistent with its bond length of 1.154 Å,

which is between those of N_2 (1.06 Å) and O_2 (1.18 Å).[2-3] With an electron in the π^* antibonding orbital, NO can easily be oxidized to the nitrosonium ion (NO^+) and possibly reduced to NO^-. As each electron is added going from NO^+ to NO^- decreases the bond order, which is reflected in the serially increasing bond lengths and decreasing vibrational energies (Table 1-1).[4] Thus, measurement of these properties provides a means to assess the character of nitrosyl groups in compounds containing NO.

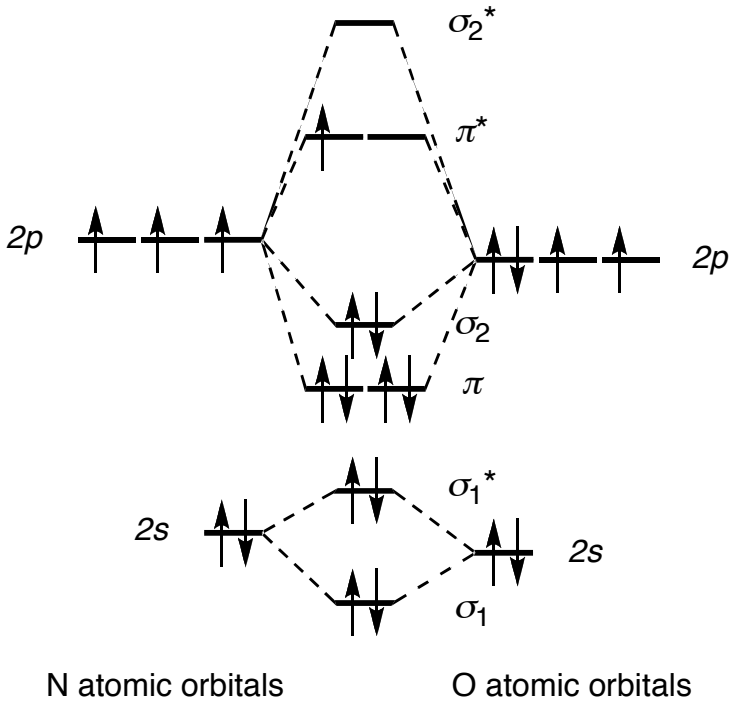

Figure 1-1. Molecular orbital diagram for NO.

Table 1-1. Properties of nitrogen monoxides.[4]

Molecule	Nitrogen oxidation number	Bond length (Å)	N—O stretch (cm^{-1})
Nitrosonium (NO^+)	+3	0.95	2300
Nitric oxide (NO)	+2	1.15	1840
Nitroxyl anion (NO^-)	+1	1.26	1290

Environmental Significance of Nitric Oxide and Other Nitrogen Oxides

For more than 200 years, three different oxides of nitrogen have been known.[1] Nitric oxide, nitrogen dioxide (NO_2), and nitrous oxide (N_2O) all have adverse effects on the environment.[5] Both NO and NO_2, which are jointly referred to as NO_X, are reactive radicals that are major components of pollution. The main source of NO_X emissions come from combustion processes in fossil fuel power stations, motor vehicles, and domestic combustion appliances.[5] Nitrous oxide, an anesthetic popularly known as laughing gas, is relatively chemically inert but contributes to the greenhouse effect because it is a strong infrared absorber.[5b]

Nitric oxide is a colorless, odorless gas and makes up at least 90% of NO_X emissions.[5] As an active free radical, it will readily oxidize to NO_2 by oxidants such as dioxygen (O_2) (Equation 1-1) and ozone (O_3) (Equation 1-2). When the concentration of NO is greater than 1 ppm, oxidation by O_2 occurs very quickly.

$$2NO + O_2 \rightarrow 2NO_2 \qquad (1\text{-}1)$$

$$NO + O_3 \rightarrow NO_2 + O_2 \qquad (1\text{-}2)$$

However, oxidation by ozone predominately occurs at concentrations less than 1 ppm, such as in the upper troposphere and stratosphere.[5] Ozone depletion from the troposphere creates a problem because O_3 is needed to absorb UV radiation and reduce solar heating, which is harmful to life on earth. Equation 1-3 shows that NO will react with hydroperoxy radicals (HO_2•) to form both NO_2 and hydroxyl radicals (•OH), which are highly reactive molecules in the lower atmosphere and change the chemical properties of many pollutants.[5] For example, hydroxyl radicals will react

with hydrocarbons to produce organic peroxy radicals (RO_2•), which then will also oxidize NO to NO_2 (Equation 1-4).

$$NO + HO_2\bullet \rightarrow NO_2 + \bullet OH \qquad (1\text{-}3)$$

$$NO + RO_2\bullet \rightarrow NO_2 + RO\bullet \qquad (1\text{-}4)$$

Nitrogen dioxide is a corrosive and highly oxidizing reddish-brown gas with a pungent odor. While only 5-10% of NO_X emissions are composed of NO_2, the major source of it comes from the rapid oxidation of NO.[5] Its reddish-brown color contributes to the discoloration and reduced visibility of polluted air, and it is an efficient absorber of ultraviolet and visible light. The photolysis of NO_2 leads to the production of NO (Equation 1-5) and eventually ozone (Equation 1-6, where M is any small molecule).[5] Production of O_3 in the lower troposphere contributes to

$$NO_2 + h\upsilon \rightarrow NO + O \qquad (1\text{-}5)$$

$$O + O_2 \xrightarrow{M} O_3 \qquad (1\text{-}6)$$

photochemical smog and the greenhouse effect, which are enhanced in urban areas due to the presence of hydrocarbons.[5] Nitrogen dioxide also contributes to the acidification of rain because it can readily be transformed to nitric and nitrous acid with water and OH (Equations 1-7 through 1-9).

$$2NO_2 + H_2O \rightarrow HNO_3 + HNO_2 \qquad (1\text{-}7)$$

$$NO_2 + OH \xrightarrow{M} HNO_3 \qquad (1\text{-}8)$$

$$NO_2 + NO + H_2O \rightarrow 2HNO_2 \qquad (1\text{-}9)$$

Unfortunately, over 30 million tons of NO_X gases are vented to the atmosphere each year,[6] an amount that has increased at least 4% per year since

1950.[5b] These NO_X gases contribute to the greenhouse effect by increasing the production of ozone in the lower troposphere. In the lower stratosphere, NO_X gases are directly and indirectly blamed for the loss of approximately 50% of the ozone layer.[5b] NO_X gases are predicted to have a greater global warming effect than CO_2.[5b] Overall, its continued increase could negatively effect ecosystems, cause corrosion and erosion, and could be detrimental to the wildlife in streams and lakes. Therefore, it is important to develop methods or systems for the removal of NO_X emissions.

Systems for Controlling NO_X Emissions

The two approaches for removing NO_X from the atmosphere are to either treat it at the source of emission or not to produce it at all. Efforts to modify combustion processes have reduced, but not eliminated, NO_X emissions.[5b] On the other hand, a number of commercial approaches for NO_X removal have proven to be more effective.[5] These commercial approaches include adsorptive, thermal, and catalytic systems. Among these systems, the best approach is selective catalytic reduction (SCR) with ammonia (NH_3) because it provides the best balance of economic, technical, and regulatory concerns.[5b, 6] Some plants utilizing SCR have shown to reduce 80-90% of NO_X emissions.[5b]

Equation 1-10 shows the simplest equation for the reduction of NO_X by SCR and normally operates at temperatures between 300 and 400 °C.[5b, 6] Despite its success, SCR has several problems that limit its effectiveness. The use of anhydrous NH_3 requires a sophisticated distribution system of pipes and nozzles to store and deliver anhydrous NH_3 to react with NO_X. Also, about 5-20 ppm of unreacted NH_3,

another pollutant, is released into the atmosphere.[6] Other reductants, such as H_2, CO, C, and hydrocarbons, are not very cost effective.[5b, 6-7]

$$4NO + 4NH_3 + O_2 \xrightarrow{cat} 4N_2 + 6H_2O \qquad (1\text{-}10)$$

$$NO \xrightarrow{cat} \tfrac{1}{2}N_2 + \tfrac{1}{2}O_2 \qquad (1\text{-}11)$$

A highly desirable approach for the removal of NO_X involves the direct decomposition of NO into its elements (Equation 1-11) because it does not require the use of a reductant. Researchers have studied the use of zeolites for the decomposition of NO for over 40 years; zeolites are hydrated aluminosilicate materials with a microporous structure that can accommodate a variety of cations.[8] However, it was not until 1981 when the direct disproportionation of NO over Cu-zeolites was reported.[9] These zeolites were not sufficiently active for practical use, but several researchers have tried to develop different ion-exchanged zeolites to obtain better results.[10] These ion-exchanged zeolites successfully disproportionated NO without the use of a reductant, but most of them required elevated temperatures.

Clearly, there are enormous health and economic benefits for new technologies that eliminate NO_X emissions. Any new technology that offers acceptable solutions for the elimination of NO_X emissions in power plants has a potential to generate billions of dollars of business.[6] It would also be beneficial to develop commercial technology to eliminate NO_X emissions from motor vehicles because none are currently available. The catalytic decomposition of NO into its elements provides the cleanest and most direct approach to NO_X removal, but new combustion or chemical process technologies that do not co-produce NO_X are even

more highly desirable. No matter how difficult the approaches, it is extremely important to develop a method for the elimination of NO_X emissions.

Biological Significance of Nitric Oxide

Nitric oxide has been used as a probe to study the ligand environment in metalloproteins for almost 150 years because it can function as an electron donor or an electron acceptor.[11] However, to the surprise of the biological community, this toxic molecule is one of the most ubiquitous substances in mammals. The versatility of NO was not realized until it was discovered that mammalian cells synthesized it in the 1980s.[3, 11] Shortly after it was discovered, researchers discovered that NO is involved in an astonishing array of critically important physiological and pathophysiological functions.[3, 11]

As one of the most widespread signaling molecules in biology, NO plays a major role in a wide variety of cellular and organ functions in the body.[3] These functions can be separated into three categories including regulatory, protective, and cytotoxic.[12] Among the many regulatory functions, NO helps control vascular tone and permeability, cellular adhesion, and renal function. NO plays a role within the immune system and also functions as a neurotransmitter, bronchodilator, and inhibitor of platelet adhesion and aggregation. As a protective molecule, it inhibits cell inflammatory activity and acts as an antioxidant by neutralizing oxidants associated with oxidative stress such as hydrogen peroxide, alkyl hydroperoxides, and superoxide. Generally, the concentration of NO required to mediate the protective effects are in the picomolar to nanomolar range.[13] Higher concentrations of NO make

it highly cytotoxic in the presence of other cytotoxic agents such as superoxide, heavy metals, alkylating agents, and radiation.[12-13] Under these conditions, NO can induce DNA damage and lipid peroxidation.

Since NO participates in multiple physiological roles, defects in the NO pathway lead to the development of various pathophysiological states. Some of these disorders include hypertension, atherosclerosis, coronary artery disease, stroke, impotence, and vascular complications in diabetes mellitus.[3] Excess NO has also been implicated in other diseases such as Parkinson's Disease, multiple sclerosis, rheumatoid arthritis, and glaucoma.[14] It is evident from the varied biological effects, disorders, and diseases that the development of novel systems for both the release and scavenging of NO is highly desirable.

Systems for the Storage and Release of Nitric Oxide

Nearly all pharmaceutical companies have established research and development programs for the discovery of new therapeutic strategies for the storage and delivery of NO.[3] When developing an NO-donor system, it is important that it can locally release NO since the sphere of influence of NO is approximately 100 μm.[13] NO-delivery systems should also only release NO to prevent any formation of toxic by-products; otherwise, the by-products should be proven to be non-toxic.

A few examples of current systems that store and release NO are shown in Figure 1-2.[13, 15] Organic nitrates are the most commonly studied and used NO-releasing drugs; they are also one of the few classes of drugs that have been approved for clinical use. Nitroglycerin has been used to relieve angina pectoris and acute

myocardial infarction for over a hundred years; however, the main limitation of organic nitrates is the development of tolerance with prolonged continuous use.[13, 15] Another clinically relevant NO-donor drug is sodium nitroprusside, a potent NO dispenser, and it is used to rapidly lower the blood pressure in hypertensive crises.[13,15] Unfortunately, sodium nitroprusside has to be delivered intravenously because it is ionic in nature.[15] Another limitation of sodium nitroprusside is that it produces toxic, free cyanide ions (CN^-).[13, 15]

A promising class of drugs is anionic diazeniumdiolates (X—[N(O)NO]).[13, 15] These diazeniumdiolates can spontaneously release 2 equivalents of NO under physiological conditions, and NO-release rates can be controlled by varying X. Even though diazeniumdiolates have shown promise for the treatment of certain cancers, the toxicity of the by-products still need to be confirmed.[13] Another promising class of drugs is *S*-nitrosothiols because they are naturally occurring NO donors.[13, 15] They are considered to be NO^+ donors, which makes them less susceptible to conditions of oxidative stress. Modification of the environment around the parent thiol can lead to several means by which *S*-nitrosothiols can release NO. A major limitation of the early forms of *S*-nitrosothiols is that they rapidly decompose in an unpredictable manner in the presence of trace Cu^+.

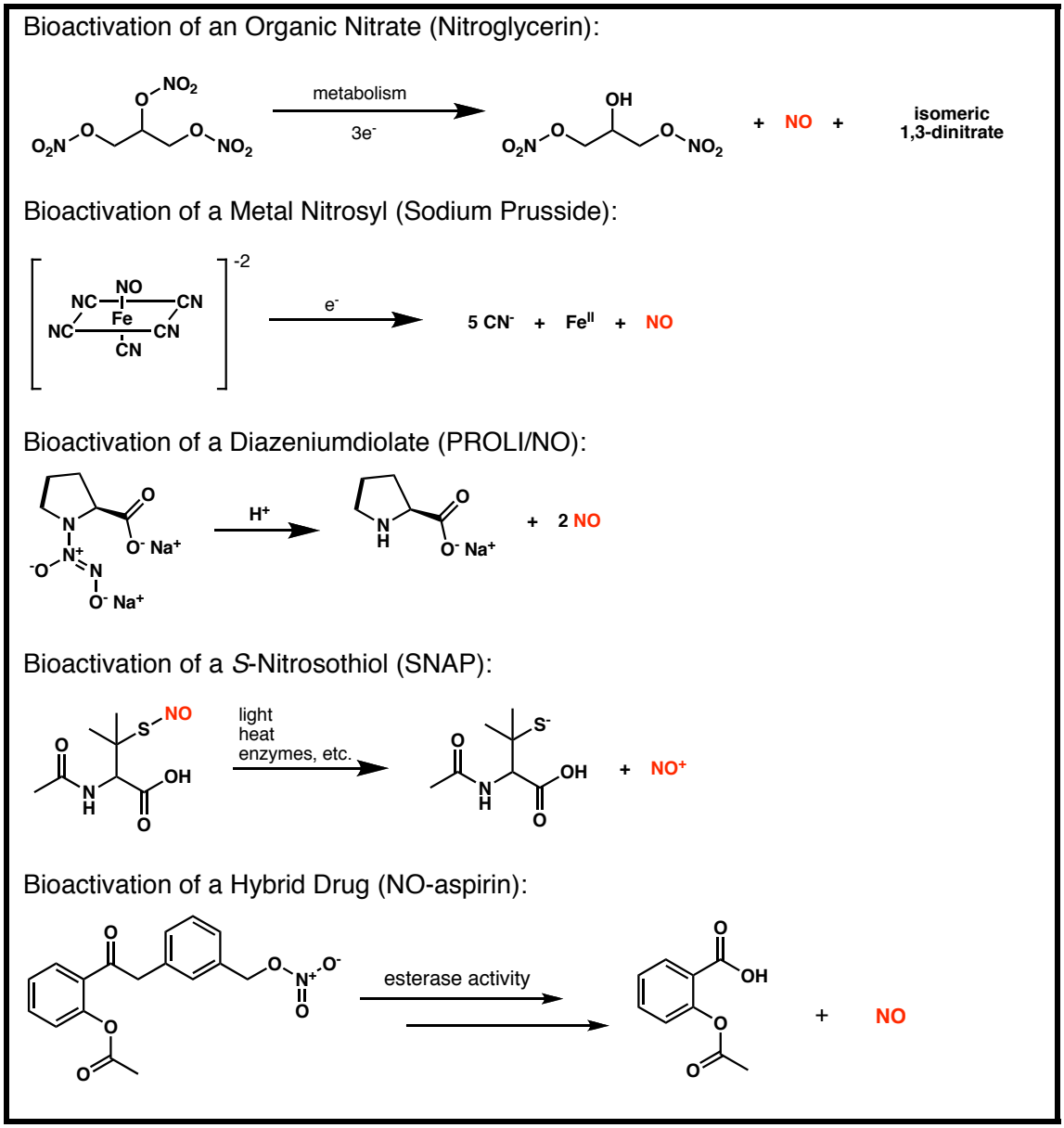

Figure 1-2. Examples of current systems that store and release NO, including nitroglycerin, sodium prusside, PROLI/NO, SNAP, and NO-aspirin.[13, 15]

A novel approach to the design of NO-releasing drugs is hybrid NO donor drugs. The aim of this strategy is to synthesize drugs that retain the pharmacological activity of the parent compound but also have the biological actions of NO as a complementary system.[13, 15] For example, a major limitation of non-steroidal anti-

inflammatory drugs (NSAIDs) such as aspirin is its toxic effects on the gastrointestinal tract. However, NO has cytoprotective properties in the stomach and other organs; thus, NO-releasing NSAIDs can be synthesized to protect the gastrointestinal system while maintaining its anti-inflammatory activity.[13, 15]

Most of the current systems utilized for the storage and release of NO are organic systems that rely on metabolizing the prodrug. A promising approach for NO therapy is to covalently immobilize metal nitrosyl (M—NO) complexes within porous polymeric hosts because varying the M—NO units can control the release of NO.[16] Padden and coworkers previously reported the synthesis of materials that can reversibly bind NO.[16a] The material slowly and passively releases NO, and initial *in vitro* studies display the promise of this material for use as a coating for implantable stents used in balloon angioplasty and other surgical instruments.

The instantaneous release of NO on demand is also desirable for various medical purposes.[3, 11] Several M—NO complexes have been studied that release NO upon photolysis.[17-18] In an attempt to make these M—NO complexes medically useful, researchers have incorporated them into different materials. Mitchell-Koch and coworkers reported the immobilization of a ruthenium-nitrosyl complex within a porous organic polymer, which demonstrated controllable release to myoglobin.[16b] Other M—NO systems have been entrapped in various polymers and have been shown to effectively release NO upon photoactivation.[19] These M—NO systems show great promise because they can locally deliver NO without fear of producing toxic by-products.

Nanomaterials: General Concepts

Another approach to improving these systems is to develop nanomaterials that interact with NO. Nanomaterials are an aspect of nanotechnology that concentrate on synthesizing and studying materials having at least one dimension less than 100 nm.[20] Even though nanomaterials have been in existence for centuries, their usefulness has only recently been exposed. They offer tremendous potential to achieve advancements in the area of electronics, biotechnology, and catalysis. Nanoparticles, a form of nanomaterials, can display beneficial and unique chemical and physical properties from their larger counterparts.

For example, gold is relatively inert in bulk form, but supported gold nanoparticles display unique activity for carbon monoxide oxidation, ethyne hydrochlorination, and oxidation of alcohols.[20b, 21] Carbon nanotubes exhibit vastly different chemical properties compared to both coal and diamonds.[20, 21] Some of these properties include remarkable strength, high elasticity, and large thermal conductivity and current density, which is why these materials have been proposed for various applications in medicine and electronics. Both zinc oxide and titanium dioxide are white when they are made of larger, micron-sized particles and transparent if they are made of nanoparticles.[21] Since they still absorb ultraviolet light, they are finding their way into modern, transparent, and highly effective sunscreens.

The various processes utilized to obtain nanoparticles follow two main strategies often referred to as “top down” and “bottom up”. Top down is

characterized as producing nanoproducts through reduction techniques, such as milling, etching, and lithography (Figure 1-3), and is common in the electronics industry. The bottom up approach is related to the "synthesis" of nanosized materials, starting from the molecular scale (Figure 1-3). The majority of methods used to synthesize nanoparticles utilize the bottom up approach, and they are mainly composed of single atoms or metal clusters. Despite the number of techniques available to synthesize nanoparticles, it is still a challenge to design and process functional nanoparticles with well defined structures.[22]

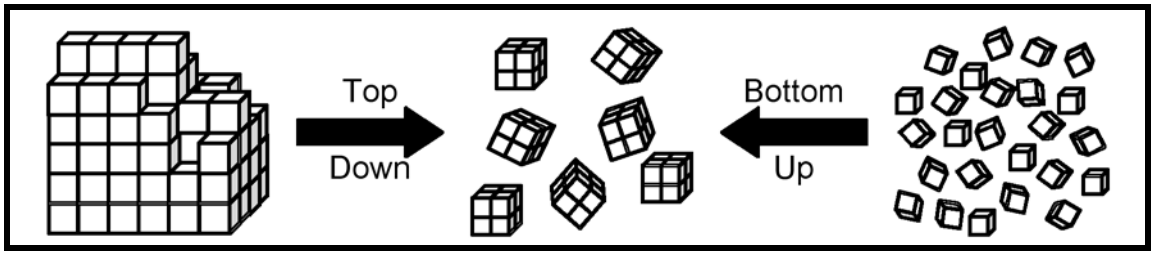

Figure 1-3. "Top down" and "bottom up" strategies.

Development of Nanomaterials that Interact with Nitric Oxide

Researchers that have synthesized NO-releasing nanomaterials all utilize the bottom up approach and covalently attach the NO-releasing unit to preformed nanoparticles. Schoenfisch and coworkers immobilized diazeniumdiolate units onto gold and silica nanoparticles.[23] The NO-releasing silica nanoparticles demonstrated enhanced bactericidal efficacy and reduced cytotoxicity of healthy cells compared to their larger counterparts.[23a] Neuman and coworkers synthesized electrostatic assemblies between water-soluble quantum dots and the cationic complex *trans*-

$[Cr(cyclam)(ONO)_2]^+$ (cyclam = 1,4,8,11-tetraazacyclotetradecane) and demonstrated enhanced NO photogeneration compared to the unassembled cationic complex.[24]

Several transition metal complexes, including *trans*-$[Cr(cyclam)(ONO)_2]^+$, are known to interact with NO, but only a few studies have been reported that characterize nanomaterials composed entirely of metal complexes.[25] Porphyrin nanotubes and nanofiber bundles have been synthesized using phase-transfer ionic self-assembly; however, the reports do not compare the properties of the nanotubes with that of the larger, micron-sized particles.[26] A vanadium phosphorous oxide catalyst synthesized using precipitation with compressed antisolvent (PCA) technology displayed improved activity in the oxidation of *n*-butane compared to the traditionally prepared catalyst.[25]

Precipitation with compressed antisolvent technology is a semicontinuous method that regularly utilizes supercritical carbon dioxide ($sc CO_2$) as the precipitant. A detailed description of PCA technology will be discussed in Chapter 2. The process is advantageous because using $sc CO_2$ as a benign medium in chemistry satisfies several green chemistry principles such as pollution prevention, lower toxicity, and use of an abundantly available resource with no increase in environmental burden.[27] The most common employment of PCA technology occurs in the pharmaceutical industry even though it has been used to make other materials.[28]

A PCA method in which $sc CO_2$ served as the precipitant was recently described for the formation of nanoparticles composed of metal complexes containing salen ligands (Figure 1-4) (salen, *N*,*N*'-salicylidiene-1,2-ethylene-diaminato(2-)).[29] A

correlation was found between particle morphology and the molecular structure of the precursor metal complexes. Nanoparticles having rodlike structures with diameters of less than 100 nm and submicron-lengths were obtained from planar [M^{II}(salen)] precursors (M^{II} = Co, Ni), while non-planar complexes produced spherical nanoparticles.

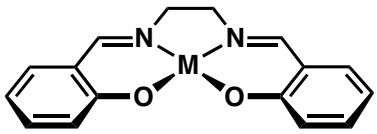

M^{II}(salen) M^{II} = Co, Ni

Figure 1-4. Metal Salen Complexes

Overview of Remaining Dissertation Chapters

Initial results from analytical and spectroscopic studies indicate that the metal complexes remain intact after being processed into particles.[29] X-ray absorption spectroscopy studies were also performed on the Co(salen) nanopaticle complexes to investigate the ligand environment around the metal center.[30] Chapter 2 will detail the results obtained from scanning electron microscopy (SEM), transmission electron microscopy (TEM), and x-ray diffraction experiments to help better understand the structure of the nanoparticulate metal complexes. It is important to gain a better understanding of the structure of the nanoparticles because the information would provide additional insight into the enhanced reactivity of the nanoparticles. The results of this study provide evidence that nanoparticles form lamellar structures during processing.

Supercritical CO_2 and PCA technology has been utilized to coat substrates with a thin layer of drugs for controlled release.[31] The same technology can be used

to coat substrates such as stents and implants with nanoparticulate metal nitrosyl complexes. It is important to understand the function of the nanoparticles compared to their molecular precursors. Chapters 3 and 4 discuss the quantitative gas uptake of NO and O_2, respectively, by both the metal salen nanoparticles and the unprocessed starting materials using a tapered element oscillating microbalance (TEOM). The Co^{II}(salen) nanoparticles display enhanced reactivity to both NO and O_2 compared to their molecular precursors. Both chapters will also discuss the experiments utilized to identify the product and understand its reactivity.

Chapter 5 describes the synthesis of a new series of alkoxysilyl-modified salen ligands, H_2**1** (Figure 1-5). The syntheses of various metal complexes with these ligands are also described. The objective of this work was to design new silica nanoparticles composed of immobilized metal complexes. Only one complex, Co^{II}**1A**, was covalently bound to silica particles because of solubility limitations with the other metal complexes. Preliminary experiments with this new material are also discussed.

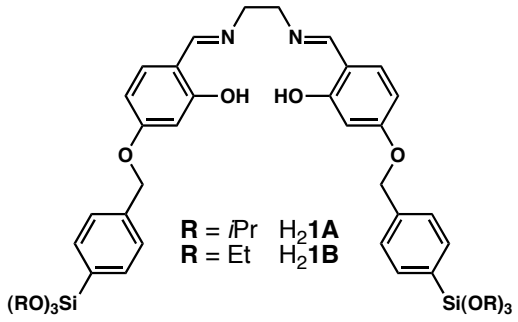

Figure 1-5. Alkoxysilyl-modified salen ligand (H_2**1**).

The studies presented in this dissertation show that fabricating nanoparticles of metal complexes utilizing PCA technology produce systems that have distinct structural and functional properties. The metal complexes that are covalently bound to silica particles also provide a good foundation for the development of new silica

nanomaterials for the storage and release of NO delivery. Ultimately, the molecular-based nanomaterials reported herein represent advances toward novel nanomaterials that interact with nitric oxide.

References

1. Greenwood, N. N.; Earnshaw, A. *Chemistry of the Elements*, 2nd ed.; Butterworth-Heinemann: Oxford, 1997.

2. (a) McCleverty, J. A. *Chem. Rev.* **2004**, *104*, 403-418. (b) Ford, P. C.; Lorkovic, I. M. *Chem. Rev.* **2002**, *102*, 993-1017.

3. *Nitric Oxide: Biology and Pathobiology*; Ignarro, L. J., Ed.; Academic Press: San Diego, 2000.

4. Stamler, J. S.; Singel, D. J.; Loscalzo, J. *Science* **1992**, *258*, 1898-1902.

5. (a) Graham, J. A.; Grant, L. D.; Folinsbee, L. J.; Kotchmar, D. J.; Garner, J. H. In *Environmental Health Criteria 188*; World Health Organization: Geneva, 1996. (b) Sloss, L. L.; Hjalmarsson, A.-K.; Soud, H. N.; Campbell, L. M.; Stone, D. K.; Shareef, G. S.; Emmel, T.; Maibodi, M.; Livengood, C. D.; Markussen, J. *Nitrogen Oxides Control Technology Fact Book*; Noyes Data Corporation: Park Ridge, 1992.

6. Armor, J. N. *Catal. Today* **1995**, *26*, 99-105.

7. Armor, J. N. *Catal. Today* **1995**, *26*, 147-158.

8. Clean Air Technology Center; Information Transfer and Program Integration Division; Office of Air Quality Planning and Standards; U. S. Environmental Protection Agency. *Zeolite, a versatile air pollutant adsorber*; The Office: Research Triangle Park, 1998.

9. Iwamoto, M.; Yokoo, S.; Sakai, K.; Kagawa, S. *J. Chem. Soc., Faraday Trans. 1* **1981**, *77*, 1629-1638.

10. For examples see: (a) Martins, L.; Peguin, R. P. S.; Wallau, M.; Urquieta-Gonzalez, E. A. *J. Braz. Chem. Soc.* **2005**, *16*, 589-596. (b) Chang, Y.-f.; McCarty, J. G. *J. Catal.* **1998**, *178*, 408-413. (c) Bell, A. T. *Catal. Today* **1997**, *38*, 151-156. (d) Minming, H.; Chunhua, Y.; Kunsong, C. *J. Mol. Catal.* **1991**, *69*, L7-L13. (e) Iwamoto, M.; Hamada, K. *Catal. Today* **1991**, *10*, 57-71. (f) Kanno, Y.; Matsui, Y.; Imai, H. *J. Inclusion Phenom.* **1987**, *5*, 385-395.

11. *Nitric Oxide: Principles and Actions*; Lancaster, J., Ed.; Academic Press: San Diego, 1996.

12. Wink, D. A.; Mitchell, J. B. *Free Radical Biol. Med.* **1998**, *25*, 434-456.

13. Miller, M. R.; Megson, I. L. *Br. J. Pharmacol.* **2007**, *151*, 305-321.

14. (a) *Nitric Oxide and Infection*; Fang, F. C., Ed.; Kluwer Academic/Plenum Publishers: New York, 1999. (b) Toda, N.; Nakanishi-Toda, M. *Prog. Retinal Eye Res.* **2007**, *26*, 205-238.

15. For examples see: (a) Low, S. Y. *Mol Aspects Med* **2005**, *26*, 97-138. (b) Napoli, C.; Ignarro, L. J. *Annu Rev Pharmacol Toxicol* **2003**, *43*, 97-123. (c) Wang, P. G.; Xian, M.; Tang, X.; Wu, X.; Wen, Z.; Cai, T.; Janczuk, A. J. *Chem Rev* **2002**, *102*, 1091-1134.

16. (a) Padden, K. M.; Krebs, J. F.; MacBeth, C. E.; Scarrow, R. C.; Borovik, A. S. *J. Am. Chem. Soc.* **2001**, *123*, 1072-1079. (b) Mitchell-Koch, J. T.; Reed, T. M.; Borovik, A. S. *Angew. Chem., Int. Ed.* **2004**, *43*, 2806-2809. (c) Mitchell-Koch, J. T.; Padden, K. M.; Borovik, A. S. *J. Polym. Sci., Part A: Polym. Chem.* **2006**, *44*, 2282-2292.

17. (a) de Leo, M.; Ford, P. C. *J. Am. Chem. Soc.* **1999**, *121*, 1980-1981. (b) Works, C. F.; Ford, P. C. *J. Am. Chem. Soc.* **2000**, *122*, 7592-7593. (c) DeRosa, F.; Bu, X.; Ford, P. C. *Inorg. Chem.* **2005**, *44*, 4157-4165.

18. (a) Patra, A. K.; Afshar, R.; Olmstead, M. M.; Mascharak, P. K. *Angew. Chem., Int. Ed.* **2002**, *41*, 2512-2515. (b) Patra, A. K.; Mascharak, P. K. *Inorg. Chem.* **2003**, *42*, 7363-7365. (c) Ghosh, K.; Eroy-Reveles, A. A.; Avila, B.; Holman, T. R.; Olmstead, M. M.; Mascharak, P. K. *Inorg. Chem.* **2004**, *43*, 2988-2997.

19. (a) Eroy-Reveles, A. A.; Leung, Y.; Beavers, C. M.; Olmstead, M. M.; Mascharak, P. K. *J. Am. Chem. Soc.* **2008**, *130*, 4447-4458. (b) Halpenny, G. M.; Olmstead, M. M.; Mascharak, P. K. *Inorg. Chem.* **2007**, *46*, 6601-6606. (c) Eroy-Reveles, A. A.; Leung, Y.; Mascharak, P. K. *J. Am. Chem. Soc.* **2006**, *128*, 7166-7167. (d) Bordini, J.; Ford, P. C.; Tfouni, E. *Chem. Commun.* **2005**, 4169-4171.

20. (a) Roco, M. C. In *Handbook of Nanoscience, Engineering, and Technology*; Goddard, W. A., Brenner, D. W., Lyshevski, S. E., Iafrate, G. J., Eds.; CRC Press: Boca Raton, 2007, pp 3.1-3.26. (b) *Nanotechnology in Catalysis*; Zhou, B.; Han, S.; Raja, R., Eds.; Springer: New York, 2007.

21. Foster, L. E. *Nanotechnology: Science, Innovation, and Opportunity*; Prentice Hall: Upper Saddle River, 2006.

22. (a) Johnston, K. P.; Shah, P. S. *Science* **2004**, *303*, 482-483. (b) McLeod, M. C.; Anand, M.; Kitchens, C. L.; Roberts, C. B. *Nano Lett.* **2005**, *5*, 461-465. (c) Ogale, S. B.; Ahmad, A.; Pasricha, R.; Dhas, V. V.; Syed, A. *Appl. Phys. Lett.* **2006**, *89*, 263105-263107. (d) Lester, E.; Blood, P.; Denyer, J.; Giddings, D.;

Azzopardi, B.; Poliakoff, M. *J. Supercrit. Fluids* **2006**, *37*, 209-214. (e) Euliss, L. E.; DuPont, J. A.; Gratton, S.; DeSimone, J. *Chem. Soc. Rev.* **2006**, *35*, 1095-1104. (f) Dahl, J. A.; Baddux, B. L. S.; Hutchison, J. E. *Chem. Rev.* **2007**, *107*, 2228-2269. (g) Lisiecki, I. *J. Phys. Chem. B* **2005**, *209*, 12231-12244.

23. (a) Hetrick, E. M.; Shin, J. H.; Stasko, N. A.; Johnson, C. B.; Wespe, D. A.; Holmuhamedov, E.; Schoenfisch, M. H. *ACS Nano* **2008**, *2*, 235-246. (b) Shin, J. H.; Schoenfisch, M. H. *Chem. Mater.* **2008**, *20*, 239-249. (c) Polizzi, M. A.; Stasko, N. A.; Schoenfisch, M. H. *Langmuir* **2007**, *23*, 4938-4943. (d) Shin, J. H.; Metzger, S. K.; Schoenfisch, M. H. *J. Am. Chem. Soc.* **2007**, *129*, 4612-4619.

24. (a) Neuman, D.; Ostrowski, A. D.; Mikhailovsky, A. A.; Absalonson, R. O.; Strouse, G. F.; Ford, P. C. *J. Am. Chem. Soc.* **2008**, *130*, 168-175. (b) Neuman, D.; Ostrowski, A. D.; Absalonson, R. O.; Strouse, G. F.; Ford, P. C. *J. Am. Chem. Soc.* **2007**, *129*, 4146-4147.

25. Hutchings, G. J.; Bartley, J. K.; Webster, J. M.; Lopez-Sanchez, J. A.; Gilbert, D. J.; Kiely, C. J.; Carley, A. F.; Howdle, S. M.; Sajip, S.; Caldarelli, S.; Rhodes, C.; Volta, J. C.; Poliakoff, M. *J. Catal.* **2001**, *197*, 232-235.

26. (a) Wang, Z.; Ho, K. J.; Medford, C. J.; Shelnutt, J. A. *Adv. Mater.* **2006**, *18*, 2557-2560. (b) Liu, B.; Qian, D.-J.; Chen, M.; Wakayama, T.; Nakamura, C.; Miyake, J. *Chem. Commun.* **2006**, 3175-3177.

27. Jessop, P. G.; Subramaniam, B. *Chem. Rev.* **2007**, *107*, 2666-2694.

28. Foster, N.; Mammucari, R.; Dehghani, F.; Barrett, A.; Bezanehtak, K.; Coen, E.; Combes, G.; Meure, L.; Ng, A.; Regtop, H. L.; Tandya, A. *Ind. Eng. Chem. Res.* **2003**, *42*, 6476-6493.

29. Johnson, C. A.; Sharma, S.; Subramaniam, B.; Borovik, A. S. *J. Am. Chem. Soc.* **2005**, *127*, 9698-9699.

30. Johnson, C.; Long, B.; Nguyen, J. G.; Day, V. W.; Borovik, A. S.; Subramaniam, B.; Guzman, J. *J. Phys. Chem. C* **2008**, *112*, 12272-12281.

31. (a) Subramaniam, B.; Saim, S.; Rajewski, R.; Stella, V. J. *ACS Symp. Ser.* **2001**, *766*, 96-110. (b) Subramaniam, B.; Saim, S.; Rajewski, R. A.; Stella, V.; (The University of Kansas, USA). Application: US, 1998, 30 pp, Cont-in-part of U S Ser No 722,463.

CHAPTER TWO

STRUCTURAL EXAMINATION OF NANOPARTICLES OF METAL COMPLEXES PROCESSED BY PCA TECHNOLOGY

Introduction

The interest in development of new nanomaterials has intensified over the last two decades because they offer tremendous potential to achieve advancements in the area of electronics, biotechnology, and catalysis. Various nanomaterials have been shown to display beneficial chemical and physical properties compared to their larger counterparts; a few of these examples were discussed in Chapter 1. However, processes for sub-micron particles of *molecules* have lagged behind atom-based systems because limited preparative methods have hindered production.[1] Precipitation with compressed antisolvent (PCA) technology is one convenient method for the preparation of nano-sized particles composed of *molecules.*

The formation of nanoparticulate metal complexes using PCA technology was recently reported;[2] however, little information about the molecular structure of the molecules within the particles (molecular structure) was known. If the molecular structure could be elucidated, it would provide valuable information concerning their chemical properties. For example, molecular structural information would help explain why gas uptake studies on these nanomaterials suggest that every metal site is accessible.

Precipitation with compressed antisolvent (PCA) technology, which is also known as supercritical antisolvent precipitation (SAS), is a semicontinuous method that regularly utilizes supercritical carbon dioxide (*sc*CO_2) as the precipitant. Supercritical fluids (SCFs) are attractive benign media for the production of nanoparticles because they display properties that are intermediate between liquid and vapor phases, increasing their usefulness.[3] Water and carbon dioxide are common SCFs because they are cheap, non-polluting, nontoxic, and easily accessible materials. Since *sc*CO_2 is readily accessed at relatively low temperatures and pressures, it is the most commonly used SCF.

In the PCA process, the molecule of interest is dissolved in a suitable organic solvent, and then the solution is sprayed simultaneously with *sc*CO_2 (Figure 2-1). Since the nonpolar *sc*CO_2 is miscible with the solvent and not the compound, it extracts the solvent from the spray, causing substantial supersaturation and particle formation.[3] The resulting particles are relatively uniform in size and are collected from both the precipitation vessel and a filter located downstream from the precipitation chamber.

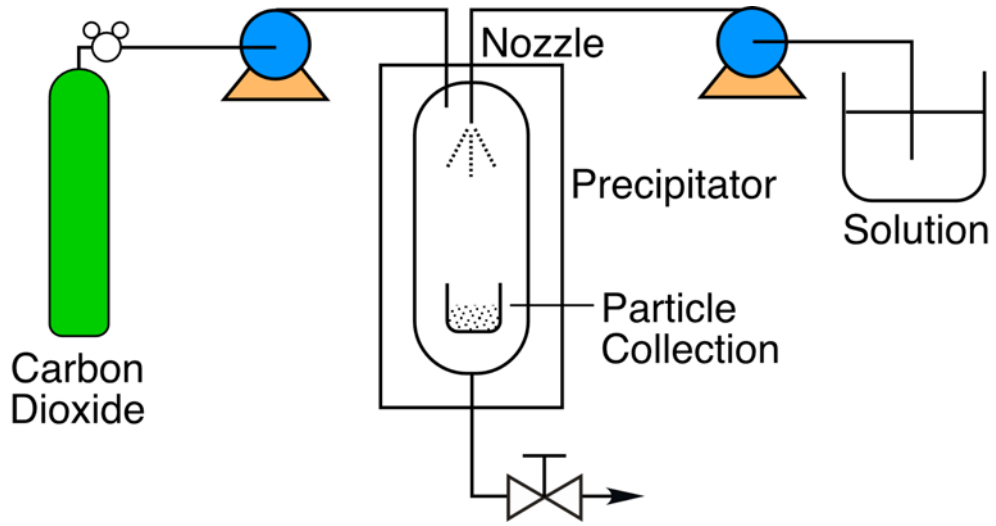

Figure 2-1. Schematic diagram of the PCA set up.

The pharmaceutical industry commonly employs PCA technology for drug formulation, but it also has been employed for other materials, such as polymers.[3] The formation of nanoparticles composed entirely of metal complexes containing salen ligands (salen, *N,N'*-salicylidiene-1,2-ethylene-diaminato(2-)) has been recently reported.[2] These metal salen (M^{II}(salen)) complexes are good candidates for this investigation because the molecular form of these complexes have been intensely studied for a variety of functions, ranging from gas binding[4] to enantioselective catalysts.[5] Figure 2-2 illustrates some of the metal complexes that were examined as particles.

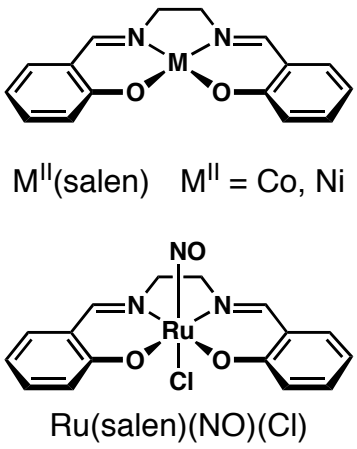

Figure 2-2. Molecular structures used in the PCA studies

Initial analytical and spectroscopic results are similar for the unprocessed M^{II}(salen) complexes and metal salen nanoparticles ($[M^{II}(salen)]_P$). Scanning electron microscopy (SEM) has also been used to examine the differences in morphology of the nanoparticles. An SEM image of $[Co^{II}(salen)]_P$ (Figure 2-3a) shows aggregates of primary particles having rodlike structures, with average diameters and lengths of 100 and 675 nm, respectively. In contrast, the SEM image of unprocessed Co^{II}(salen) shows flat hexagonal particles measuring tens to hundreds of microns (Figure 2-3b).

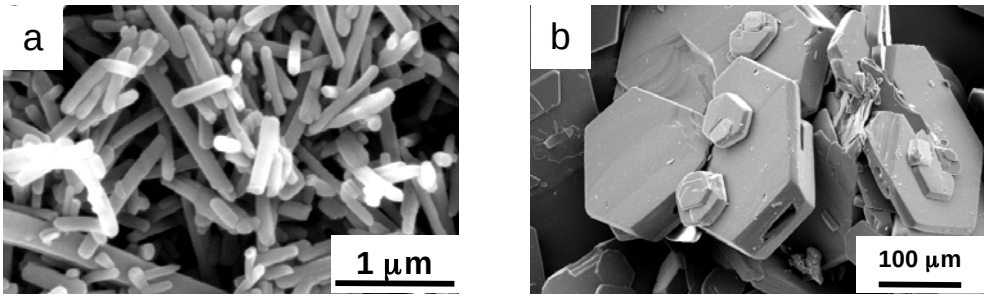

Figure 2-3. SEM images of: (a) the rodlike primary particles of $[Co^{II}(salen)]_P$ obtained from PCA technology and (b) unprocessed Co^{II}(salen).

The geometrical differences between the complexes at the molecular level influence the morphology of the processed particles. For example, planar molecules, such as Co^{II}(salen) and Ni^{II}(salen) (Figure 2-4a) form rodlike particles with nearly identical dimensions. However, nonplanar molecules have distinctly different morphologies. For instance, Ru(salen)(NO)(Cl) molecules form aggregates of primary particles with spherical structures and average diameters of approximately 50 nm (Figure 2-4b). Since changes in different PCA processing variables, such as

temperature, pressure, and CO_2 flow rate, affect the size of the nanoparticles, it is important that the particles are prepared under nearly identical operating conditions.[6]

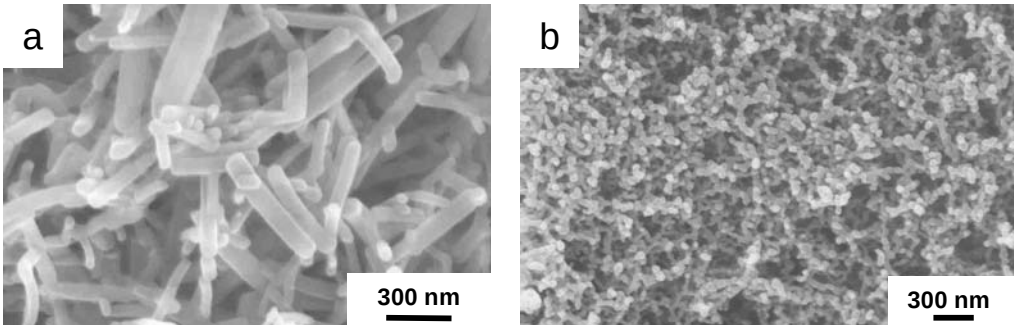

Figure 2-4. SEM images of: (a) $[Co(salen)]_P$ and (b) $[Ru(salen)(NO)(Cl)]_P$.[2]

Surface area analysis of unprocessed $Co^{II}(salen)$ and $[Co^{II}(salen)]_P$ confirms that $[Co^{II}(salen)]_P$ has a larger surface area with an average pore size a little less than 10 nm (Table 2-1).[7] Initial SEM micrographs help confirm the morphology of the nanoparticles, but additional SEM experiments are required to better understand the structure of the nanoparticles. To help complement the surface area analysis, an SEM experiment involving a sputter-coating study is necessary.

Table 3-1. Surface area analysis of unprocessed $Co^{II}(salen)$ and $[Co^{II}(salen)]_P$.[a]

	True Density (g/mL)	Surface Area (m^2/g)	Total Pore Volume (10^{-3} mL/g)	Average Pore Diameter (Å)
$Co^{II}(salen)$	1.6111	0[b]	0.4	0[b]
$[Co^{II}(salen)]_P$	1.3157	14-18	29-31	67-82

[a] Surface area analysis was collected by Dr. Chad Johnson and reported in reference 7.
[b] The measurements were below the limits of detection.

Scanning electron microscopes are useful to study the surface topography of samples; however, their resolution is one order of magnitude less than transmission electron microscopes. Transmission electron microscopy (TEM) is used to study the local structure, morphology, and chemistry of materials with nanometer resolution.

Thus, TEM was also used to help identify the structure of the nanoparticles.

A single crystal X-ray diffraction pattern of $[Co^{II}(salen)]_P$ cannot be obtained because the particles are too small, so X-ray absorption spectroscopy (XAS) has been used to probe the ligand environment around the metal center of the processed and unprocessed metal complexes. The XAS studies show that the ligand environment around the cobalt center differs between the unprocessed and processed Co(salen).[8] The XAS data suggest that unprocessed Co(salen) has a 5-coordinate cobalt center, which is confirmed with crystallographic data, but $[Co(salen)]_P$ has a 4-coordinate cobalt center with a distorted tetrahedral geometry. An electron diffraction pattern could not be obtained with TEM because the nanoparticles were too thick. Fortunately, powder X-ray diffraction (PXRD) can be used to obtain information about the structure, composition, and state of polycrystalline materials.

A crystalline material possesses a distinct X-ray pattern that can be viewed as a "finger-print"; thus, it is a common technique to quickly analyze unknown materials in fields such as mineralogy, forensic science, archeology, and biological and pharmaceutical sciences.[9] PXRD is advantageous because various samples, such as powders, solids, films, and ribbons, can be analyzed quickly and in a nondestructive manner. It is difficult to determine the crystal structures from PXRD data alone, but valuable information, such as interplanar distances and Miller indices, can be determined.

Figure 2-5 provides an illustration of how PXRD data is obtained. When a beam of monochromatic X-rays is directed at a sample, reflected and diffracted X-

rays can be observed at various angles with respect to the primary beam. Although most of the scattering X-rays are eliminated through destructive interference, diffraction occurs when scattering in a certain direction is in phase with scattered rays from other atomic planes. The Bragg equation (Equation 2-1) for the different orders of diffraction, *n*, provides the relationship between the interplanar distance, d, the wavelength of the X-ray beam, λ, and the angle of diffraction, θ.

$$n\lambda = 2d \sin \theta \qquad (2\text{-}1)$$

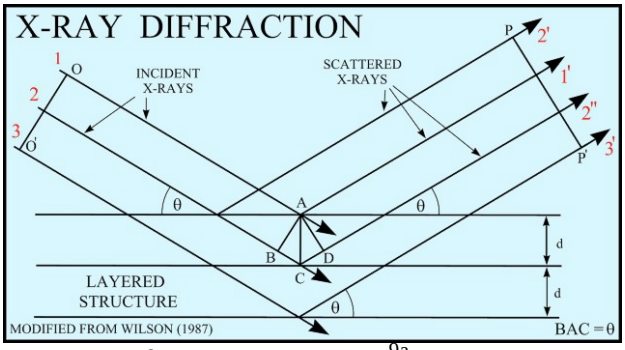

Figure 2-5. Representation of scattering X-rays.[9a]

It is important to gain a better understanding of the structure of the nanoparticles because the information would provide additional insight into the enhanced reactivity of the nanoparticles. The results reported herein describe the use of both SEM and transmission electron microscopy (TEM) to ascertain important molecular structural information of nanoparticulate Co^{II}(salen) ($[Co^{II}(salen)]_P$) and nanoparticulate Ni^{II}(salen) ($[Ni^{II}(salen)]_P$). This chapter also discusses how the PXRD data corroborates the information elucidated from microscopy.

Experimental Section

General Methods. All reagents were purchased from commercial sources and used as received, unless otherwise noted. Ni^{II}(salen) was synthesized following literature methods.[2]

Physical Methods. ^{1}H and ^{13}C NMR spectra were recorded on Bruker Avance 400 or 500 MHz spectrometers equipped with a Silicon Graphics workstation. Chemical shifts are reported in ppm relative to residual solvent. Perpendicular-mode X-band EPR spectra were collected using a Bruker EMX spectrometer equipped with an ER041XG microwave bridge. A quartz liquid nitrogen finger Dewar (Wilmad Glass) was used to record spectra at 77 K, and low-temperature (4 K) spectra were obtained using an Oxford Instrument liquid He quartz cryostat. Spectra for EPR active samples were collected using the following spectrometer settings: attenuation = 15 dB, microwave power = 6.300 mW, frequency = 9.26 GHz, sweep width = 5000 G, modulation amplitude = 10.02 G, gain = 1.00 x 10^3, conversion time = 81.920 ms, time constant = 655.36 ms, and resolution = 1024 points.

Scanning electron micrographs were acquired on a Schottky thermal field emission FEI/Philips XL-30FEG operating at an accelerating voltage of 10.0 kV. SEM samples were prepared by sprinkling the particles directly onto a conductive carbon tab (Ted Pella, Inc. Part # 16084-1) attached to a 12.7 mm diameter aluminum specimen mount (Ted Pella, Inc. Part # 16111) and pressed down. The sample was sputter-coated with 2 different sources and instruments. Some of the samples were sputter-coated with an iridium coat by using a South Bay Technology, Incorporated IBS/e- System for variable amounts of time operating at approximately 5 mTorr and 6 mA. The rest of the samples were sputter-coated with a 3 nm thick Au-Pd alloy coat

by using a Polaron SC7600 operating at 53 mTorr and 5 mA.

Transmission electron micrographs were acquired using a FEI/Philips CM-20 operating at 200 kV. The samples were prepared by two different methods. For the first method, $[M^{II}(salen)]_P$ were dispersed in distilled water and sonicated for various times from 5 minutes to 20 minutes. A drop was then deposited on an ultrathin holey carbon film on a 400 mesh copper grid (Ted Pella, Inc. Part # 01824) and allowed to dry prior to imaging. The second method involved pressing a small amount of the nanoparticles onto the copper grid.

Powder X-ray diffraction experiments were performed using a Rigaku D/Max 2200PC Ultima III multipurpose powder diffractometer with graphite-monochromated Cu Kα radiation. X-rays were provided by a normal-focus sealed X-ray tube operated at 40 kV and 44 mA. Scans were taken with an increment size of 0.05° over a range of 2θ from 5° to 70°. The diffractograms were processed using Jade 8.0 software.

Results and Discussion

SEM Studies of $[Co^{II}(salen)]_P$. Micrographs of uncoated $[Co^{II}(salen)]_P$ show the possibility of either a hollow or lamellar (layered) structure (Figure 2-6). The images show a lighter circular region at the end of the nanoparticles. This contrast provides possible evidence of a denser outer shell with either an empty core (i.e. hollow nanoparticles) or a different structure within the inner core (i.e. lamellar structure). Unfortunately, the particles are nonconducting (or insulating) specimens, and an accumulation of electrons on the samples creates high surface potentials that degrade SEM images.[10] This degradation, usually known as charging issues, makes it difficult to confirm the nanoparticulate structure because these images can contain artificial signals, such as brighter contrasts in different areas of the specimen.

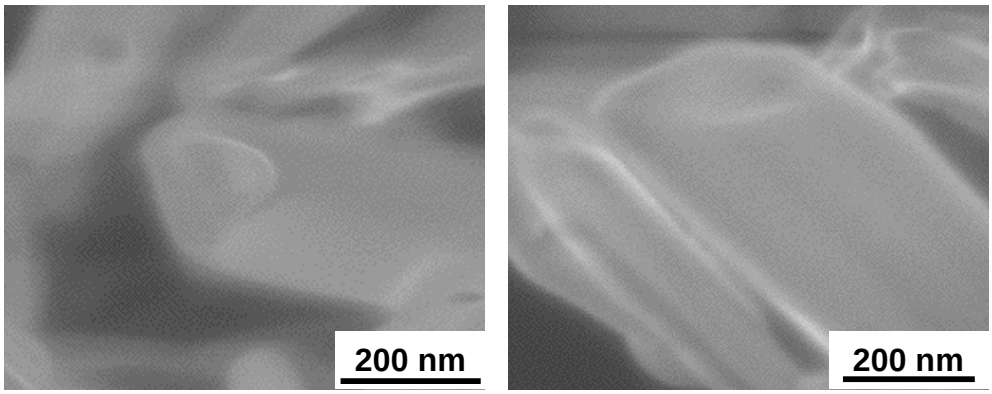

Figure 2-6. SEM micrographs of uncoated $[Co^{II}(salen)]_P$ indicating a possibility of either a hollow or two-core structure.

In order to avoid charging issues, the nanoparticles need to be sputter-coated. When a specimen is sputter-coated, it is coated with a thin layer of a conductive metal, which decreases the accumulation of electrons on the sample. When the nanoparticles are sputter-coated, there are two concerns that need to be addressed. The first concern is that the particles need to have a minimal layer that eliminates any charging effects. The second concern is to avoid filling the possible hollow ends. To help prevent filling the possible hollow ends, the samples coated with iridium were spun while they were sputter-coated.

The nanoparticles were coated with iridium for 30 seconds (Figure 2-7a) and 60 seconds (Figure 2-7b), which provided approximately 0.9 and 1.7 nm thick coatings, respectively. The nanoparticles were also coated with a Au-Pd alloy for 90 seconds, which provided approximately a 3 nm thick coating (Figures 2-7c and 2-7d). These SEM images show a few particles that have openings at their edges. Unfortunately, these images do not provide sufficient evidence to determine if the nanoparticles are hollow; thus, more information is needed to support this idea.

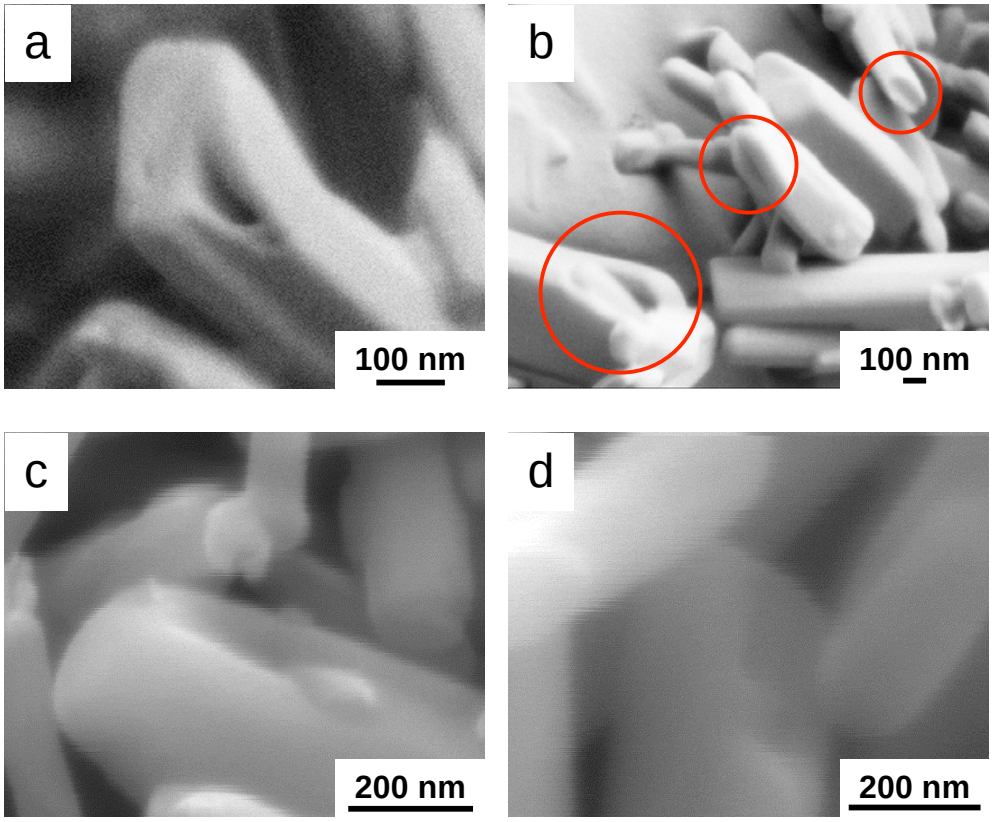

Figure 2-7. SEM micrographs of $[Co^{II}(salen)]_P$ coated with: (a) iridium for 30 s; (b) iridium for 60 s (circles show a few particles that might be hollow); (c) Au-Pd for 90 s (3 nm); and (d) Au-Pd for 90 s (3 nm).

Figure 2-7 shows images of nanoparticles that might be hollow, but the idea of a layered structure cannot be dismissed because the nanoparticles could have inner cores or layers that are shorter in length than the outer core. Instead of looking at the ends of the particles for hollow cores, it may be possible to look for particles that are "cracked," which exposes the internal layers. Figure 2-8 shows SEM micrographs representing the possibility of the lamellar structure of $[Co^{II}(salen)]_P$. The layers appear like "steps" in the middle of the particle, which are approximately 25 nm thick. These images provide evidence that the nanoparticulate metal complexes form a lamellar structure during processing, which is somewhat contradictory to information ascertained from the SEM images in Figure 2-7.

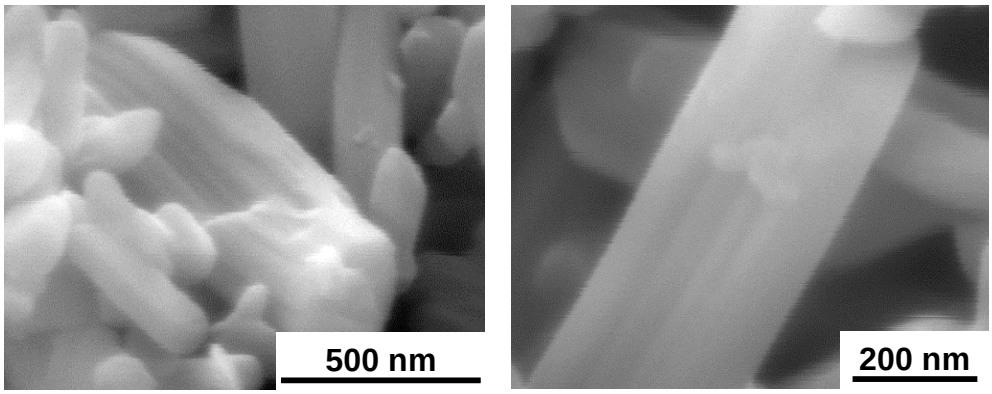

Figure 2-8. SEM micrographs showing a possible lamellar structure of $[Co^{II}(salen)]_P$.

TEM Studies of $[Co^{II}(salen)]_P$ and $[Ni^{II}(salen)]_P$. Transmission electron microscopy (TEM) has been utilized to help determine whether $[M^{II}(salen)]_P$ has a lamellar structure. Representative TEM micrographs of $[Co^{II}(salen)]_P$ (Figure 2-9a) and $[Ni^{II}(salen)]_P$ (Figure 2-9b) show that two main cores exist within the nanoparticles. The inner core has a well-defined boundary and is darker than the outer core. Hollow particles normally display a well-defined boundary with a lighter inner core.[11] The darker region is due to increased electron scattering, which supports the notion that there are more molecules in the inner core. Even though the TEM sample mostly diffracts rather than absorbs the electron beam, the intensity of the transmitted beam is still affected by the volume and density of the material through which it passes. Because these nanoparticles are rather thick for TEM analysis, these images do not provide any information on molecular structure of the nanoparticles. In order to ascertain any structural information from TEM, the nanoparticulate samples need to be prepared in a manner that would produce thinner specimens.

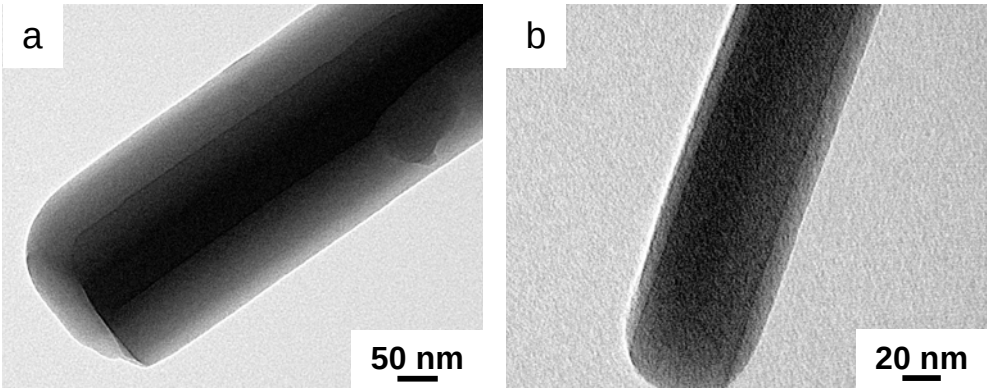

Figure 2-9. TEM micrographs of: (a) $[Co^{II}(salen)]_P$ and (b) $[Ni^{II}(salen)]_P$.

The lamellar structure of these nanoparticles is more apparent when the nanoparticles are sonicated as shown in Figure 2-10. When the nanoparticles are sonicated in water, their structure begins to break apart. The boundaries of four layers can easily be observed when the samples are sonicated (Figure 2-10a), where each layer adds approximately 20 nm to the diameter of the nanoparticles. An image of a broken $[Co^{II}(salen)]_P$ exposes the layers of the nanoparticle (Figure 2-10b). Overall, both SEM and TEM micrographs support the premise of a lamellar structure within $[M^{II}(salen)]_P$.

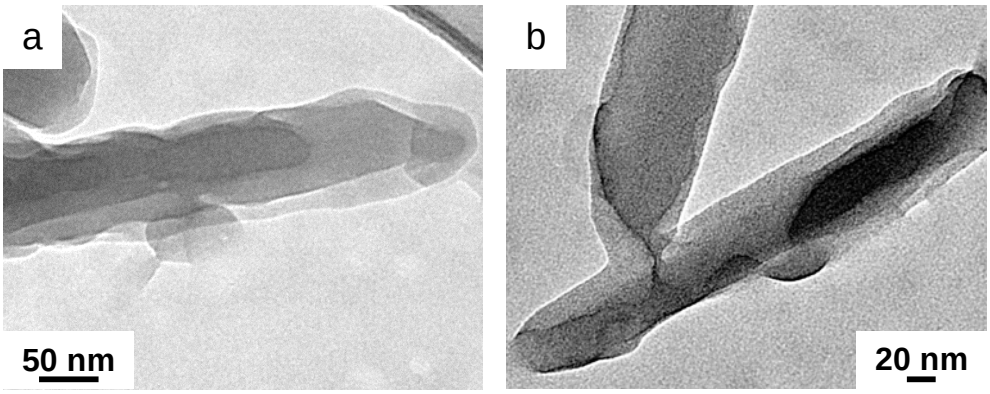

Figure 2-10. TEM micrographs of $[Co^{II}(salen)]_P$ prepared after the particles were sonicated in water where (a) shows well-defined boundaries of four different layers and (b) shows exposed layers in nanoparticle.

Powder XRD Studies of $[Co^{II}(salen)]_P$ and $[Ni^{II}(salen)]_P$. To further determine the structure of the metal complex nanoparticles, powder X-ray diffraction (PXRD) was carried out on both unprocessed and processed metal complexes. These studies indicate that unprocessed $Co^{II}(salen)$ and $[Co^{II}(salen)]_P$ contain species with different solid-state structures (Figure 2-11). The broader peaks in the diffractograph of $[Co^{II}(salen)]_P$ (Figure 2-11a) indicate smaller crystalline dimensions relative to unprocessed $Co^{II}(salen)$ (Figure 2-11b). When the crystalline dimensions are less than 0.1 μm, the sharpness of the back-reflection lines are affected, resulting in broader peaks.[12]

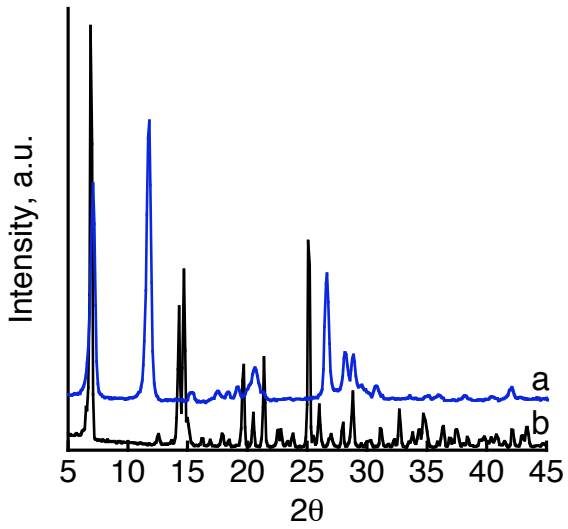

Figure 2-11. PXRD data of (a) $[Co^{II}(salen)]_P$ and (b) unprocessed $Co^{II}(salen)$.

Analysis of the PXRD data for unprocessed $Co^{II}(salen)$ is simpler since the molecular structure has been solved and reported.[8] Unprocessed $Co^{II}(salen)$ has a monoclinic unit cell with dimensions of a = 26.339(3) Å, b = 6.9804(8) Å, c = 14.203(2) Å (Figure 2-12), and some of the diffraction peaks are associated with these dimensions. The main diffraction peak for unprocessed $Co^{II}(salen)$ at 6.896° has an interplanar distance of 25.62 Å (n = 2), which is similar to a. The second

largest diffraction peak at 25.121° is associated with both b and c. This diffraction peak has an interplanar distance of 7.09 Å (n = 2) for b and 14.17 Å (n = 4) for c. The peaks centered around 14.5° could be associated with all three lattice planes because the interplanar distances are fairly similar to the unit cell dimensions.

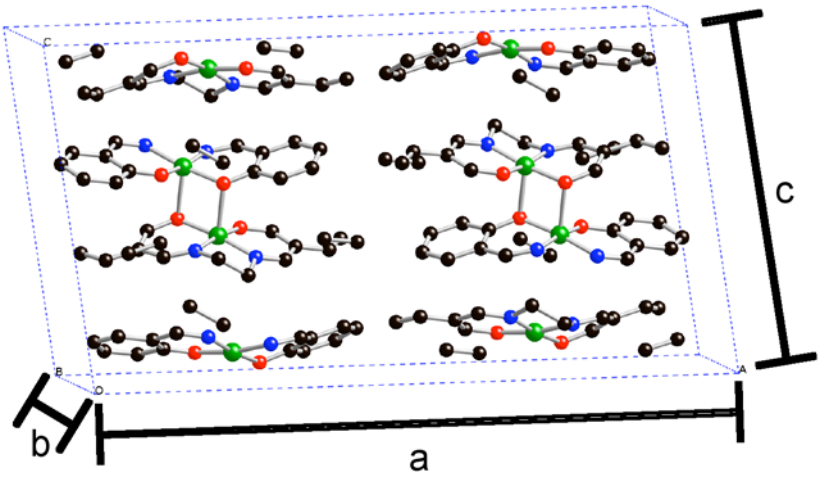

Figure 2-12. The unit cell of unprocessed Co^{II}(salen) with the hydrogen atoms omitted for clarity. The crystallographic data is available in Reference 8.

One noticeable difference in the diffractogram of $[Co^{II}(salen)]_P$ is a new main diffraction peak at 11.751°, which represents the appearance of an interplanar distance of 7.525 Å. The second and third order Bragg diffraction peaks related to this lattice plane is found at 26.589° and 41.939°, respectively. The diffraction peak at 7.050° is similar to the main diffraction peak for unprocessed Co^{II}(salen). However, the PXRD data indicates that the crystal structures for the unprocessed and processed materials differ greatly, which supports the results obtained from XAS. Therefore, it is not appropriate to make any comparisons between unprocessed and nanoparticle Co^{II}(salen).

Since the PXRD data for unprocessed and processed Ni^{II}(salen) are similar

(Figure 2-13), the molecular structure of Ni^{II}(salen) will provide some valuable insight on the arrangement of the molecules within $[Ni^{II}(salen)]_P$. Unprocessed Ni^{II}(salen) also has a monoclinic unit cell with dimensions of a = 13.831(3) Å, b = 26.155(5) Å, and c = 7.482(2) Å (Figure 2-14).[13] The main diffraction peak at 6.896° for unprocessed Ni^{II}(salen) is associated with both a and b. This diffraction peak has an interplanar distance of 12.81 Å (n = 1) for a and 25.62 Å (n = 2) for b. The second major peak at 11.594° has a lattice plane that is 7.63 Å (n = 1), which is similar to c. Additionally, the diffraction peak at 14.748° is also associated with b (24.01 Å, n = 4), and the peak at 12.971° is associated a (13.64 Å, n = 2).

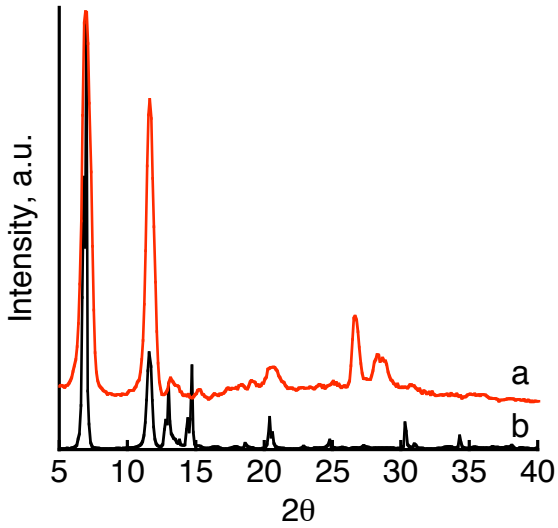

Figure 2-13. PXRD data of (a) $[Ni^{II}(salen)]_P$ and (b) unprocessed Ni^{II}(salen).

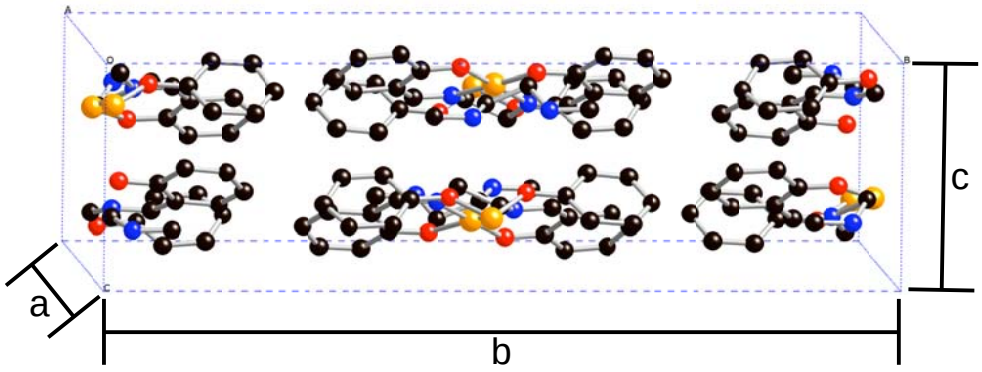

Figure 2-14. The unit cell of unprocessed Ni^{II}(salen) with the hydrogen atoms omitted for clarity. The crystallographic data is available in Reference 3.

Overall, the similar PXRD patterns between unprocessed and nanoparticulate $[Ni^{II}(salen)]_P$ provide evidence that the crystal structures are similar, where the unit cell shape and size is practically the same. Like $[Co^{II}(salen)]_P$, the peaks for $[Ni^{II}(salen)]_P$ are also broader relative to unprocessed Ni^{II}(salen), which is due to the smaller crystalline dimensions. One of the most important differences involves the appearance of the peaks at 26.641° and 28.5° and the disappearance of the peak at 14.748° in $[Ni^{II}(salen)]_P$. This difference is most likely due to disorder within $[Ni^{II}(salen)]_P$. The appearance of extra diffraction peaks commonly occurs when the symmetry of the crystallites decreases and/or the disorder within the crystallites increases.[14]

Another difference between unprocessed and nanoparticulate Ni^{II}(salen) involves the intensity of the peak at 11.6°, where the intensity for $[Ni^{II}(salen)]_P$ is more intense relative to its unprocessed analog. Relative intensity increases are generally due to preferential orientation of the crystallites, which is common in highly asymmetric crystallites.[12] Random orientation of the crystallites is normally desired, but this preferential orientation can provide insight into the molecular structure of

$[Ni^{II}(salen)]_P$ because it identifies a prominent interplanar distance. The diffraction peak at 11.610° has an interplanar distance of 7.616 Å, which is similar to c. Since the lattice planes along the c-axis are prevalent within $[Ni^{II}(salen)]_P$, it could be associated with the lamellar structure within the nanoparticle.

While the PXRD patterns for unprocessed and nanoparticulate $Ni^{II}(salen)$ are similar, the PXRD patterns for $[Co^{II}(salen)]_P$ and $[Ni^{II}(salen)]_P$ are virtually identical (Figure 2-15). The lower intensities and slight peak shifts found for $[Co^{II}(salen)]_P$, are due to the different metal atoms.[12] Another minor difference is that the relative intensity for the diffraction peak at approximately 11.6° is larger for $[Co^{II}(salen)]_P$, which is most likely due to the preferred orientation within the nanoparticles. Beyond these minor differences, results from microscopy and PXRD suggest that $[Ni^{II}(salen)]_P$ and $[Co^{II}(salen)]_P$ are isostructural and similar to the molecular structure present in unprocessed $Ni^{II}(salen)$.

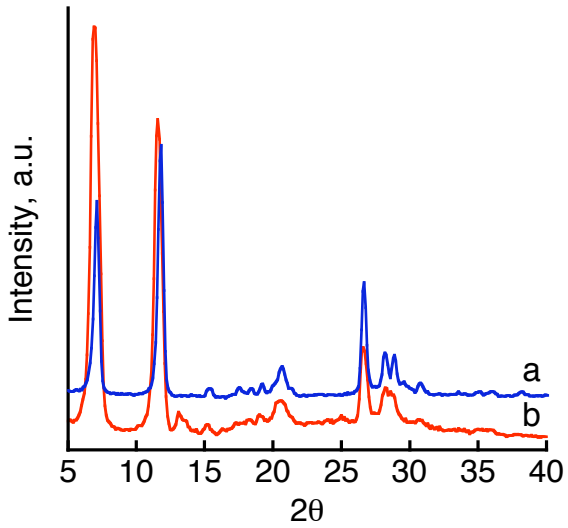

Figure 2-15. PXRD data of (a) $[Co^{II}(salen)]_P$ and (b) $[Ni^{II}(salen)]_P$.

Results obtained from microscopy and PXRD also suggest that the molecular structure is layered within the nanoparticulate metal complexes. The peak at 11.6° is

an important interplanar distance for both $[Ni^{II}(salen)]_P$ and $[Co^{II}(salen)]_P$. This peak is important to $[Co^{II}(salen)]_P$ because it is a new diffraction peak. Since $[Co^{II}(salen)]_P$ and $[Ni^{II}(salen)]_P$ are isostructural, the lattice planes along the c-axis are prevalent in both sets of nanoparticles. As such, it is reasonable to conclude that the molecular structure is layered within the nanoparticulate metal complexes, and these layers are associated with the lattice plane along the c-axis because the distance of the lattice planes are similar.

Summary and Conclusions

Microscopy results indicate that the rodlike nanoparticulate metal complexes form lamellar structures during processing. The SEM micrographs of broken nanoparticles show the inner core layers, and they provide the strongest topological evidence for the existence of a nanoparticulate lamellar structure. TEM studies also show that the metal complex nanoparticles are made of different layers. The TEM images of the nanoparticles show two well-defined cores that contain various layers that are not as well defined. When the nanoparticles are sonicated slightly, the different layers are more prominent in the TEM micrographs.

Powder X-ray diffraction data also support the idea that the nanoparticulate metal complexes have lamellar structures. The PXRD results for $[Co^{II}(salen)]_P$ indicate that these structures are vastly different than the unprocessed $Co^{II}(salen)$ particles, which is already confirmed by XAS studies.[8] The PXRD data for unprocessed and nanoparticulate $Ni^{II}(salen)$ is similar, which means that their molecular structures are also similar. Since the PXRD data for $[Co^{II}(salen)]_P$ and $[Ni^{II}(salen)]_P$ are virtually identical, $[Co^{II}(salen)]_P$ also has a similar molecular structure to that of unprocessed $Ni^{II}(salen)$. The diffraction peaks at approximately 11.6° are prominent in both nanoparticulate metal complexes and most likely

associated with the layers within the nanoparticles.

The nanoparticulate metal complexes also have larger surface areas compared to their unprocessed analogs,[7] which can be explained by the lamellar structure possessed by these nanoparticles. Since surface area analyses are average measurements of the bulk properties, the combined layers can contribute to the average pore size found in the nanoparticles. Altogether, the results provide insight into the structural composition of the metal complex nanoparticles.

References

1. Hutchings, G. J.; Bartley, J. K.; Webster, J. M.; Lopez-Sanchez, J. A.; Gilbert, D. J.; Kiely, C. J.; Carley, A. F.; Howdle, S. M.; Sajip, S.; Caldarelli, S.; Rhodes, C.; Volta, J. C.; Poliakoff, M. *J. Catal.* **2001**, *197*, 232-235.

2. Johnson, C. A.; Sharma, S.; Subramaniam, B.; Borovik, A. S. *J. Am. Chem. Soc.* **2005**, *127*, 9698-9699.

3. (a) Dahl, J. A.; Baddux, B. L. S.; Hutchison, J. E. *Chem. Rev.* **2007**, *107*, 2228-2269. (b) Jessop, P. G.; Subramaniam, B. *Chem. Rev.* **2007**, *107*, 2666-2694. (c) Reverchon, E.; Adami, R. *J. Supercrit. Fluids* **2006**, *37*, 1-22. (d) Foster, N.; Mammucari, R.; Dehghani, F.; Barrett, A.; Bezanehtak, K.; Coen, E.; Combes, G.; Meure, L.; Ng, A.; Regtop, H. L.; Tandya, A. *Ind. Eng. Chem. Res.* **2003**, *42*, 6476-6493.

4. (a) Jones, R. D.; Summerville, D. A.; Basolo, F. *Chem. Rev.* **1979**, *79*, 139-179. (b) Niederhoffer, E. C.; Timmons, J. H.; Martell, A. E. *Chem. Rev.* **1984**, *84*, 137-203.

5. Jacobsen, E. N. *Acc. Chem. Res.* **2000**, *33*, 421-431.

6. (a) Kröber, H.; Teipel, U. *J. Supercrit. Fluids* **2002**, *22*, 229-235. (b) Reverchon, E. *J. Supercrit. Fluids* **1999**, *15*, 1-21. (c) Park, Y.; Curtis, C. W.; Roberts, C. B. *Ind. Eng. Chem. Res.* **2002**, *41*, 1504-1510.

7. Johnson, C. A.; Ottiger, S.; Pini, R.; Gorman, E.; Nguyen, J. G.; Munson, E.; Mazzotti, M.; Borovik, A. S.; Subramaniam, B. *AIChE J.* accepted pending minor revisions.

8. Johnson, C.; Long, B.; Nguyen, J. G.; Day, V. W.; Borovik, A. S.; Subramaniam, B.; Guzman, J. *J. Phys. Chem. C* **2008**, *112*, 12272-12281.

9. (a) Poppe, L. J.; Paskevich, V. F.; Hathaway, J. C.; Blackwood, D. S.; U. S. Geological Survey and U. S. Department of the Interior: Woods Hole, 2001. (b) *A Guide to Materials Characterization and Chemical Analysis*, 2nd ed.; Sibilia, J. P., Ed.; VCH Publishers: New York, 1996.

10. Goldstein, J. I.; Newbury, D.; Joy, D. C.; Lyman, C. E.; Echline, P.; Sawyer, L.; Michael, J. R., *Scanning Electron Microscopy and X-Ray Microanalysis*. 3rd ed.; Kluwer Academic/Plenum Publishers: New York, 2003.

11. Wang, Z. L.; Hui, C., Eds. *Electron Microscopy of Nanotubes*; Kluwer Academic Publishers: Boston, 2003.

12. Klug, H. P.; Alexander, L. E. *X-ray Diffraction Procedures for Polycrystalline and Amorphous Materials*, 2nd ed.; John Wiley & Sons: New York, 1974.

13. Manfredotti, A. G.; Guastini, C. *Acta Cryst. C* **1983**, *39*, 863-865.

14. Takase, Aya. Rigaku, Carlsbad, CA. Personal communication, 2008.

CHAPTER THREE

NITRIC OXIDE DISPROPORTIONATION AT MILD TEMPERATURES BY A NANOPARTICULATE COBALT(II) COMPLEX

Introduction

The interest in the chemistry of nitric oxide (NO) has intensified dramatically in recent years, resulting in over 13,000 papers in the last five years.[1] The majority of these papers focus on the biological significance of NO because of its proposed role in numerous physiological and pathophysiological functions, which were detailed in Chapter 1.[2] As one of the most versatile biological molecules, problems within NO pathways can lead to various diseases and disorders.[2] Thus, it is clear that basic research geared towards understanding the fundamental mechanism of action for this molecule is of great importance.

Equally important is the need to develop materials that release NO. Since NO has been linked to regulatory processes involving the cardiovascular, regulatory, and nervous systems,[3] various NO-releasing drugs (discussed in Chapter 1) have been developed for therapeutic uses. As an inhibitor of platelet adhesion and aggregation, NO-releasing materials have been developed as coatings for improving the biocompatibility of various blood-contacting biomedical devices.[4] Many researchers have tried to utilize the cytotoxic properties of NO as an anticancer agent,[5] but the controlled release of NO to specific locales is important for this application. One

approach for the controlled release of NO is to utilize covalently immobilized photoactive metal nitrosyl (M—NO) complexes within polymeric hosts.[6] These photoactive M—NO complexes can also be entrapped in various polymers.[7]

Useful applications also exist for materials that store and subsequently release NO, but there are few examples of systems that have the capability to reversibly bind NO.[8-9] There is also a need to develop materials that readily scavenge NO because it is implicated in some diseases when present in excess concentrations.[10] Padden and coworkers have immobilized a Co^{II}(salen) complex within a porous organic host and showed that it can selectively and reversibly bind NO (Scheme 3-1).

Scheme 3-1

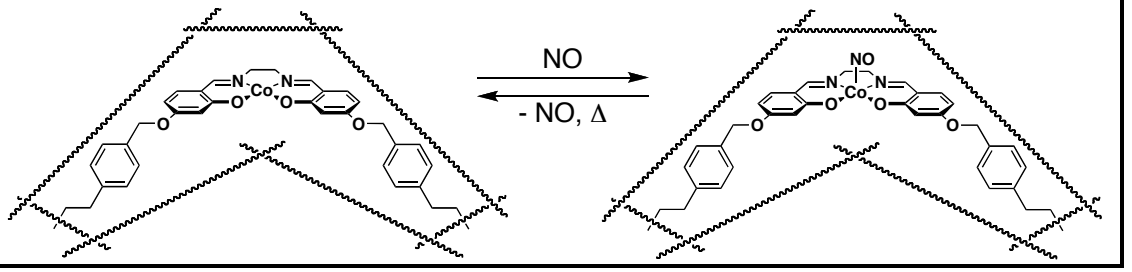

The polymeric system developed by Padden and coworkers is unique because its NO binding properties contrast those found for their molecular analogs. Co^{II}(salen) is known to irreversibly bind NO, forming the Co^{III}(salen)NO_2 species in the presence of dioxygen (Scheme 3-2).[11] In contrast, there is little evidence that amorphous or crystalline Co^{II}(salen) binds NO.[12] However, the formation of Co^{II}(salen) nanoparticles ($[Co^{II}(salen)]_P$) by precipitation with compressed anti-solvent (PCA) technology[13] could provide a new platform for NO chemistry because

other nanoparticles have displayed beneficial and unique chemical properties compared to their bulk counterparts.[14]

Scheme 3-2

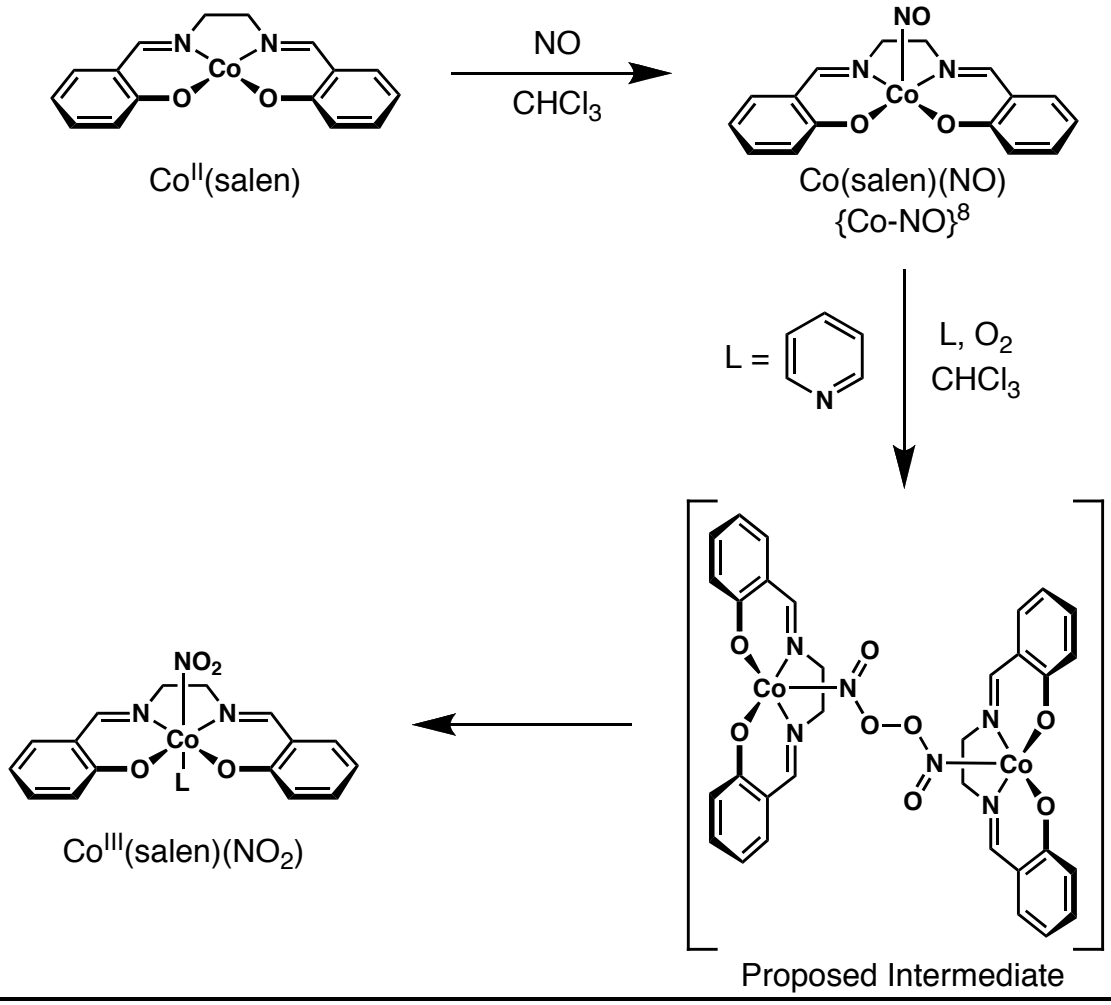

When the production of nanoparticles composed entirely of metal complexes by PCA technology was reported, their chemical reactivity had not been explored.[13] Thus, their reactivity toward gases, such as NO and O_2, was explored utilizing a tapered element oscillating microbalance (TEOM). The TEOM is an instrument that is traditionally used to accurately measure adsorption in microporous materials and can detect mass changes of a solid sample at the microgram level.[15] The instrument

measures mass change by directly measuring the change in frequency (Equation 3-1), where *k* is the force constant of the tapered element.

$$\Delta m = k\left(\frac{1}{f_1^2} - \frac{1}{f_0^2}\right) \qquad (3\text{-}1)$$

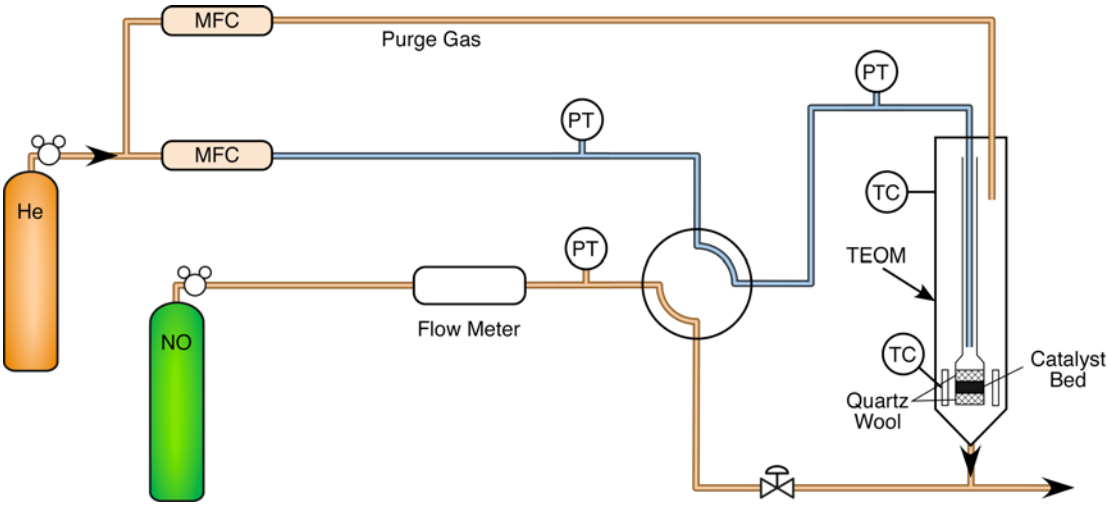

Figure 3-1. Schematic of the TEOM apparatus. MFC = Mass Flow Controller, PT = Pressure Transducer, TC = Thermal Couple.

The schematic of the TEOM used for these experiments is shown in Figure 3-1. In a typical experiment, a baseline is established by flowing pure helium through the tapered element. The sample is then exposed to pure NO, and the mass change is recorded as a function of time. It should be noted that an immediate increase in mass change is observed due to the density difference between NO and He. When the mass change stabilizes, the flow gas is switched back to He, which is also accompanied by a negative step change. The net mass gain is determined from a stable mass reading, and a typical uptake profile is shown in Figure 3-2.

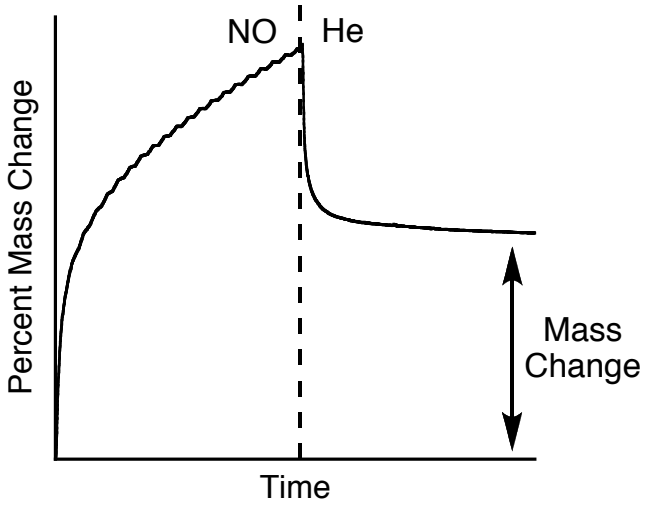

Figure 3-2. Typical TEOM uptake profile.

The original objective of this study was to determine the kinetics of NO binding to $[Co^{II}(salen)]_P$; however, our findings suggest that $[Co^{II}(salen)]_P$ catalyzes the disproportion of NO to N_2 and N_2O. Thus, this chapter describes the studies that probed the interaction of NO with unprocessed and processed M^{II}(salen) complexes, as well as the experiments utilized to determine the products of the reaction. A brief discussion on the morphological and structural effects of NO reactivity is also included.

Experimental Section

General Methods. Unprocessed Co(salen) and $NaNO_2$ were purchased from Sigma-Aldrich, and $Na^{15}NO_2$ (99%) was obtained from Promy Chemical LLC—all chemicals were used as received. Literature methods were used to synthesize Ni(salen) and the nanoparticles.[13] Nitric oxide used for the tapered element oscillating microbalance (TEOM) experiments was chemical grade (99.5%) from Linde Gas LLC. To trap out NO_X and H_2O impurities, the gas was passed through

two U-tubes immersed in isopropanol/dry ice before being exposed to the samples. Nitric oxide was generated following literature methods using $NaNO_2$ ($Na^{15}NO_2$ for ^{15}NO) and acidic $FeSO_4$.[16] Ultra-high purity helium and argon (99.996%) were purchased from Airgas and Linweld, respectively. Elemental analyses were accomplished at Desert Analytics (Tucson, AZ).

Physical Methods. Fourier transform infrared (FTIR) spectra were collected on a Mattson Genesis series or a Varian Scimitar 800 series FTIR instrument with values reported in wavenumbers. The samples were prepared as KBr pellets.

Scanning electron micrographs were acquired on a Schottky thermal field emission FEI/Philips XL-30FEG operating at an accelerating voltage of 10.0 kV. Scanning electron microscopy samples were prepared by sprinkling the sub-micron particles directly onto a conductive carbon tab (Ted Pella, Inc. Part # 16084-1) attached to a 12.7 mm diameter aluminum specimen mount (Ted Pella, Inc. Part # 16111) and pressed down. The sample was then sputter-coated with a 3 nm thick Au-Pd alloy coat by using a Polaron SC7600 operating at 53 mTorr and 5 mA.

Transmission electron micrographs were acquired using a FEI/Philips CM-20 operating at 200 kV. The samples were prepared by pressing a small amount of the nanoparticles onto an ultrathin holey carbon film on a 400 mesh copper grid (Ted Pella, Inc. Part # 01824). The transmission electron microscope was also equipped with an energy-dispersive spectrometer (EDAX/4pi) system.

Powder X-ray diffraction (PXRD) experiments were performed using a Rigaku D/Max 2200PC Ultima III multipurpose powder diffractometer with graphite-

monochromated Cu Kα radiation. X-rays were provided by a normal-focus sealed X-ray tube operated at 40 kV and 44 mA. Scans were taken with an increment size of 0.05° over a range of 2θ from 5° to 70°.

Tapered Element Oscillating Microbalance (TEOM). A Rupprecht & Patashnick TEOM 1500 mass analyzer (100 μL sample volume) was used to obtain continuous adsorption data at room temperature. Figure 3-1 contains a schematic of the experimental setup—a detailed analysis of the TEOM operating principles has been reported;[17] only a brief description of the procedure is described here. Initially, a baseline is determined by flowing helium (15 sccm) through a mass flow controller and then a 4-port valve into the TEOM with the sample in place until a stable output is achieved under ambient conditions. The flow gas is then switched from helium to NO (at a flow rate of 7-9 sccm) with the flow rate controlled by a Dwyer flowmetter, and the mass change is recorded as a function of time. When the mass change stabilizes, the flow-gas is switched back to helium (15 sccm), causing a step decrease in mass which is partly caused by the lower density of helium and partly due to desorption of adsorbed species. The net mass gain of the sample is determined from a stable mass reading for at least 15 min following the switch from NO to He flow.

The purge gas (He flowing at 21.5 sccm) is continuously sent through a Books mass flow controller throughout the entire experiment. A pressure transducer was placed immediately before gas entrance into the TEOM to measure the pressure upstream of the packed bed. The other pressure transducers were used to balance the pressure when switching between He and NO.

Labeling Studies. These studies used ^{14}NO or ^{15}NO generated using the method reported by Mattson.[16] The NO producing site consisted of a 2-neck 100 mL round-bottom flask (NO-generating RBF) that was equipped with a stopcock and a 60 mL additional funnel. This flask was charged with 0.5 g of $NaNO_2$ ($Na^{15}NO_2$ for ^{15}NO) and the additional funnel contained 10 mL of acidic $FeSO_4$. The set-up was evacuated for 15 min, purged with N_2 for 15 min, and then sealed. $[Co^{II}(salen)]_P$ (8 mg) was placed between two cotton balls and inserted inside a 5 cm glass tube that was then positioned via 3/8" Tygon tubing between the NO-generating RBF and a 2-neck 500 mL flask (equipped with a stopcock in one neck). In a typical experiment, the sample and a second RBF were placed under a dynamic vacuum for 15 min and then sealed via a stopcock. The acidic $FeSO_4$ solution was subsequently added to $NaNO_2$ and allowed to react for ~ 3 min, after which the NO-generating RBF was opened to the rest of the system for 10 min. The stopcocks were closed and the procedure was repeated using a new solution of acidic $FeSO_4$ and solid $NaNO_2$. Six independent runs were done per sample. A schematic diagram of the experiment can be found in Appendix A (Figure A-1).

Results and Discussion

NO Uptake Measurements. The uptake of NO is monitored using a tapered element oscillating microbalance (TEOM). Flowing NO over a sample of $[Co^{II}(salen)]_P$ produces a reproducible mass increase of approximately 32% (Figure 3-3), which corresponds to approximately 3.5 NO per cobalt center. This finding eliminates the simple binding of NO to each Co^{II}(salen) molecule within the particles,

as is found when the complex is in the condensed phase — a 9% mass gain would be expected from this type of uptake.

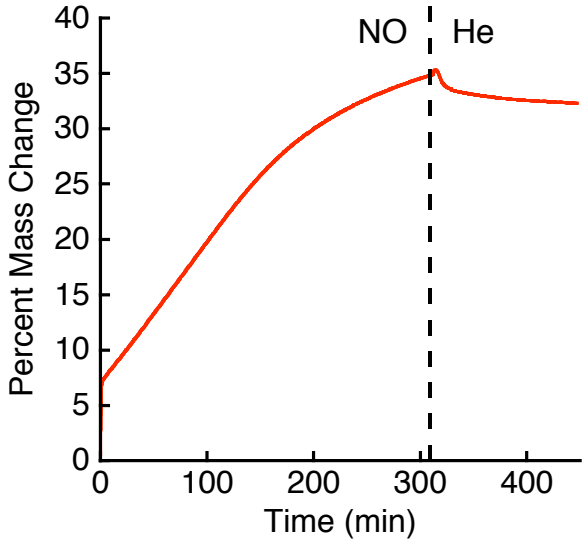

Figure 3-3. TEOM profile for NO uptake by $[Co^{II}(salen)]_P$.

The larger than expected mass gain with NO is specific for $[Co^{II}(salen)]_P$. Under the same experimental conditions, TEOM measurements of unprocessed $Co^{II}(salen)$ shows less than a 0.5% mass change in the presence of NO (Figure 3-4a). This finding supports previous observations that $Co^{II}(salen)$ normally does not interact with NO in the solid state. In addition, the large mass change is not attributed solely to the morphology of the nanoparticles. The structurally identical nanoparticles of $Ni^{II}(salen)$ ($[Ni^{II}(salen)]_P$) display a mass change of less than 0.8% when exposed to flowing NO in a TEOM (Figure 3-4b). This result is in accordance to the known chemistry of $Ni^{II}(salen)$, which does not bind NO in either the solution or solid state.

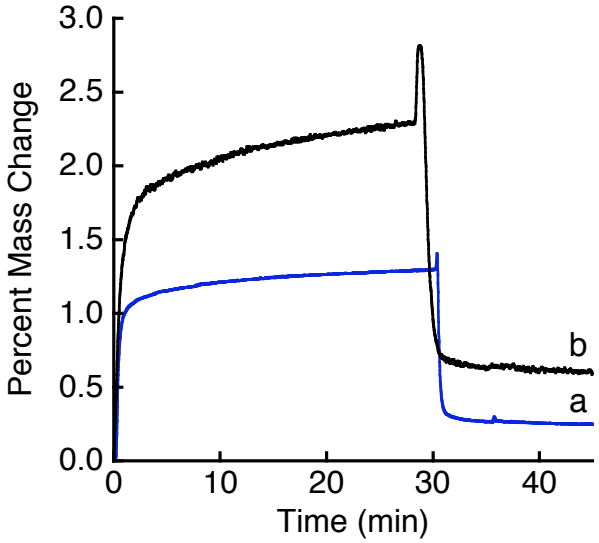

Figure 3-4. TEOM profile for the uptake of NO by (a) unprocessed Co^{II}(salen) (—) and (b) $[Ni^{II}(salen)]_P$ (—).

Analytical data obtained from elemental analyses supports the large mass change observed from NO-exposed $[Co^{II}(salen)]_P$ (Table 3-1). The elemental compositions of $[Co^{II}(salen)]_P$ and its unprocessed analog are identical within measurement accuracy, and agree closely with the calculated theoretical percentages. Similar results are found for unprocessed Co^{II}(salen) and NO-treated Co^{II}(salen), again indicating that the complex does not bind NO in the solid state. In contrast, there is a large change in the elemental percentages for $[Co^{II}(salen)]_P$ when exposed to flowing NO. The percentage of nitrogen atoms changes from 8.11% to 14.63%, an increase that corresponds to the addition of 3.5 nitrogen atoms per cobalt complex, which can be attributed to the uptake of approximately four NO molecules.

Table 3-1. Results from Elemental Analyses.[a]

	%C	%H	%N	%Co	# of N-atoms
Co^{II}(salen)	57.08	4.25	8.25	17.02	2.04
$[Co^{II}(salen)]_P$	56.92	4.13	8.11	16.66	2.05
Co^{II}(salen) + NO	58.16	4.24	8.45	16.17	2.20
$[Co^{II}(salen)]_P$ + NO	35.36	2.18	14.63	10.83	5.68

[a] Calculated values for Co^{II}(salen): %C, 59.09; %H, 4.35; %N, 8.61; %Co, 18.12

FTIR Spectroscopy Analyses. One possible explanation for the observed mass gain is that $[Co^{II}(salen)]_P$ converts NO into other species, such as N_2O, NO_2, and N_2.[18] To probe this possibility, we have examined the vibrational properties of the nanoparticles using Fourier transformed infrared (FTIR) spectroscopy (Figure 3-5). Several new bands are present in samples treated with flowing NO that are assigned to nitrogen-based products (Figure 3-5b): N_2O (2210 cm^{-1}),[19] N_2 (2170 cm^{-1}),[20] and NO_2 (1580 cm^{-1}).[21] In addition, the peak at 1640 cm^{-1} is similar to signals found in complexes with Co—NO units.[11] The features disappear when the NO-exposed nanoparticles are heated under vacuum for 2 h, producing a FTIR spectrum approaching that of $[Co^{II}(salen)]_P$ (Figure 3-5c).

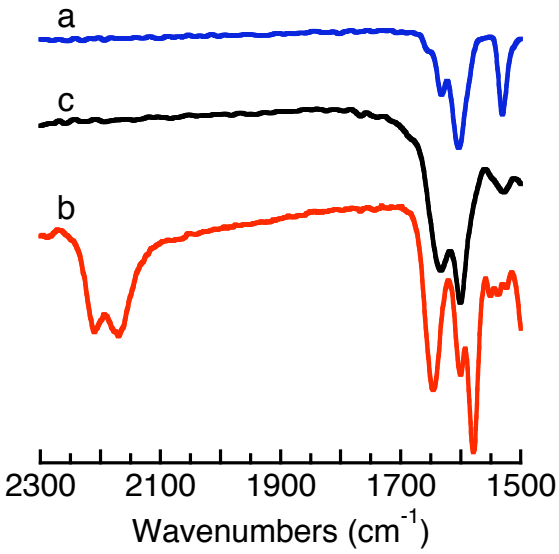

Figure 3-5. FTIR spectra (KBr pellets) of (a) $[Co^{II}(salen)]_P$ (—), (b) $[Co^{II}(salen)]_P$ + NO (—), and (c) NO-exposed $[Co^{II}(salen)]_P$ placed under vacuum at 120°C for 2 h (—).

Isotopic labeling studies with ^{15}NO provide further evidence to support the formation of N_2O and N_2. The bands at 2210 and 2170 cm^{-1} are replaced with a broad band centered at 2110 cm^{-1} in the ^{15}NO treated nanoparticles, which is attributed to overlapping vibrations from $^{15}N_2$ and $^{15}N_2O$ (Figure 3-6). The observed shifts are expected based on a classical harmonic N—N oscillator model that predicts each band should be lowered in energy by ~75 cm^{-1}. Similar shifts have been observed for these isotopomers in cobalt and iron tropocoronand complexes.[19-20] In addition, the band at 1640 cm^{-1} shifts a small amount to 1635 cm^{-1} in the ^{15}N-isotopomer, which is substantially smaller than the predicted value of 30 cm^{-1} for $\nu(^{15}NO)$. Even though there is currently no explanation as to why such a relatively small shift is observed, this change indicates that the vibration is sensitive to the isotope of nitrogen in the sample.

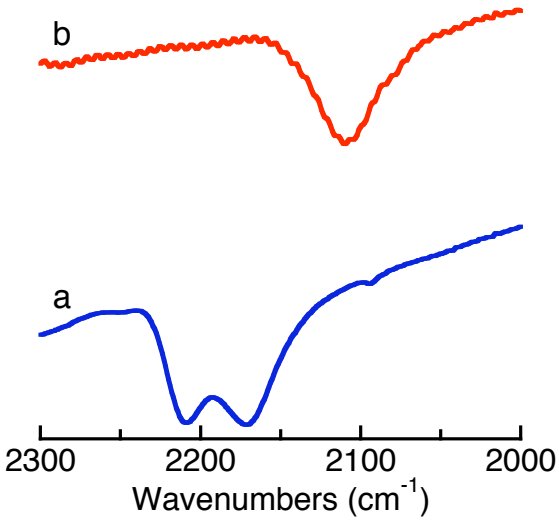

Figure 3-6. FTIR spectra (KBr pellet) of (a) $[Co^{II}(salen)]_P$ + ^{14}NO (—) and (b) $[Co^{II}(salen)]_P$ + ^{15}NO (—).

$[Co^{II}(salen)]_P$ does not bind to N_2 or N_2O when exposed to either gas, providing further evidence that both gases are formed during the disproportionation of NO. No color changes are observed when the nanoparticles are exposed to either gas, which is different from the color changed observed when $[Co^{II}(salen)]_P$ is exposed to NO. Also, the FTIR spectra for the N_2 and N_2O-exposed nanoparticles are identical to the FTIR spectrum for $[Co^{II}(salen)]_P$ (Figure A-2).

Effects of NO Exposure on Morphology and Structure of $[Co^{II}(salen)]_P$. Results from the NO uptake studies suggest that nearly all the metal sites are accessible for reactivity. This finding agrees with the microscopy results (Chapter 2) that suggest $[Co^{II}(salen)]_P$ has a layered structure. The uptake studies also imply that the disproportionation products are bound within $[Co^{II}(salen)]_P$. Thus, a variable of concern is the effect of the adsorbed species on the morphology and molecular

structure of the nanoparticles. Both microscopic techniques and PXRD are used to probe this concern.

The majority of $[Co^{II}(salen)]_P$ appears to maintain their rodlike morphology after NO exposure (Figure 3-7a). The lamellar structure also appears to stay intact with the presence of the two core molecular structure (Figure 3-7b). The inner core appears to be darker, which means it is more dense in that area, but without sonicating the samples, any changes in the molecular structure are difficult to determine using TEM. These microscopy results are similar to those found for unexposed $[Co^{II}(salen)]_P$ (Chapter 2).

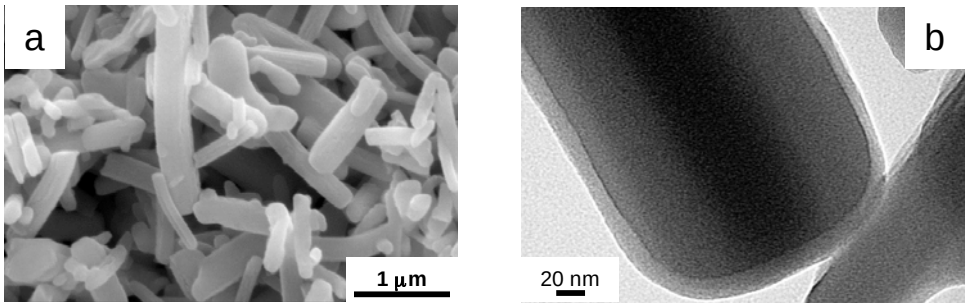

Figure 3-7. Images of $[Co^{II}(salen)]_P$ after NO exposure utilizing (a) SEM and (b) TEM.

Data from PXRD studies show that the crystalline lattices of $[Co^{II}(salen)]_P$ change after exposure to NO (Figure 3-8a). Four new diffraction peaks appear when compared with $[Co^{II}(salen)]_P$, and they are not different orders of Bragg diffraction peaks (Table 3-2). Interestingly, two of the diffraction peaks show smaller lattice planes than the 12.5 Å and 12.8 Å lattice planes of $[Co^{II}(salen)]_P$ and unprocessed $Co^{II}(salen)$, respectively. These results are counterintuitive because quantitative NO uptake measurements would predict larger lattice planes from the additional absorbed

species. Normally, the crystalline shape could be determined from the PXRD data; however, the software could not find an appropriate match. A possible explanation for this result is the existence of more than one crystalline phase because the computer software is programmed to assume that only one crystalline phase is present. Since various NO disproportionation products stay bound to the material, there is a high possibility that more than one crystalline phase exists.

Table 3-2. PXRD data for NO-exposed $[Co^{II}(salen)]_P$.

d (Å)	1st Order (2θ)		2nd Order (2θ)		3rd Order (2θ)	
	Calculated	Observed	Calculated	Observed	Calculated	Observed
9.454	—	9.347	18.757	20.305	28.297	29.042
8.644	—	10.225	20.532	20.305	—	—
6.251	—	14.158	28.538	29.042	—	—
5.984	—	24.792	29.838	31.247	—	—

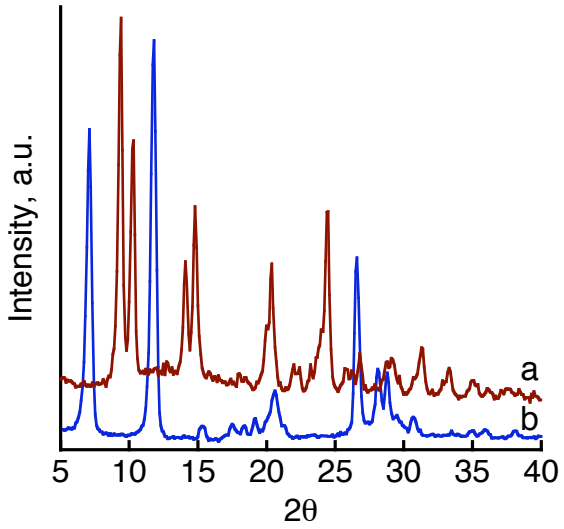

Figure 3-8. PXRD data of (a) NO-exposed $[Co^{II}(salen)]_P$ and (b) $[Co^{II}(salen)]_P$.

Summary and Conclusions

The kinetics of NO binding to $[Co^{II}(salen)]_P$ could not be determined because the nanoparticles catalyze the disproportionation of NO, which is supported by

analytical data from elemental analyses and FTIR spectroscopy. There are examples of other metal-based systems that display the same reactivity toward NO as $[Co^{II}(salen)]_P$,[22] but the only systems that disproportionates NO at room temperature involving cobalt complexes occur in the condensed phase.[20b, 23] To our knowledge, the systems that disproportionate NO require elevated temperatures, usually above 400°C.

In conclusion, unprocessed $Co^{II}(salen)$ clearly *does not bind* NO, illustrating a new functional property of $[Co^{II}(salen)]_P$ compared to its molecular precursor. The new NO reactivity in $[Co^{II}(salen)]_P$ is partly due to its four-coordinate nature;[24] however, the cause(s) of how the disproportionation products stay absorbed to $[Co^{II}(salen)]_P$ is not understood. Nonetheless, these findings show that this bottom up approach of fabricating nanoparticulates of metal complexes produces systems that have distinct structural and functional properties.

References

1. Miller, M. R.; Megson, I. L. *Br. J. Pharmacol.* **2007**, *151*, 305-321.

2. (a) *Nitric Oxide: Biology and Pathobiology*; Ignarro, L. J., Ed.; Academic Press: San Diego, 2000. (b) *Nitric Oxide: Principles and Actions*; Lancaster, J., Ed.; Academic Press: San Diego, 1996.

3. Wink, D. A.; Mitchell, J. B. *Free Radical Biol. Med.* **1998**, *25*, 434-456.

4. For reviews see: (a) Wu, Y.; Meyerhoff, M. E. *Talanta* **2008**, *75*, 642-650. (b) Hetrick, E. M.; Schoenfisch, M. H. *Chem. Soc. Rev.* **2006**, *35*, 780-789. (c) Shin, J. H.; Schoenfisch, M. H. *Analyst* **2006**, *131*, 609-615. (d) Frost, M. C.; Reynolds, M. M.; Meyerhoff, M. E. *Biomaterials* **2005**, *26*, 1685-1693. (e) Reynolds, M. M.; Frost, M. C.; Meyerhoff, M. E. *Free Radical Biol. Med.* **2004**, *37*, 926-936.

5. (a) Shami, P. J.; Saavedra, J. E.; Bonifant, C. L.; Chu, J.; Udupi, V.; Malaviya, S.; Carr, B. I.; Kar, S.; Wang, M.; Jia, L.; Ji, X.; Keefer, L. K. *J. Med. Chem.* **2006**, *49*, 4356-4366. (b) Zhang, C. X.; Lippard, S. J. *Curr. Opin. Chem. Biol.* **2003**, *7*, 481-489. (c) Yamamoto, T.; Bing, R. J. *P.S.E.B.M.* **2000**, *225*, 200-206.

6. Mitchell-Koch, J. T.; Reed, T. M.; Borovik, A. S. *Angew. Chem., Int. Ed.* **2004**, *43*, 2806-2809.

7. (a) Eroy-Reveles, A. A.; Leung, Y.; Beavers, C. M.; Olmstead, M. M.; Mascharak, P. K. *J. Am. Chem. Soc.* **2008**, *130*, 4447-4458. (b) Halpenny, G. M.; Olmstead, M. M.; Mascharak, P. K. *Inorg. Chem.* **2007**, *46*, 6601-6606. (c) Eroy-Reveles, A. A.; Leung, Y.; Mascharak, P. K. *J. Am. Chem. Soc.* **2006**, *128*, 7166-7167. (d) Bordini, J.; Ford, P. C.; Tfouni, E. *Chem. Commun.* **2005**, 4169-4171.

8. (a) Ribeiro, J. M.; Hazzard, J. M.; Nussenzveig, R. H.; Champagne, D. E.; Walker, F. A. *Science* **1993**, *260*, 539-541. (b) Ding, X. D.; Weichsel, A.; Andersen, J. F.; Shokhireva, T. K.; Balfour, C.; Pierik, A. J.; Averill, B. A.; Montfort, W. R.; Walker, F. A. *J. Am. Chem. Soc.* **1999**, *121*, 128-138. (c) de Leo, M.; Ford, P. C. *J. Am. Chem. Soc.* **1999**, *121*, 1980-1981.

9. Padden, K. M.; Krebs, J. F.; MacBeth, C. E.; Scarrow, R. C.; Borovik, A. S. *J. Am. Chem. Soc.* **2001**, *123*, 1072-1079.

10. (a) *Nitric Oxide and Infection*; Fang, F. C., Ed.; Kluwer Academic/Plenum Publishers: New York, 1999. (b) Toda, N.; Nakanishi-Toda, M. *Prog. Retinal Eye Res.* **2007**, *26*, 205-238.

11. Clarkson, S. G.; Basolo, F. *Inorg. Chem.* **1973**, *12*, 1528-1534.

12. The only references on NO binding to solid Co^{II}(salen) contain limited information on the properties and formulation of the final complexes: (a) Diehl, H.; Hach, C. C.; Harrison, G. *Iowa St. Coll. J. Sci.* **1947**, *21*, 287-309. (b) Earnshaw, A.; Hewlett, P. C.; Larkworthy, L. F. *Chem. Soc.* **1965**, 4712-4723.

13. Johnson, C. A.; Sharma, S.; Subramaniam, B.; Borovik, A. S. *J. Am. Chem. Soc.* **2005**, *127*, 9698-9699.

14. For examples see: (a) Roco, M. C. In *Handbook of Nanoscience, Engineering, and Technology*; Goddard, W. A., Brenner, D. W., Lyshevski, S. E., Iafrate, G. J., Eds.; CRC Press: Boca Raton, 2007, pp 3.1-3.26. (b) *Nanotechnology in Catalysis*; Zhou, B.; Han, S.; Raja, R., Eds.; Springer: New York, 2007. (c) Foster, L. E. *Nanotechnology: Science, Innovation, and Opportunity*; Prentice Hall: Upper Saddle River, 2006.

15. See for example, Zhu, W.; van de Graaf, J. M.; van den Broeke, L. J. P.; Kapteijn, F.; Moulijn, J. A. *Ind. Eng. Chem. Res.* **1998**, *37*, 1934-1942.

16. Mattson, B. M. Microscale Gas Chemistry. Educational Innovations, Norwalk, **2003**.

17. Zhu, W.; van de Graaf, J. M.; van den Broeke, L. J. P.; Kapteijn, F.; Moulijn, J. *Ind. Eng. Chem. Res.* **1998**, *37*, 1934-1942.

18. Tsukahara, H.; Ishida, T.; Todoroki, Y.; Hiraoka, M.; Mayumi, M. *Free Radical Res.* **2003**, *37*, 171-177.

19. Franz, K. J.; Lippard, S. J. *J. Am. Chem. Soc.* **1999**, *121*, 10504-10512.

20. (a) Franz, K. J.; Doerrer, L. H.; Spingler, B.; Lippard, S. J. *Inorg. Chem.* **2001**, *40*, 3774-3780. (b) Hilderbrand, S. A.; Lippard, S. J. *Inorg. Chem.* **2004**, *43*, 4674-4682.

21. (a) Shimokawabe, M.; Okumura, K.; Ono, H.; Takezawa, N. *React. Kinet. Catal. Lett* **2001**, *73*, 267-274. (b) Minming, H.; Chunhua, Y.; Kunsong, C. *J. Mol. Catal.* **1991**, *69*, L7-L13. (c) Agnew, S. F.; Swanson, B. I.; Jones, L. H.; Mills, R. L. *J. Phys. Chem.* **1985**, *89*, 1678-1682. (d) Chao, C.-C.; Lunsford, J. H. *J. Amer. Chem. Soc.* **1971**, *93*, 71-77. (e) Nakamoto, K. *Infrared and Raman Spectra of Inorganic and Coordination Compounds, Part B: Applications in Coordination, Organometallic, and Bioinorganic Chemistry*, 5th ed.; John Wiley & Sons, Inc.: New York, 1997.

22. (a) Chang, Y. F.; McCarty, J. G. *J. Catal.* **1998**, *178*, 408-413. (b) Bell, A. T. *Catal. Today* **1997**, *38*, 151-156. (c) Armor, J. N. *Catal. Today* **1995**, *26*, 147-158. (d) Iwamoto, M.; Yokoo, S.; Sakai, K.; Kagawa, S. *J. Chem. Soc., Faraday Trans. 1* **1981**, *77*, 1629-1638.

23. (a) Potter, W. T.; Cho, J.; Sublette, K. L. *Fuel Process. Technol.* **1994**, *40*, 355-360. (b) Rossi, M.; Sacco, A. *J. Chem. Soc. D* **1971**, 694. (c) Miki, E.; Tanaka, M.; Saito, K.; Maejima, T.; Mizumachi, K.; Ishimori, T. *Bull. Chem. Soc. Jpn.* **1985**, *58*, 1642-1645.

24. Johnson, C.; Long, B.; Nguyen, J. G.; Day, V. W.; Borovik, A. S.; Subramaniam, B.; Guzman, J. *J. Phys. Chem. C* **2008**, *112*, 12272-12281.

CHAPTER FOUR

REVERSIBLE DIOXYGEN BINDING BY A NANOPARTICULATE COBALT(II) COMPLEX

Introduction

Synthetic dioxygen carriers have long been studied because they are important models for biological systems.[1] Proteins that can bind, transport, store, and release O_2 are of critical importance to nearly all forms of animal life because dioxygen is required for various oxidation processes. The study of model complexes helps provide valuable insight for biochemists that are interested in the details of dioxygen binding and transport.[1-2]

Industrial chemists have tried to utilize these model complexes to separate O_2 from air, which is predominately done using cryogenic distillation.[1, 3] For example, the military has attempted to develop onboard oxygen delivery systems but have been hampered by the metal complexes' long-term chemical instability. Other methods for the purification of O_2 have also proven to be ineffective due to instabilities and/or inadequate O_2-binding capacity.

One of the most common metal complexes that has been studied as a synthetic dioxygen carrier is Co^{II}(salen) (salen, *N*,*N*'-salicylidiene-1,2-ethylene-diaminato(2-)) and its various derivatives (Figure 4-1). Four-coordinate Co^{II} complexes are very poor dioxygen binders, whereas five-coordinate Co^{II} complexes readily bind O_2 at

ambient pressures of oxygen.[1a-b, 4] When a fifth ligand binds to the axial position, the square-pyramidal coordination geometry provides the correct electronic configuration for O_2 binding: the energy of the d_{z^2} orbital needs to be raised above that of the d_{xy} orbital to give a $(d_{xz})^2(d_{yz})^2(d_{z^2})^1$ configuration.[1a, b] Scheme 4-1 illustrates this concept for the solution chemistry of Co^{II}(salen).[4-5] Four-coordinate Co^{II}(salen) also weakly binds pyridine under anaerobic conditions but readily forms the tertiary Co(salen)(py)(O_2) complex in the presence of dioxygen.

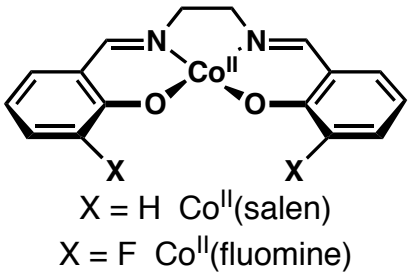

Figure 4-1. Co^{II}(salen) and one of its derivatives, Co^{II}(fluomine)

Sharma and coworkers have illustrated this concept within an organic polymeric host.[4] In this study, key endogenous ligands, salen and pyridine, are covalently bound in the correct locations within the porous organic host to help form immobilized Co^{II} complexes (Scheme 4-2). The equilibrium between four and five-coordinate Co^{II} complexes found for the polymer is similar to the equilibrium in the solution phase.[5] Since the pyridine ligand is immobilized in close proximity to the immobilized Co^{II} complexes, the polymer quickly and reversibly binds dioxygen, which emphasizes the importance of the fifth ligand for O_2 binding.

Scheme 4-1[a]

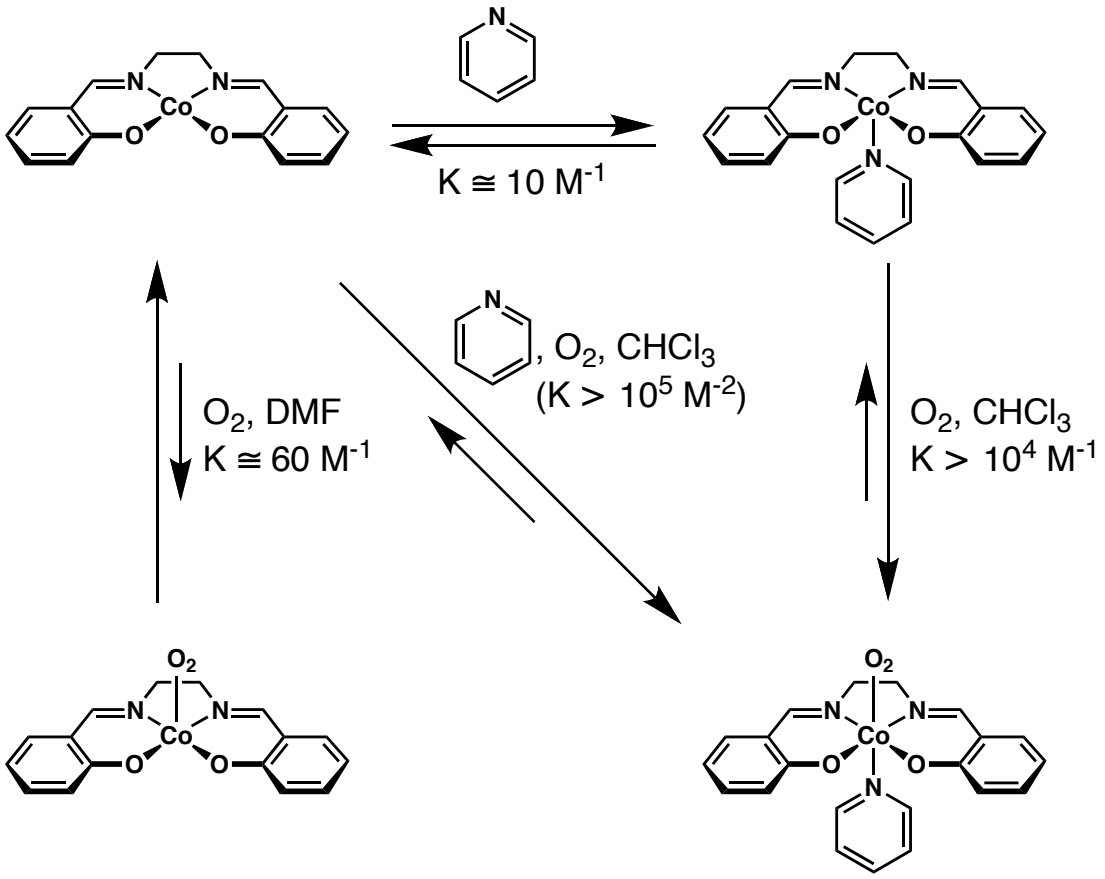

[a] Taken from ref 6.

Scheme 4-2[a]

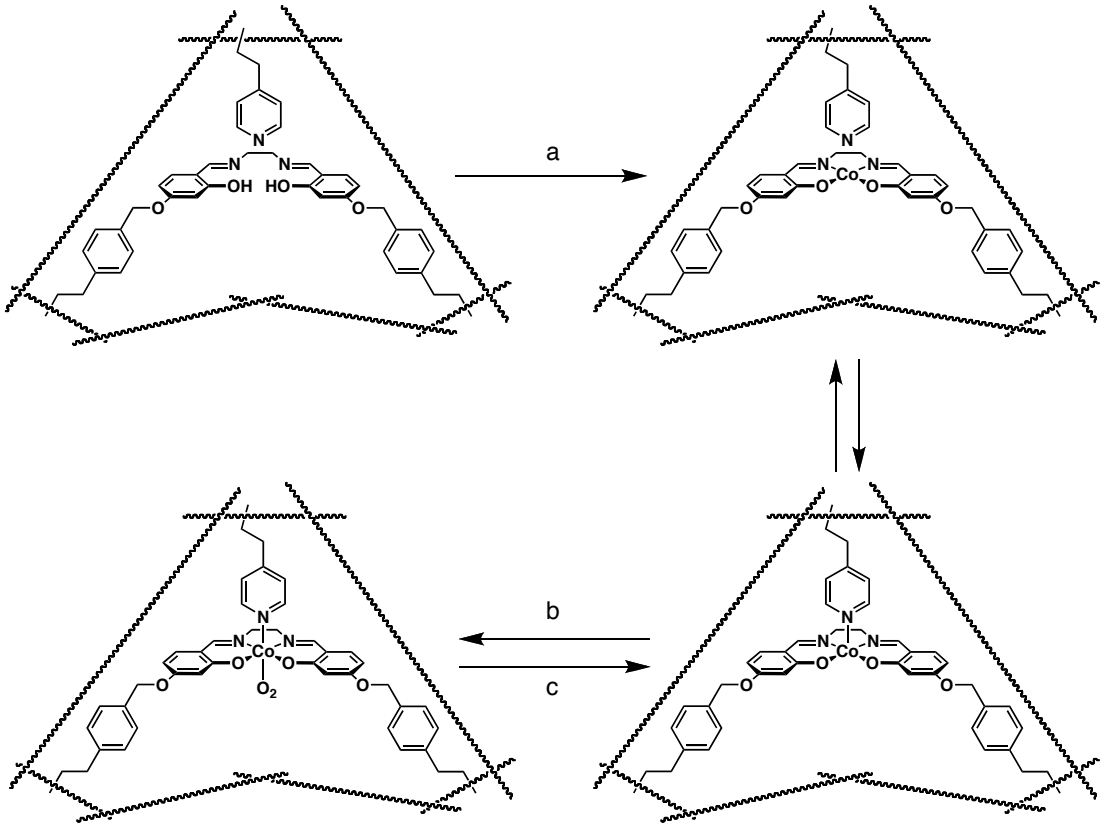

[a] Conditions: (a) $Co(OAc)_2$, MeOH, Ar, 6 h; (b) O_2, CH_3NO_2; (c) N_2, CH_3NO_2.

Since dioxygen binds to Co^{II}(salen) poorly, there is a question of whether there will be improved reactivity towards O_2 utilizing Co^{II}(salen) nanoparticles ($[Co^{II}(salen)]_P$) produced by the precipitation with compressed antisolvent (PCA) technology, whose preparation and properties were discussed in Chapter 2. This chapter discusses studies used to observe the interactions of unprocessed and processed Co^{II}(salen) complexes with dioxygen utilizing a tapered element oscillating microbalance (TEOM). The chapter also details the experiments used to determine

the product of this reaction. Finally, a brief discussion on the morphological and structural effects of the nanoparticles upon O_2 binding is discussed.

Experimental Section

General Methods. Unprocessed Co^{II}(salen) was purchased from Sigma-Aldrich and labeled $^{18}O_2$ (99 atom % ^{18}O) was purchased from Icon Isotopes. Literature methods were used to synthesize $[Co^{II}(salen)]_P$.[6] Ultra-high purity helium, dioxygen, and argon (99.996%) were purchased from Airgas.

Physical Methods. Fourier transform infrared (FT-IR) spectra were collected on a Mattson Genesis series or a Varian Scimitar 800 series FTIR instrument with values reported in wavenumbers. The samples were prepared as KBr pellets.

A SpectraPro SP-2356 imaging spectrograph (600/1200/2400 g/mm; Princeton Instruments – Acton; Acton, MA) equipped with a CCD camera (1,024 x 256 pixels; Princeton Instruments – Acton; Acton, MA) was used to collect the Raman spectra. The 532.43 nm excitation source was provided by a 130 mW diode pulsed solid-state laser (Snake Creek Lasers, Halstead, PA). The 1200 gr/mm gratings provided an instrumental resolution of 5.7 cm^{-1} (1.9 cm^{-1} per CCD pixel). The samples were prepared as KBr pellets.

Scanning electron micrographs were acquired on a Schottky thermal field emission FEI/Philips XL-30FEG operating at an accelerating voltage of 10.0 kV. SEM samples were prepared by sprinkling the sub-micron particles directly onto a conductive carbon tab (Ted Pella, Inc. Part # 16084-1) attached to a 12.7 mm diameter aluminum specimen mount (Ted Pella, Inc. Part # 16111) and pressed down.

The sample was then sputter-coated with a 3 nm thick Au-Pd alloy coat by using a Polaron SC7600 operating at 53 mTorr and 5 mA.

Transmission electron micrographs were acquired using a FEI/Philips CM-20 microscope operating at 200 kV. The samples were prepared pressing a small amount of the nanoparticles onto the copper grid. The transmission electron microscope was also equipped with an energy-dispersive spectrometer (EDAX/4pi) system.

Powder X-ray diffraction (PXRD) experiments were performed using a Rigaku D/Max 2200PC Ultima III multipurpose powder diffractometer with graphite-monochromated Cu Kα radiation. X-rays were provided by a normal-focus sealed X-ray tube operated at 40 kV and 40 mA. Scans were taken with an increment size of 0.05° over a range of 2Θ from 5° to 70°.

Tapered Element Oscillating Microbalance (TEOM). A Rupprecht & Patashnick TEOM 1500 mass analyzer (100 μL sample volume) was used to obtain continuous adsorption data at room temperature. Figure 3-1 contains a schematic of the experimental setup—a detailed analysis of the TEOM operating principles has been reported;[7] only a brief description of the procedure is described here. Initially, a baseline is determined by flowing helium (15 sccm) through the instrument with sample in place until a stable output is achieved. The flow gas is then switched from helium to O_2 (at a flow rate of 7 sccm) and the mass change is recorded as a function of time. When the mass change stabilizes, the flow-gas is switched back to helium (15 sccm), causing a step decrease in mass which is partly caused by the lower density of helium and partly due to desorption of adsorbed species. The net mass

gain of the sample is determined from a stable mass reading for at least 15 min following the switch from O_2 to He.

O_2 Binding Experiments. Two different methods were used to bind dioxygen to $[Co^{II}(salen)]_P$. The first method involved exposing the nanoparticles to the atmosphere for at least 24 h, which resulted in dark green particles. The second method involved placing $[Co^{II}(salen)]_P$ (8 mg) between two cotton balls inside a 5 cm glass tube. The glass tube was then attached to a tank of O_2 via Tygon tubing. Finally, dioxygen flowed through the sample for at least 30 min, which also resulted in dark green particles.

Labeling Studies. A 25 mL Schlenk flask containing a small amount of $[Co^{II}(salen)]_P$ was evacuated for approximately 15 min. The flask was then filled with N_2 and then evacuated; this procedure was repeated two more times. $^{18}O_2$ was added to the flask while the flask was under static vacuum. The flask was kept under a positive pressure of $^{18}O_2$ overnight, resulting in nanoparticles turning from brown to dark green.

Results and Discussion

O_2 Binding. When $[Co^{II}(salen)]_P$ is processed using PCA technology, the nanoparticles are brown (Figure 4-2a). The nanoparticles will turn dark green within a day when it is exposed to the atmosphere (Figure 4-2b). These initial results were a little surprising because $[Co^{II}(salen)]_P$ within the nanoparticles were thought to have only four-coordinate Co^{II} centers (see introduction).[8] Note that the nanoparticles will

stay brown as long as it is kept under an inert atmosphere, such as argon or dinitrogen.

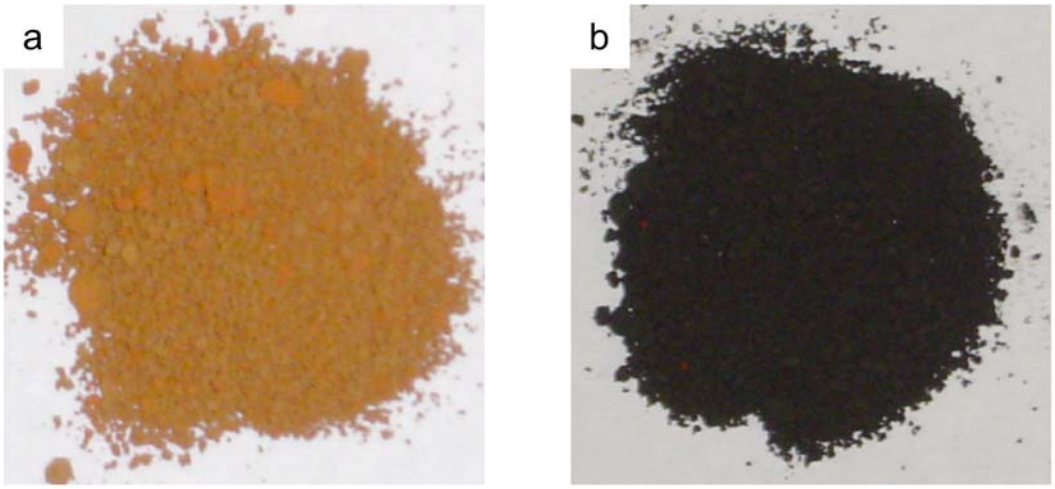

Figure 4-2. Observed colors of (a) $[Co^{II}(salen)]_P$ and (b) $[Co^{II}(salen)]_P$ exposed to dioxygen.

O_2 Uptake Measurements using a TEOM. Before NO and O_2 uptake studies with nanoparticles were performed, the use of a tapered element oscillating microbalance (TEOM) had mainly been limited to porous materials.[9] Even though nano-sized metal catalysts supported on magnesium powder have been studied with a TEOM,[10] it still was an under-utilized method for measuring gas uptake by nanoparticles prior to our investigations. One possible reason for this under-utilization is that the small size of the nanoparticles may create pressure and packing density issues, which affects the mass change observed by affecting the frequency of the tapered element.

Initial uptake measurements showed decreases in the O_2 flow-rates. The pressure immediately upstream of the TEOM (Figure 3-1), which is known as the back-pressure, also decreased. When the flow rate was increased to its initial rates,

there was an increase in the mass change and back-pressure (Figure 4-3). When the flow gas was switched back to He, the mass change slowly tapers off in correlation to the observed decrease in pressure. In order to understand these back-pressure measurements, experiments were performed on unprocessed Co^{II}(salen) to determine a correlation between flow rates and the mass change observed because back-pressures are not observed during the measurement with these larger particles. An increase in the mass change is observed anytime the flow rates are increased (Figure B-1). Thus, studies were done to make sure that the O_2 flow-rate remained constant throughout the measurement.

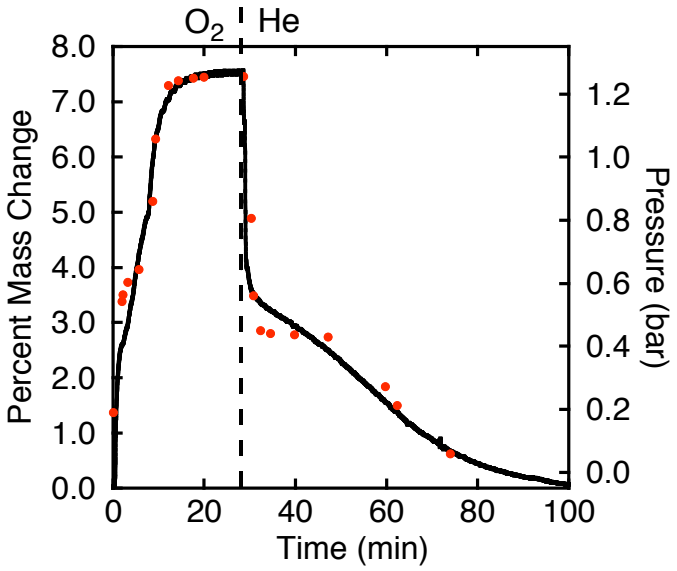

Figure 4-3. Initial TEOM profile for O_2 uptake by $[Co^{II}(salen)]_P$. The red dots are the corresponding pressure profiles.

When unprocessed Co^{II}(salen), $[Co^{II}(salen)]_P$, and $[Ni^{II}(salen)]_P$ are exposed to the same constant flow-rates of O_2, it appears that only $[Co^{II}(salen)]_P$ binds dioxygen based on the tapered profile (Figure 4-4a). However, the back-pressure for $[Co^{II}(salen)]_P$ also tapers off (Figure 4-4b), which caused some concern in the

measurement. The back-pressure for $[Ni^{II}(salen)]_P$ does not reach 0 bar, but it does return quickly to the initial pressure. The slow decrease in the back-pressure made it difficult to determine whether the TEOM profiles with O_2 were real or an instrumental artifact.

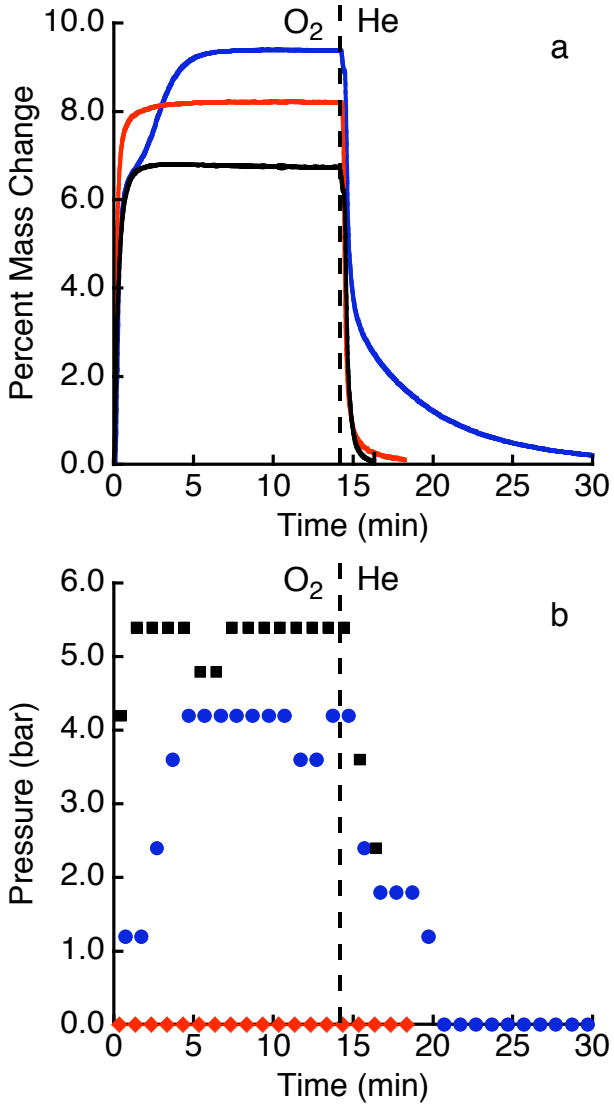

Figure 4-4. (a) TEOM profiles for O_2 uptake by $[Co^{II}(salen)]_P$ (—), Unprocessed $Co^{II}(salen)$ (—), and $[Ni^{II}(salen)]_P$ (—) and (b) the corresponding pressure profiles for $[Co^{II}(salen)]_P$ (●), $Co^{II}(salen)$ (♦), and $[Ni^{II}(salen)]_P$ (■).

The back-pressure varied slightly between nanoparticulate runs because it was difficult to pack every sample (packing density) exactly the same. Our qualitative findings indicated that higher back-pressures were observed when the nanoparticles were packed very tightly. Furthermore, desorption times were increased for the higher packed samples (Figure 4-5) because higher back-pressures took longer to reach 0 bar. Again, this TEOM profile could be artificial because of an increased back-pressure; it should be noted that the samples were light green particles, which is consistent with a small amount of dioxygen binding by $[Co^{II}(salen)]_P$.

Unfortunately, the use of a TEOM to study the uptake of dioxygen proved to be difficult. These studies were problematic because the flow-rate and pressure issues could not be decoupled. Note that these same issues did not complicate the NO uptake studies that were discussed in Chapter 3. A possible explanation for this difference is in the inherent chemical properties of the two systems: binding NO to the nanoparticles is an irreversible process, whereas O_2 binding is reversible. Varying NO flow-rates and pressure issues did not interfere with the final mass change reading because it could be recorded under flowing He. Because $[Co^{II}(salen)]_P$ reversibly binds O_2, the mass change reading would have to occur under flowing O_2, in which back-pressure issues persist. Therefore, an instrument that measures gas binding in a static system is more appropriate for quantitative studies with dioxygen.

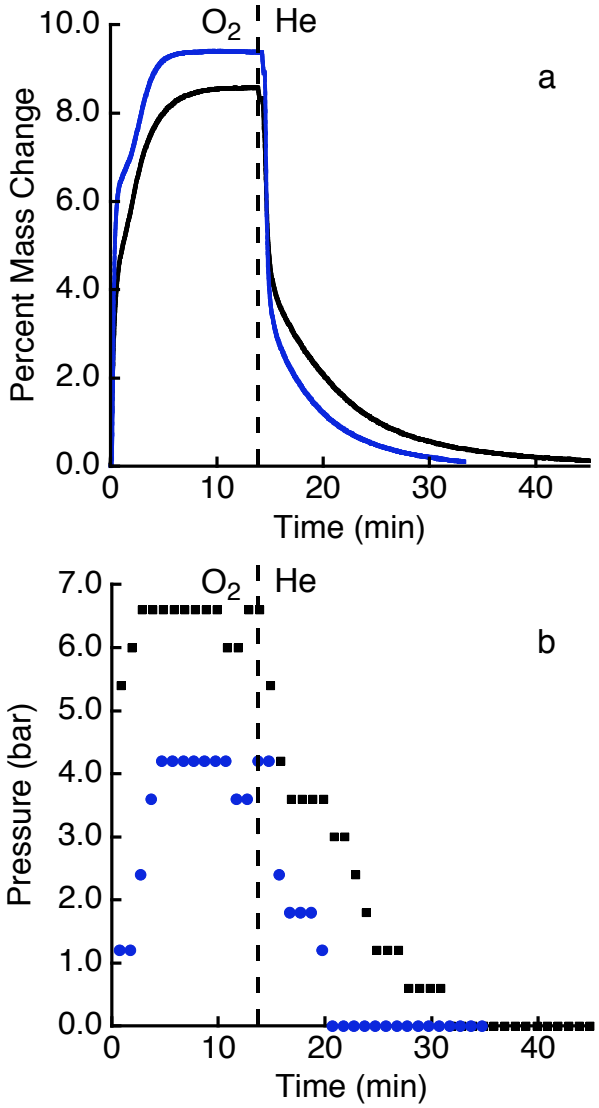

Figure 4-5. (a) TEOM profile for the uptake of O_2 by $[Co^{II}(salen)]_P$ when the they are packed normally (—) and packed very tightly (—) and (b) the corresponding pressure profiles for normal-packed $[Co^{II}(salen)]_P$ (●) and tightly-packed $[Co^{II}(salen)]_P$ (■).

Raman Spectroscopy Characterizing O_2 binding. Even though TEOM analysis could not obtain any quantitative binding data, the vibrational properties of the O_2-exposed nanoparticles were examined using Raman spectroscopy; it was anticipated that information would be obtained to support the premise that dioxygen

binds to the cobalt complexes within the nanoparticles. Raman measurements were done on a home-built spectrometer that was assembled with the help of Dr. Wytze van der Veer. A schematic diagram of the instrument is shown in Figure 4-6.

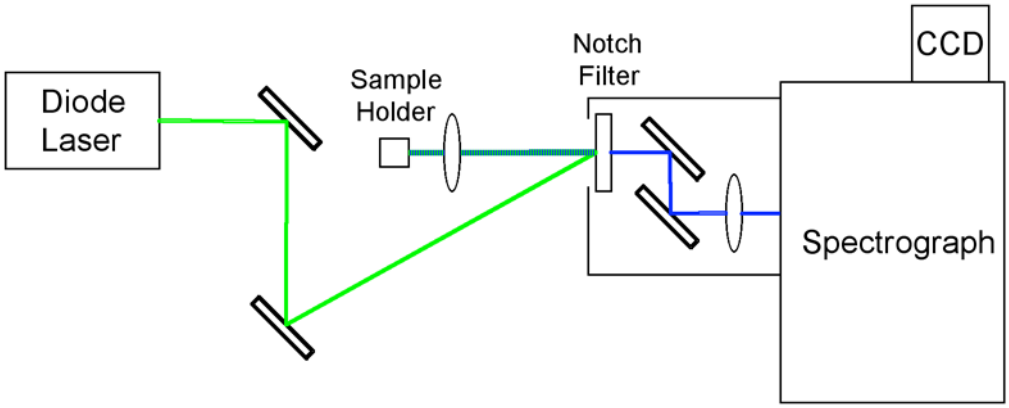

Figure 4-6. Schematic of the Raman spectrometer.

The binding of dioxygen was followed by Raman spectroscopy (Figure 4-7). Several new bands are present for the dioxygen-treated $[Co^{II}(salen)]_P$ (Figure 4-7b): 368, 547, 1046, and 1090 cm^{-1}. In addition, the intensities of these new vibrational bands decrease after purging the oxygenated samples with N_2 (Figure 4-7c). The vibrational band at 1046 cm^{-1} is in the region normally associated with bridging peroxo ligands to cobalt complexes (Figure 4-8).[11] Moreover, the band at 547 cm^{-1} is assigned to the Co—O symmetric stretches.[11b] Raman spectroscopy studies also show that dioxygen does not bind to unprocessed Co^{II}(salen) (Figure B-2), which supports previous observations that Co^{II}(salen) does not bind O_2 in the solid state.[12]

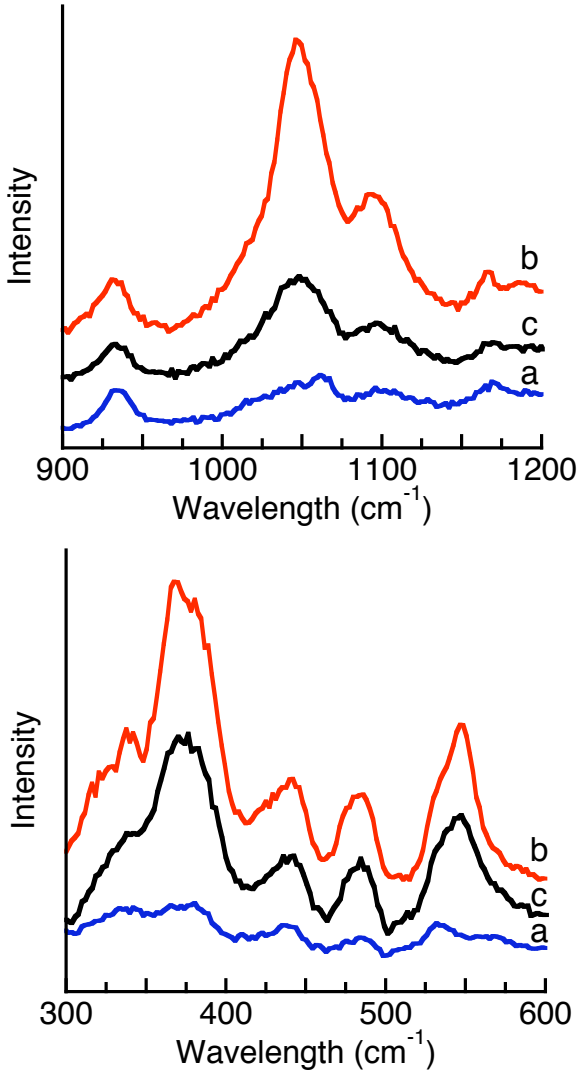

Figure 4-7. Raman spectra (KBr pellets) of (a) $[Co^{II}(salen)]_P$ (—), (b) O_2-exposed $[Co^{II}(salen)]_P$ (—), and (c) O_2-exposed $[Co^{II}(salen)]_P$ after N_2 purge (—).

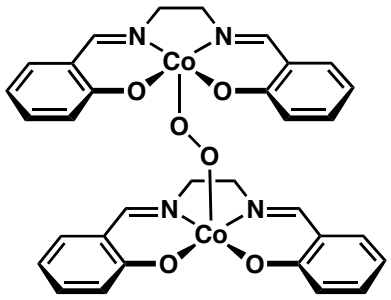

Figure 4-8. Diagram of a bridging-peroxo ligand to Co^{II}(salen).

Isotopic labeling studies also support the presence of a bridging peroxo ligand to the cobalt centers with three peaks shifting to lower energy upon treating $[Co^{II}(salen)]_P$ with $^{18}O_2$ (Figure 4-9b). In particular, the peak at 1046 cm^{-1} shifts to 986 cm^{-1}, which is predicted for a harmonic O—O oscillator ($\nu(^{16}O—^{16}O)/ \nu(^{18}O—^{18}O)$ = 1.061; calcd 1.061). The original peaks are still present because some $^{16}O_2$ leaked into the flask during the experiment. Furthermore, the 1090 cm^{-1} shifts to 1015 cm^{-1} with $^{18}O_2$ ($\nu(^{16}O—^{16}O)/ \nu(^{18}O—^{18}O)$ = 1.074; calcd 1.060) and the band at 547 cm^{-1} goes to 530 cm^{-1} ($\nu(Co—^{16}O)/ \nu(Co—^{18}O)$ = 1.032; calcd 1.046). These vibrational shifts support the premise that dioxygen binds to the cobalt complexes within the nanoparticles.

While the vibration at 1046 cm^{-1} is shown to be sensitive to dioxygen, it is slightly higher than other bridging peroxo ligands to five-coordinate cobalt complexes. However, similar vibrational frequencies have been reported for other bridging peroxo ligands to four-coordinate Co^{II} complexes.[11] These vibrational results also show that $[Co^{II}(salen)]_P$ reversibly binds O_2 because the intensities of the vibrational bands decrease after the oxygenated samples are purged with N_2. This

reversibility is supported from data obtained during desorption studies.[13] Overall, these vibrational bands provide evidence for reversible dioxygen binding to the cobalt complexes within the nanoparticles.

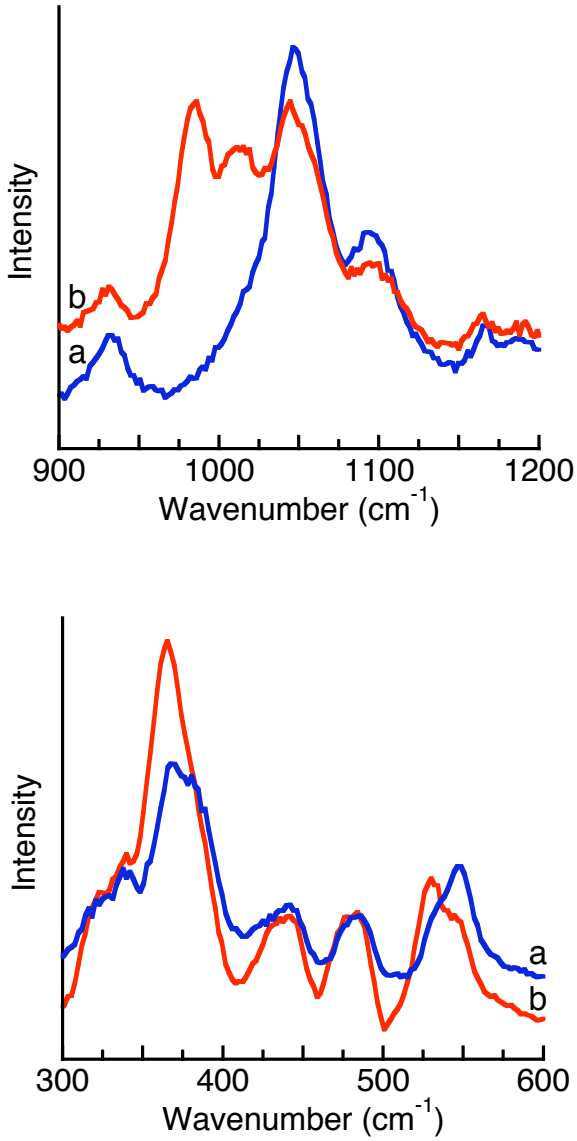

Figure 4-9. Raman spectra (KBr pellet) of (a) $[Co^{II}(salen)]_P$ + $^{16}O_2$ (—) and (b) $[Co^{II}(salen)]_P$ + $^{18}O_2$ (—).

Effects of O_2 Exposure on Morphology and Structure of $[Co^{II}(salen)]_P$. Quantitative dioxygen binding studies with $[Co^{II}(salen)]_P$ were performed by our collaborators.[14] The static dioxygen adsorption measurements were performed on a Rubotherm magnetic suspension balance, and these measurements reveal an uptake of approximately 0.491 mmol of O_2/(mmol of $[Co^{II}(salen)]_P$) at 25 °C.[15] These results are consistent with a binding stoichiometry involving a bridging peroxo ligand between two cobalt centers.[11] These results, along with the NO studies, strongly suggest that nearly all the metal sites are accessible for binding external gases. Because these complexes display unique reactivity towards dioxygen for four-coordinate Co^{II} complexes, there was a question of whether the morphology and molecular structure of the nanoparticles change during the binding event.

The morphology of $[Co^{II}(salen)]_P$ does not appear to change after exposure to O_2 based on microscopy (Figure 4-10a). The two core molecular structure also appears to stay intact (Figure 4-10b), but it is difficult to see different layers within the core with the TEM unless the samples are sonicated. Even though microscopy supplies some insight into the molecular structure of the nanoparticles, PXRD can provide additional information about the molecular structure of the O_2-exposed nanoparticles.

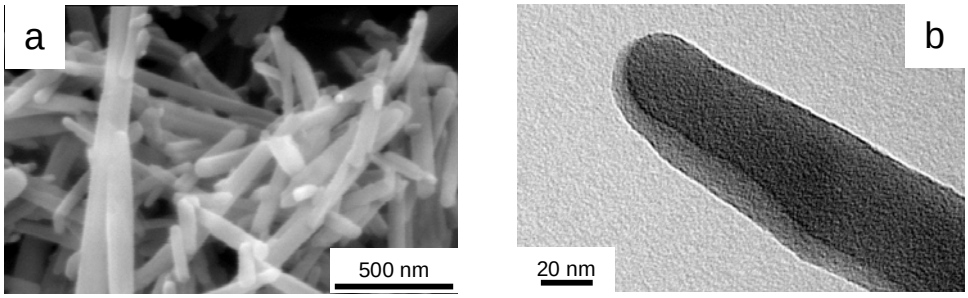

Figure 4-10. Images of $[Co^{II}(salen)]_P$ after O_2 exposure utilizing (a) SEM and (b) TEM.

The crystalline lattice of $[Co^{II}(salen)]_P$ changes minimally after exposure to dioxygen (Figure 4-11a). This is a significant finding because the Co^{II} sites need to be close enough to bind dioxygen and form the bridging peroxy complexes without major rearrangements to the molecular structure. This finding is based on the positions of the diffraction peaks in the two diffraction patterns. For instance, the diffraction peak at 11.751° shifts very slightly to 12.078° upon exposure of the nanoparticles to O_2, signifying a slight rearrangement within the lattice that is very similar to the unexposed nanoparticles. If the diffraction peak at 11.75°, which is associated with the c-axis of the unit cell (Figure 2-14), was shifted to a significantly different value, then the Co^{II} complexes would have to experience large rearrangements to accommodate the dioxygen molecules. The additional peak at approximately 25° is most likely due to the presence of disorder within the nanoparticles.

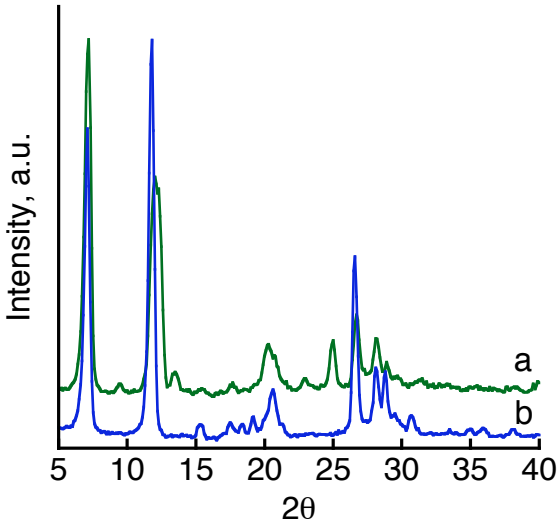

Figure 4-11. PXRD data of (a) O_2-exposed $[Co^{II}(salen)]_P$ (—) and (b) $[Co^{II}(salen)]_P$ (—).

The crystallinity of $[Co^{II}(salen)]_P$ was preserved after the nanoparticles were exposed to dioxygen, and this preservation supports the premise that the molecular structure of $[Co^{II}(salen)]_P$ is similar to unprocessed $Ni^{II}(salen)$ (as discussed in Chapter 2). Thus, a closer look at the molecular structure of unprocessed $Ni^{II}(salen)$ will provide valuable insight into the arrangement of the molecules in $[Co^{II}(salen)]_P$. The $Ni^{II}(salen)$ molecules are stacked in pairs related by a center of symmetry, with the nickel atoms 3.20 Å apart (Figure 4-12).[16] This distance is important for $[Co^{II}(salen)]_P$ to be reactive towards dioxygen because Calligaris and coworkers found that the cobalt sites are approximately 3.3 Å apart in their bridging peroxo cobalt salen complex.[17] It is also important to note that the next closest nickel atom is 4.86 Å apart, and the complexes are stacked along the c-axis (Figure 2-14), which is associated with the diffraction peak at 11.75°. Therefore, the stoichiometric uptake of

dioxygen by $[Co^{II}(salen)]_P$ can be explained if its molecular structure is similar to that of unprocessed $Ni^{II}(salen)$.

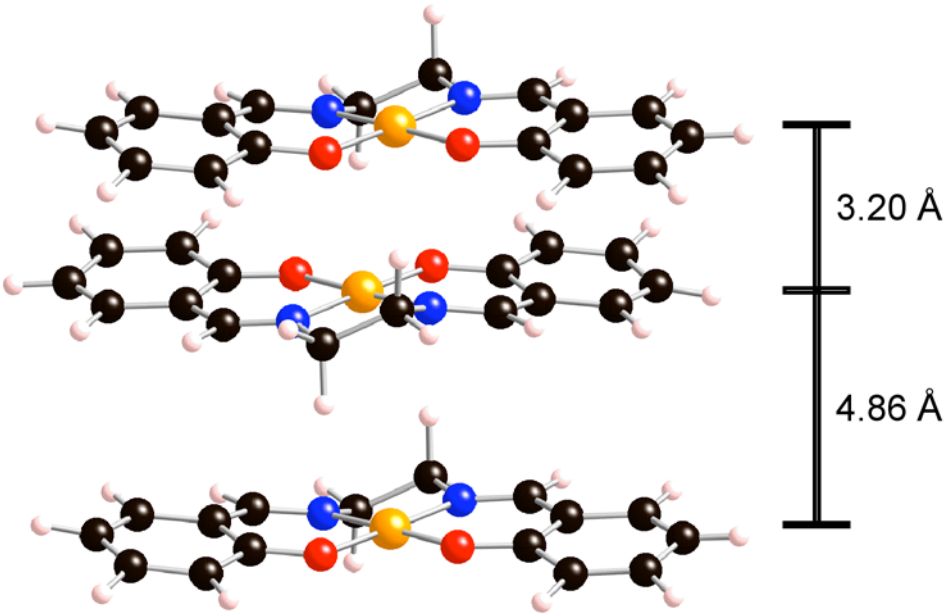

Figure 4-12. Molecular strucuture of unprocessed $Ni^{II}(salen)$. The crystallographic data is available in Reference 16.

Summary and Conclusions

The quantitative analysis and the kinetics of O_2 binding to $[Co^{II}(salen)]_P$ could not be determined using a TEOM because mass flow and pressure fluctuations during the experiments made it difficult to accurately obtain any reliable measurements. Quantitative dioxygen uptake studies utilizing a Rubotherm magnetic suspension balance found that $[Co^{II}(salen)]_P$ stoichiometrically binds dioxygen. Raman spectroscopy helped support the premise that bridging peroxo complexes are formed when dioxygen is taken up by $[Co^{II}(salen)]_P$. Minimal changes in the PXRD data also provide evidence that supports the idea that the arrangement of the metal complexes within $[Co^{II}(salen)]_P$ is similar to the molecular arrangement within unprocessed

Ni^{II}(salen). If the Co^{II}(salen) molecules are stacked in pairs that are approximately 3.2 Å apart, then $[Co^{II}(salen)]_P$ can be reactive towards O_2 with minimal rearrangement of the molecules. As stated previously, this stacking along the c-axis provides additional support for the idea that the nanoparticulate metal complexes have lamellar structures due to its association with the prominent diffraction peak at 11.75°.

The binding of dioxygen to $[Co^{II}(salen)]_P$ illustrates another functional property that the nanoparticles possess that are absent in its molecular precursor. Not only do the nanoparticles bind dioxygen, they reversibly bind O_2, which illustrates the potential for use of these nanoparticles as sorbents for gases. This functional property is unique since four-coordinate Co^{II} complexes are known to bind O_2 poorly. These findings show that the production of nanoparticulate metal complexes via PCA technology affords systems that have distinct structural and functional properties from their molecular precursors.

References

1. (a) Li, G. Q.; Govind, R. *Ind. Eng. Chem. Res.* **1994**, *33*, 755-783. (b) Niederhoffer, E. C.; Timmons, J. H.; Martell, A. E. *Chem. Rev.* **1984**, *84*, 137-203. (c) Martell, A. E. *Acc. Chem. Res.* **1982**, *15*, 155-162.

2. Jones, R. D.; Summerville, D. A.; Basolo, F. *Chem. Rev.* **1979**, *79*, 139-179.

3. Hutson, N. D.; Yang, R. T. *Ind. Eng. Chem. Res.* **2000**, *39*, 2252-2259.

4. Sharma, A. C.; Borovik, A. S. *J. Am. Chem. Soc.* **2000**, *122*, 8946-8955.

5. Cesarotti, E.; Gullotti, M.; Pasini, A.; Ugo, R. *Dalton Trans.* **1977**, 757-763.

6. Johnson, C. A.; Sharma, S.; Subramaniam, B.; Borovik, A. S. *J. Am. Chem. Soc.* **2005**, *127*, 9698-9699.

7. Zhu, W.; van de Graaf, J. M.; van den Broeke, L. J. P.; Kapteijn, F.; Moulijn, J. *Ind. Eng. Chem. Res.* **1998**, *37*, 1934-1942.

8. Johnson, C.; Long, B.; Nguyen, J. G.; Day, V. W.; Borovik, A. S.; Subramaniam, B.; Guzman, J. *J. Phys. Chem. C* **2008**, *112*, 12272-12281.

9. Zhu, W.; Kapteijn, F.; Groen, J. C.; Moulijn, J. A. *Adsorption* **2005**, *11*, 637-641.

10. Xu, X.; Song, C. *Appl. Catal., A* **2006**, *300*, 130-138.

11. (a) Hester, R. E.; Nour, E. M. *J. Raman. Spectrosc.* **1981**, *11*, 49-58. (b) Suzuki, M.; Ishiguro, T.; Kozuka, M.; Nakamoto, K. *Inorg. Chem.* **1981**, *20*, 1993-1996.

12. Brückner, S.; Calligaris, M.; Nardin, G.; Randaccio, L. *Acta Cryst.* **1969**, *B25*, 1671-1674.

13. These measurements were performed by Dr. Chad Johnson and reported in Reference 15.

14. The measurements were performed by Stefan Ottiger and Ronny Pini in Professor Mazzotti's laboratory at ETH Zurich, Institute of Process Engineering. The analysis of the data was performed by Dr. Chad Johnson in Professor Bala Subramaniam's laboratory at the Center for Environmentally Beneficial Catalysis, University of Kansas. The results are reported in Reference 15.

15. Johnson, C. A.; Ottiger, S.; Pini, R.; Gorman, E.; Nguyen, J. G.; Munson, E.; Mazzotti, M.; Borovik, A. S.; Subramaniam, B. *AIChE J.* accepted pending minor revisions.

16. Manfredotti, A. G.; Guastini, C. *Acta Cryst. C* **1983**, *39*, 863-865.

17. Calligaris, M.; Nardin, G.; Randaccio, L. *J. Chem. Soc. D* **1969**, 763-764.

CHAPTER FIVE

DESIGN, SYNTHESIS, AND CHARACTERIZATION OF IMMOBILIZED COBALT(II) COMPLEXES WITHIN SILICA PARTICLES

Introduction

Nitric oxide (NO) has various functions, ranging from its adverse role in the environment to its importance in mammalian biology, as previously discussed (Chapter 1). Because of its diverse importance, there has been strong interest in the development of substances, especially nanomaterials, that can store and subsequently deliver NO. The results in Chapter 3 indicate that Co^{II}(salen) nanoparticles ($[Co^{II}(salen)]_P$) can disproportionate NO into other species, such as N_2, N_2O, and NO_2. While these results indicate that $[Co^{II}(salen)]_P$ is not a useful system for NO delivery, more experiments are needed to completely determine its viability as an NO donor. Another approach for the delivery of NO is to utilize other types of NO storage/releasing nanoparticles.[1-2] Towards that goal, this chapter describes efforts aimed at preparing and immobilizing various metal salen complexes within silica-based nanoparticles that are capable of dispensing NO.

Silica-based materials are ideal systems for adsorption, catalysis, chemical separations, and biotechnological devices because of their chemical and thermal stabilities.[3] Silica-based nanomaterials are also biocompatible and able to be taken up by cells, making them promising materials as drug delivery vehicles.[3a, 4] For

example, Schoenfisch and coworkers immobilized diazeniumdiolates, a NO-releasing drug, onto silica-based nanoparticles (Figure 5-1),[1] which have demonstrated enhanced bactericidal efficacy compared to their larger counterparts.[4a]

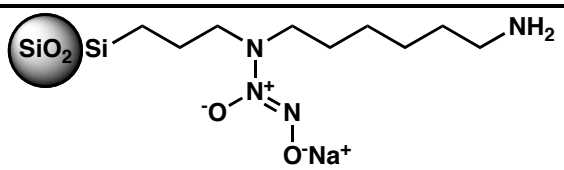

Figure 5-1. A representation of an immobilized diazeniumdiolate onto silica-based nanoparticles.[1]

Even though various metal nitrosyl complexes have been immobilized within porous organic polymers,[5] only a few of these complexes have been entrapped within silica-based materials.[6] To our knowledge, there are no reports of any metal nitrosyl complexes immobilized or entrapped within silica-based nanoparticles. Described herein are synthetic methods for the preparation of modified salen ligands to allow for immobilization within silica nanoparticles and corresponding metal complexes. The chapter also details the synthesis of different metal complexes. Initial immobilization and reactivity studies with NO are also discussed.

Experimental Section

General Methods. All reagents were purchased from commercial sources and used as received, unless otherwise noted. Solvents were purified according to standard procedures.[7] Anhydrous solvents were purchased from Aldrich. Anhydrous toluene, pentane, Et_2O, CH_2Cl_2, and CH_3CN were sparged with UHP argon and dried over columns containing Q-5 and molecular sieves. Potassium hydride (KH) as a 30% dispersion in mineral oil was filtered with a medium porosity glass frit and washed five times each with pentane and Et_2O. Solid KH was dried under vacuum

and stored under an inert atmosphere. Nitric oxide used for the preliminary experiments was chemically pure (99.0%) from Airgas. To trap out NO_x and H_2O impurities, the gas was passed through two U-tubes immersed in isopropanol/dry ice before being exposed to the samples. The compounds *p*-(chloromethyl)phenyltri-isopropoxysilane[8] (**2A**), [*o*-hydroxy, *p*-(*p*-(oxomethylphenyl)triisopropoxysilyl)]-benzaldehyde[8] (**3A**), $Ru(NO)Cl_3$,[5b] 3-*tert*-butyl-5-chloromethyl-2-hydroxy-benzaldehyde[9] (**5**), 5-azidomethyl-3-*tert*-butyl-2-hydroxybenzaldehyde[10] (**6**), *N*-[(3-*tert*-butyl-5-formyl-4-hydroxyphenyl)methyl]-*N'*-(3-triethoxysilylpropyl) urea[10] (**7**), bis[2-hydroxy-4-(4-vinylbenzyloxy)benzaldehyde]ethylenediimine (H_2**9**),[11] and silica particles[1a] were synthesized following literature methods.

Manipulations involving moisture-sensitive materials and syntheses of metal complexes were performed either in Schlenk-type glassware under nitrogen or in a Vacuum Atmospheres, Co. drybox under an argon atmosphere. Elemental analyses were accomplished either at Desert Analytics (Tucson, AZ) or Robertson Microlit Laboratories (Madison, NJ).

***p*-(chloromethyl)phenyltriethoxysilane** (**2B**). This procedure is similar to the synthesis of **2A**.[8] Under an argon atmosphere, a mixture of anhydrous ethanol (8.4 mL), anhydrous triethylamine (20.1 mL), and 80 mL of anhydrous ether was placed in a two-necked flasked equipped with a mechanical stirrer, a condenser, and an additional funnel containing a solution of *p*-(chloromethyl)phenyltrichlorosilane (6.23 g, 0.0240 mol) in ether (50 mL). The two-necked flask was then cooled to 0 °C, and the *p*-(chloromethyl)phenyltrichlorosilane solution was added under nitrogen. After the addition of *p*-(chloromethyl)phenyltrichlorosilane solution, the reaction was stirred at room temperature for at least 2 h. The reaction mixture was then transferred to a dry 500 mL flask, and the solvent was removed under reduced pressure. The

resulting white residue was stirred in pentane (at least 250 mL) under nitrogen. After filtration and concentration of the filtrate, the yellow residual liquid was distilled to afford the product (5.82 g, 84% yield) as a colorless liquid. ^{1}H NMR ($CDCl_3$): δ 1.24-1.27 (t, 9H, J = 7.0 Hz, -OCH_2CH_3), 3.86-3.90 (quart, 6H, J = 7.0 Hz, -OCH_2CH_3), 4.59 (s, 2H, -CH_2Cl), 7.40-7.42 (d, 2H, J = 7.9 Hz, Ar*H*), 7.68-7.70 (d, 2H, J = 8.0 Hz, Ar*H*). ^{13}C NMR ($CDCl_3$): δ 18.29 (-OCH_2CH_3), 46.09 (-CH_2Cl), 58.85 (-OCH_2CH_3), 127.99 (Ar*C*), 131.53 (Ar*C*), 135.30 (Ar*C*), 139.55 (Ar*C*). ^{29}Si NMR ($CDCl_3$): δ -58.45. MS (ESI): *m/z* 326.0 ($M + K^+$).

***p*-(chloromethyl)phenyltrimethoxysilane** (**2C**). This compound was prepared following the same procedure outlined for **2B** with 6.22 g (0.0239 mol) *p*-(chloromethyl)phenyltrichlorosilane, 5.8 mL of methanol, and 20.0 mL of triethylamine to afford the product (4.57 g, 77% yield) as a colorless liquid. ^{1}H NMR ($CDCl_3$): δ 3.63 (s, 9H, -OCH_3), 4.60 (s, 2H, -CH_2Cl), 7.42-7.44 (d, 2H, J = 7.9 Hz, Ar*H*), 7.65-7.97 (d, 2H, J = 8.1 Hz, Ar*H*). ^{13}C NMR ($CDCl_3$): δ 46.19 (-CH_2Cl), 51.05 (-OCH_3), 128.25 (Ar*C*), 130.03 (Ar*C*), 135.41 (Ar*C*), 139.96 (Ar*C*). ^{29}Si NMR ($CDCl_3$): δ -55.07. MS (ESI): *m/z* 269.0 ($M + Na^+$).

[*o*-hydroxy, *p*-(*p*-(oxomethylphenyl)triethoxysilyl)]benzaldehyde (**3B**). This procedure is similar to the synthesis of **3A**.[8] Under an argon atmosphere, a mixture of 2,4-dihydroxybenzaldehyde (1.406 g, 10.18 mmols), dried $NaHCO_3$ (0.975 g, 11.6 mmols), dried KI (0.191 g, 1.15 mmol), 1.2 g of molecular sieves (3 Å), and anhydrous CH_3CN (15 mL) was placed in an 100-mL three-necked flask equipped with a mechanical stirrer, stopcock, condensor with stopper, and an addition funnel containing **2B** (3.832 g, 13.27 mmols) in 5 mL of anhydrous CH_3CN. The flask was heated to 60 °C under nitrogen, the solution of **2B** was added over a course of 1 min, and the reaction mixture was stirred for 24 h. The solvent was removed in

vacuo, and the resulting pink residue was stirred in anhydrous CH_2Cl_2 (~30 mL) under an argon atmosphere. After filtration under argon, the filtrate was concentrated. The residual orange oil was purified using silica flash chromatography with CH_2Cl_2 as the eluent yielding the product as a yellow oil (2.108 g, 51% yield). ^{1}H NMR ($CDCl_3$): δ 1.22-1.25 (t, 9H, J = 7.0 Hz, -OCH$_2$C*H*$_3$), 3.85-3.90 (q, 6H, J = 7.0 Hz, -OC*H*$_2$CH$_3$), 5.01 (s, 2H, -OC*H*$_2$Ph), 6.51-6.52 (d, 1H, J = 2.3 Hz, benzaldehyde Ar*H*), 6.61-6.63 (dd, 1H, J = 2.3 and 8.7 Hz, benzaldehyde Ar*H*), 7.29-7.31 (d, 1H, J = 8.7 Hz, benzaldehyde Ar*H*), 7.39-7.40 (d, 2H, J = 7.9 Hz, phenyl Ar*H*), 7.71-7.73 (d, 2H, J = 8.0 Hz, phenyl Ar*H*), 9.59 (s, 1H, -C*H*O), 11.49 (s, 1H, -O*H*). ^{13}C NMR ($CDCl_3$): δ 18.02 (-OCH$_2$*C*H$_3$), 58.52 (-O*C*H$_2$CH$_3$), 69.87 (-O*C*H$_2$Ph), 101.40 (benzaldehyde Ar*C*), 108.45 (benzaldehyde Ar*C*), 115.17 (benzaldehyde Ar*C*), 126.57 (phenyl Ar*C*), 131.16 (phenyl Ar*C*), 134.95 (phenyl Ar*C*), 135.10 (benzaldehyde Ar*C*), 137.74 (phenyl Ar*C*), 164.16 (benzaldehyde Ar*C*), 165.50 (benzaldehyde Ar*C*), 194.14 (-*C*HO). ^{29}Si NMR ($CDCl_3$): δ -58.31. FT-IR (cm^{-1}, nujol mull): 1657 (C=O), 1641-1628-1577 (C=C), 1080 (Si-O). MS (ESI): *m/z* 413.3 (M + Na$^+$).

Bis[[*o*-hydroxy, *p*-(*p*-(oxomethylphenyl)triisopropoxysilyl)]-benzaldehyde]-ethylenediimine (H_2**1A**). This procedure is a modification of that reported by Corriu and coworkers.[8] Under an argon atmosphere, a solution of ethylenediamine (134 μL, 2.01 mmol) in anhydrous toluene (9 mL) was added dropwise at room temperature to a solution of **3A** (1.74 g, 4.02 mmol) in anhydrous toluene (15 mL) containing 3Å molecular sieves (1 g). The solution became yellow instantly and was refluxed under a nitrogen atmosphere for 45 min. The reaction mixture was then filtered, and the filtrate was concentrated under a reduced atmosphere. The residual oil was dissolved in anhydrous pentane (~100 mL) under a

nitrogen atmosphere. A yellow precipitate formed within 5 min and was allowed to stir for a few more hours. The precipitate was then filtered and washed with anhydrous pentane until the filtrate became colorless. The product was then dried under vacuum to yield 1.57 g of a yellow solid (44% yield). Mp 124–126 ºC. ^{1}H NMR ($CDCl_3$): δ 1.21-1.23 (d, 36H, J = 6.1 Hz, -OCH(CH_3)$_2$), 3.86 (s, 4H, -CH_2CH_2), 4.22-4.32 (sept, 6H, J = 6.1 Hz, -OC*H*(CH_3)$_2$), 5.07 (s, 4H, -OCH_2Ph), 6.45-6.48 (dd, 2H, J = 2.4 and 8.5 Hz, benzaldehyde Ar*H*), 6.506-6.512 (d, 2H, J = 2.4 Hz, benzaldehyde Ar*H*), 7.10-7.12 (d, 2H, J = 8.6 Hz, benzaldehyde Ar*H*), 7.40-7.42 (d, 4H, J = 8.1 Hz, phenyl Ar*H*), 7.69-7.72 (d, 4H, J = 8.1 Hz, phenyl Ar*H*), 8.22 (s, 2H, *H*(Ph)C=N-), 13.68 (s, 2H, -O*H*). ^{13}C NMR ($CDCl_3$): δ 25.60 (-OCH(CH_3)$_2$), 58.78 (-CH_2CH_2), 65.49 (-OCH(CH_3)$_2$), 69.91 (-OCH_2Ph), 102.19 (benzaldehyde Ar*C*), 107.05 (benzaldehyde Ar*C*), 112.60 (benzaldehyde Ar*C*), 126.64 (phenyl Ar*C*), 132.81 (benzaldehyde Ar*C*), 132.87 (phenyl Ar*C*), 135.25 (phenyl Ar*C*), 138.25 (phenyl Ar*C*), 162.69 (benzaldehyde Ar*C*), 164.74 (benzaldehyde Ar*C*), 165.47 (H(Ph)*C*=N-). ^{29}Si NMR ($CDCl_3$): δ -62.08. FT-IR (cm^{-1}, KBr): 1628 (C=N), 1036 (Si-O). HRMS (ESI): Exact mass calcd for $C_{48}H_{68}N_2O_{10}Si_2$ $[M + Na]^+$, 911.4310. Found 911.4297.

Bis[[*o*-hydroxy, *p*-(*p*-(oxomethylphenyl)triethoxysilyl)]-benzaldehyde]-ethylenediimine (H_2**1B**). This compound was prepared following the same procedure outlined for H_2**1A** with 1.02 g (2.61 mmol) **3B** and 87.3 μL (1.31 mmol) ethylenediamine to afford a yellow solid (0.914 g, 44% yield) as the product. Mp 105–108 ºC. ^{1}H NMR ($CDCl_3$): δ 1.20-1.23 (t, 18H, J = 7.0 Hz, -OCH$_2$CH_3), 3.81 (s, 4H, -CH_2CH_2), 3.82-3.86 (q, 12H, J = 7.0 Hz, -OCH_2CH$_3$), 5.03 (s, 4H, -OCH_2Ph), 6.41-6.44 (dd, 2H, J = 2.3 and 8.5 Hz, benzaldehyde Ar*H*), 6.461-6.465 (d, 2H, J = 2.2 Hz, benzaldehyde Ar*H*), 7.06-7.07 (d, 2H, J = 8.6 Hz, benzaldehyde Ar*H*), 7.38-

7.40 (d, 4H, *J* = 7.9 Hz, phenyl Ar*H*), 7.66-7.67 (d, 4H, *J* = 8.0 Hz, phenyl Ar*H*), 8.17 (s, 2H, *H*(Ph)C=N-), 13.55 (s, 2H, -O*H*). ^{13}C NMR ($CDCl_3$): δ 18.42 (-OCH_2CH_3), 58.95 (-OCH_2CH_3), 59.00 (-CH_2CH_2), 70.02 (-OCH_2Ph), 102.32 (benzaldehyde Ar*C*), 107.22 (benzaldehyde Ar*C*), 112.76 (benzaldehyde Ar*C*), 126.93 (phenyl Ar*C*), 130.99 (benzaldehyde Ar*C*), 132.97 (phenyl Ar*C*), 135.33 (phenyl Ar*C*), 138.79 (phenyl Ar*C*), 162.77 (benzaldehyde Ar*C*), 164.80 (benzaldehyde Ar*C*), 165.61 (H(Ph)*C*=N-). FT-IR (cm^{-1}, KBr): 1626 (C=N), 1037 (Si-O). HRMS (ESI): Exact mass calcd for $C_{42}H_{56}N_2O_{10}Si_2$ $[M + H]^+$, 805.3552. Found 805.3548.

Co^{II}1A. Under an argon atmosphere, H_2**1A** (0.70 g, 0.79 mmol) was dissolved in a minimal amount of anhydrous CH_2Cl_2 (~30 mL) in a 250 mL flask. Addition of a solution of $Co(acac)_2$ (0.20 g, 0.79 mmol) in anhydrous CH_2Cl_2 (~30 mL) resulted in the immediate formation of a dark red-orange solution. After 12 h, the solvent was removed in vacuo, and the resulting dark red solid was dissolved in anhydrous pentane (~100 mL). An orange precipitate formed within 5 min and was allowed to stir for a few more hours. The reaction mixture was then filtered and the precipitate was washed with anhydrous pentane until the filtrate became colorless. The product was then dried under vacuum to yield 0.62 g of an orange solid (84% yield). Anal. Calcd (found) for $C_{48}H_{66}CoN_2O_{10}Si_2$: C, 60.93 (59.71); H, 7.03 (6.42); N, 2.96 (2.88); Co, 6.23 (5.63); Si, 5.94 (3.2). FTIR (cm^{-1}, KBr): 1605 (C=N), 1038 (Si-O). UV/vis (CH_2Cl_2): $\lambda_{max/nm}$ (ε, M^{-1} cm^{-1}) = 250 (44900), 335 (13500), 349 (13900), 402 (15100), 480 (2730). X-band EPR (CH_2Cl_2, 4 K): *g* = 3.8, 1.9. HRMS (ESI): Exact mass calcd for $C_{48}H_{66}CoN_2O_{10}Si_2$ $[M + Na]^+$, 968.3486. Found 968.3505.

Co^{II}1B. This compound was prepared following the same procedure outlined for **Co^{II}1A** with 0.721 g (0.896 mmol) H_2**1B** and 0.230 g (0.894 mmol) $Co(acac)_2$ to

afford an orange solid (0.68 g, 88% yield) as the product. FTIR (cm^{-1}, KBr): 1606 (C=N), 1076 (Si-O). UV/vis (CH_2Cl_2): $\lambda_{max/nm}$ (ε, M^{-1} cm^{-1}) = 251 (44900), 334 (13500), 348 (13900), 401 (15100), 480 (2730). X-band EPR (CH_2Cl_2, 77 K): g = 3.8, 1.9. MS (ESI): *m/z* 861.3 ($M + H^+$).

Ru1A(NO)(Cl). This procedure is similar to the one reported by Mitchell-Koch and coworkers[5b] and was done in the presence of minimal light. Under an argon atmosphere, a 9 mL DMF solution of H_2**1A** (0.29g, 0.33 mmols) was treated with solid KH (0.03g, 0.7 mmols). After H_2 evolution was completed (~30 min), $Ru(NO)Cl_3$ (0.08g, 0.3 mmols) was added, and the solution turned into a brown-green color. After the flask was covered with Al foil, the reaction was refluxed under N_2 for 2 h. The solvent was then removed under reduced pressure, and the brown residue was purified using silica gel flash chromatography with a mobile phase of 2% methanol/98% CH_2Cl_2. Fractions containing Ru**1A**(NO)(Cl) were combined and concentrated under reduced pressure to afford 0.12 g of the product as a brown solid (36% yield). ^{1}H NMR ($CDCl_3$): δ 1.22-1.23 (d, 36H, J = 6.1 Hz, -OCH(CH_3)$_2$), 3.89-3.94 (m, 2H, -CH_2CH_2), 4.23-4.32 (m, 8H, -OCH(CH_3)$_2$, -CH_2CH_2), 5.09 (s, 4H, -OCH_2Ph), 6.39-6.42 (dd, 2H, J = 2.4 and 8.8 Hz, benzaldehyde ArH), 6.886-6.892 (d, 2H, J = 2.4 Hz, benzaldehyde ArH), 7.13-7.15 (d, 2H, J = 8.9 Hz, benzaldehyde ArH), 7.41-7.43 (d, 4H, J = 8.0 Hz, phenyl ArH), 7.71-7.73 (d, 4H, J = 8.0 Hz, phenyl ArH), 8.11 (s, 2H, H(Ph)C=N-). ^{13}C NMR ($CDCl_3$): δ 25.75 (-OCH(CH_3)$_2$), 59.44 (-CH_2CH_2), 65.65 (-OCH(CH_3)$_2$), 70.16 (-OCH_2Ph), 105.44 (benzaldehyde ArC), 108.32 (benzaldehyde ArC), 113.99 (benzaldehyde ArC), 126.93 (phenyl ArC), 132.99 (phenyl ArC), 135.47 (phenyl ArC), 137.27 (benzaldehyde ArC), 138.18 (phenyl ArC), 164.36 (benzaldehyde ArC), 166.56 (benzaldehyde ArC), 171.72 (H(Ph)C=N-). FT-IR (cm^{-1}, KBr): 1831 (N-O), 1605 (C=N), 1038 (Si-O). UV/vis

(CH_2Cl_2): $\lambda_{max/nm}$ (ε, M^{-1} cm^{-1}) = 259 (69000), 291 (41000), 367 (16500). MS (ESI): *m/z* 1076.0 ($M + Na^+$).

Ni^{II}1A. H_2**1A** (0.707 g, 0.795 mmols) was dissolved in a minimal amount of anhydrous CH_2Cl_2 (15 mL) in an 100 mL flask. Addition of a solution of $Ni(acac)_2$ (0.205 g, 0.798 mmols) in anhydrous THF (15 mL) resulted in the immediate formation of a dark brown-red solution. The reaction was then refluxed under N_2 for at least 2 h. The solvent was removed under reduced pressure, and the resulting dark red solid was dissolved in anhydrous pentane (~50 mL). An orange precipitate formed within 5 min and was allowed to stir for a few hours. The reaction mixture was then filtered, and the precipitate was washed with anhydrous pentane until the filtrate became colorless. The product was then dried under vacuum to yield 0.76 g of an orange solid (> 98% yield). ^{1}H NMR ($CDCl_3$): δ 1.22-1.23 (d, 36H, J = 6.1 Hz, -OCH(CH_3)$_2$), 3.32 (s, 4H, -CH_2CH_2), 4.23-4.30 (sept, 6H, J = 6.1 Hz, -OCH(CH_3)$_2$), 5.01 (s, 4H, -OCH_2Ph), 6.23-6.25 (d, 2H, J = 8.0 Hz, benzaldehyde Ar*H*), 6.56 (s, 2H, benzaldehyde Ar*H*), 6.87-6.89 (d, 2H, J = 8.5 Hz, benzaldehyde Ar*H*), 7.19 (s, 2H, *H*(Ph)C=N-), 7.40-7.41 (d, 4H, J = 7.6 Hz, phenyl Ar*H*), 7.69-7.70 (d, 4H, J = 7.6 Hz, phenyl Ar*H*). ^{13}C NMR ($CDCl_3$): δ 25.67 (-OCH(CH_3)$_2$), 58.32 (-CH_2CH_2), 65.59 (-OCH(CH_3)$_2$), 69.65 (-OCH_2Ph), 103.50 (benzaldehyde Ar*C*), 106.53 (benzaldehyde Ar*C*), 114.94 (benzaldehyde Ar*C*), 126.73 (phenyl Ar*C*), 132.81 (phenyl Ar*C*), 133.57 (benzaldehyde Ar*C*), 135.30 (phenyl Ar*C*), 138.66 (phenyl Ar*C*), 160.33 (benzaldehyde Ar*C*), 163.39 (benzaldehyde Ar*C*), 166.38 (H(Ph)*C*=N-). ^{29}Si NMR ($CDCl_3$): δ -62.05. FT-IR (cm^{-1}, KBr): 1610 (C=N), 1037 (Si-O). UV/vis (CH_2Cl_2): $\lambda_{max/nm}$ (ε, M^{-1} cm^{-1}) = 268 (58600), 310 (19500), 398 (9580), 436 (4250). MS (ESI): *m/z* 967.7 ($M + Na^+$).

Bis(5-azidomethyl-3-*tert*-butyl-2-hydroxybenzaldehyde)-ethylenediimine

(H_2**8)**. A solution of ethylenediamine (81.2 μL, 1.21 mmols) in anhydrous methanol (9 mL) was added dropwise at room temperature to a solution of **6** (0.564 g, 2.43 mmols) in anhydrous methanol (8 mL). The solution became yellow instantly, a yellow precipitate formed within a couple minutes, and the reaction was allowed to stir for at least 5 hours. The product was collected as a yellow solid after filtration and upon drying, yielding 0.8116 g (68% yield). Mp 78–84 ºC. ^{1}H NMR ($CDCl_3$): δ 1.43 (s, 18H, -C*H*$_3$), 3.97 (s, 4H, -C*H*$_2$C*H*$_2$), 4.26 (s, 4H, -C*H*$_2$N$_3$), 7.061-7.067 (d, 2H, *J* = 2.2 Hz, Ar*H*), 7.239-7.244 (d, 2H, *J* = 2.2 Hz, Ar*H*), 8.40 (s, 2H, *H*(Ph)C=N-), 14.12 (s, 2H, -O*H*). ESI-MS (CH_3OH): *m/z* 491.3 (M+). FT-IR (cm^{-1}, KBr): 2089 (N_3).

Immobilization of Co^{II}1A onto silica particles. This procedure is a modification of that reported by Shin and coworkers.[1a] Under an argon atmosphere, a mixture of tetraethylorthosilicate (TEOS) (0.629 g, 3.02 mmols) and Co^{II}**1A** (0.153 g, 0.162 mmols) was dissolved in anhydrous CH_2Cl_2 (4.0 mL), resulting in a red-orange solution. The mixture was then diluted with anhydrous methanol (30 mL), and the flask was capped with a rubber septum. Ammonia (7 mL, 30 wt % in water) was transferred by cannula to the reaction mixture, and a precipitate formed within 5 min. The reaction was then stirred vigorously for at least 18 h, and the orange precipitate was collected by centrifugation and washed with CH_2Cl_2 until the supernatant was colorless. The resulting orange-tan particles were dried under vacuum overnight to yield 0.28 g of material.

Preliminary NO Experiments. The silica-based particles were placed between two cotton balls inside a 5 cm glass tube. The glass tube was then attached to a piece of Tygon tubing that was connected to the second U-tube. The particles were exposed to flowing N_2 for a few minutes. The flow gas was then switched from

N_2 to NO. Nitric oxide flowed through the sample for at least 30 min, which also resulted in darker particles.

Physical Methods. NMR spectra were recorded on Bruker Avance 400 or 500 MHz spectrometers equipped with a Silicon Graphics workstation. Chemical shifts are reported in ppm relative to residual solvent. Electrospray ionization mass spectra (ESI) were recorded on a Micromass LCT Premier spectrometer operating in W mode (high and low resolution modes). Melting points were obtained with a Laboratory Devices MEL-TEMP apparatus and are uncorrected. Fourier transform infrared spectra (FT-IR) were collected on a Varian Scimitar 800 series FTIR instrument with values reported in wavenumbers. Electronic spectra were collected on a Cary 50 spectrophotometer using 1.00 mm quartz cuvettes. Perpendicular-mode X-band EPR spectra were collected using a Bruker EMX spectrometer equipped with an ER041XG microwave bridge. A quartz liquid nitrogen finger Dewar (Wilmad Glass) was used to record spectra at 77K, and low-temperature (4 K) spectra were obtained using an Oxford Instrument liquid He quartz cryostat. Spectra for EPR active samples were collected using the following spectrometer settings: attenuation = 15 dB, microwave power = 6.300 mW, frequency = 9.26 GHz, sweep width = 5000 G, modulation amplitude = 10.02 G, gain = 1.00×10^3, conversion time = 81.920 ms, time constant = 655.36 ms, and resolution = 1024 points.

Scanning electron micrographs were acquired on a Schottky thermal field emission FEI/Philips XL-30FEG operating at an accelerating voltage of 10.0 kV. SEM samples were prepared by sprinkling the sub-micron particles directly onto a conductive carbon tab (Ted Pella, Inc. Part # 16084-1) attached to a 12.7 mm diameter aluminum specimen mount (Ted Pella, Inc. Part # 16111) and pressed down. The sample was then sputter-coated with a 3 nm thick Au-Pd alloy coat by using a

Polaron SC7600 operating at 53 mTorr and 5 mA. Transmission electron micrographs were acquired using an FEI/Philips CM-20 operating at 200 kV. The sub-micron particles were dispersed in EtOH and sonicated for approximately 5 min. It was then deposited on an ultrathin holey carbon film on a 400 mesh copper grid (Ted Pella, Inc. Part # 01824) and allowed to dry prior to imaging. The transmission electron microscope was also equipped with an energy-dispersive spectrometer (EDAX/4pi) system.

Surface area analysis was collected on an Autosorb-1 instrument (Quantachrome Instruments). Approximately 200 mg of the sample was transferred to a preweighed sample tube and degassed at 100 °C for approximately 24 h. The sample tube was re-weighed to obtain a consistent mass for the sample. BET surface area (m^2/g) measurements were collected at 77 K by dinitrogen using a volumetric technique.

Results and Discussion

Design Considerations and Ligand Syntheses. In order to covalently immobilize the salen ligand within silica nanoparticles, the salen ligand needs to be modified with alkoxysilyl functional groups. Ayala and coworkers have effectively immobilized chiral salen palladium and nickel complexes on ordered mesoporous silica supports.[10] They have accomplished this by covalently binding *N*-[(3-*tert*-butyl-5-formyl-4-hydroxyphenyl)methyl]-*N'*-(3-triethoxysilylpropyl) urea (**7**) to the silica support, and then the chiral Schiff base is synthesized within the support.

Since Ayala and coworkers were able to synthesize the chiral Schiff base ligand within silica supports, it was thought that the same aldehyde, **7**, could be used to synthesize the alkoxysilyl-modified salen ligand (Scheme 5-1). Aldehyde **7** was synthesized because compound **5** could be produced cleanly in high yields. Attempts

to synthesize the Schiff base from aldehyde **7** afforded a yellow solid when it was synthesized in anhydrous THF. However, problems arose during the characterization of the Schiff base ligand: it appeared to polymerize in anhydrous $CDCl_3$ when attempts were made to characterize it by NMR spectroscopy. The polymerization most likely occurred because the ligand was unstable due to the presence of water that could not be removed.

Scheme 5-1 [a]

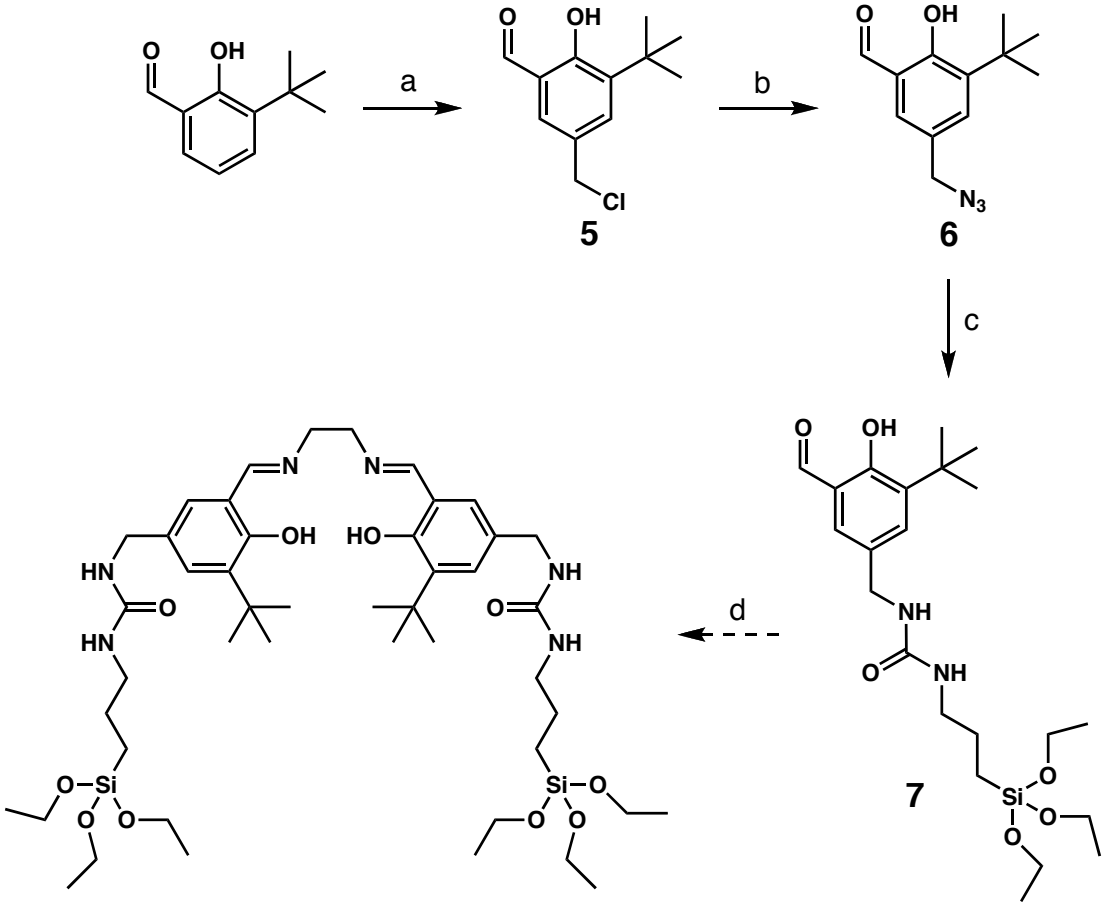

[a] Conditions: (a) n-BuNBr, conc. HCl, 40°C, 3 d, 94%; (b) NaN_3, DMF, rt, 6-10 h, 91%; (c) H_2, Pd/C, EtOAc, rt, 24 h, $OCN(CH_2)_3Si(OEt)_3$, 32%; (d) $H_2NCH_2CH_2NH_2$ (0.5 eq), anhy. THF, N_2, rt, 6 h.

Since it was difficult to dry aldehyde **7**, a different approach was taken to synthesize an alkoxy-modified salen (Scheme 5-2). The first step in this approach was to use compound **6** and synthesize the Schiff base ligand, H_2**8**, which was easily done and produced reasonable yields. It was anticipated that H_2**8** could be converted to an alkoxy-modified salen after the azide was reduced since ureayl compounds could readily be formed from the coupling of an amine with an isocyanate functional group. Two different approaches were taken to reduce the azides in the presence of 3-triethoxysilylpropylisocyanate. Unfortunately, the reaction never went to completion, and isolation of the alkoxy-modified Schiff base was not successful.

Scheme 5-2 [a]

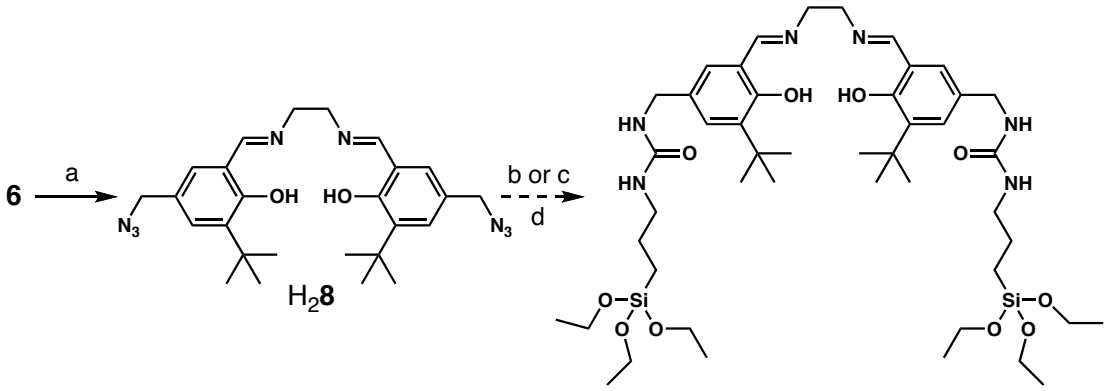

[a] Conditions: (a) $H_2NCH_2CH_2NH_2$ (0.5 eq), anhy. MeOH, N_2, rt, 4h; (b) PPh_3 (2.1 eq), THF/H_2O, rt, 2 h; (c) H_2, Pd/C, EtOAc, rt, 2 h; (d) $OCN(CH_2)_3Si(OEt)_3$, THF or EtOAc, rt, 24 h.

The previous approaches of synthesizing an alkoxy-modified salen ligand had several problems, including moisture issues. Borovik and coworkers had successfully immobilized a number of different metal salen complexes within an porous organic polymer by utilizing a styryloxy-modified salen ligand (H_2**9**).[5, 11] Since H_2**9** could easily be dried, it could be converted to an alkoxy-modified salen ligand through hydrosilylation reactions (Scheme 5-3). Hydrogen hexachloroplatinate (H_2PtCl_6) was

initially used as a catalyst because Lee and coworkers successfully used it in their attempts to immobilize D-glucose within zeolite crystals.[12] However, the catalyst was ineffective in CH_2Cl_2 as it turned black immediately upon contact with the reaction mixture. Platinum(0)-1,3-divinyl-1,1,3,3-tetramethyldisiloxane complex (Pt(0)) was also used as a catalyst because Zhao and coworkers successfully utilized it towards the production of photodeformable spherical hybrid nanoparticles,[13] but the desired ligand still did not form.

Scheme 5-3 [a]

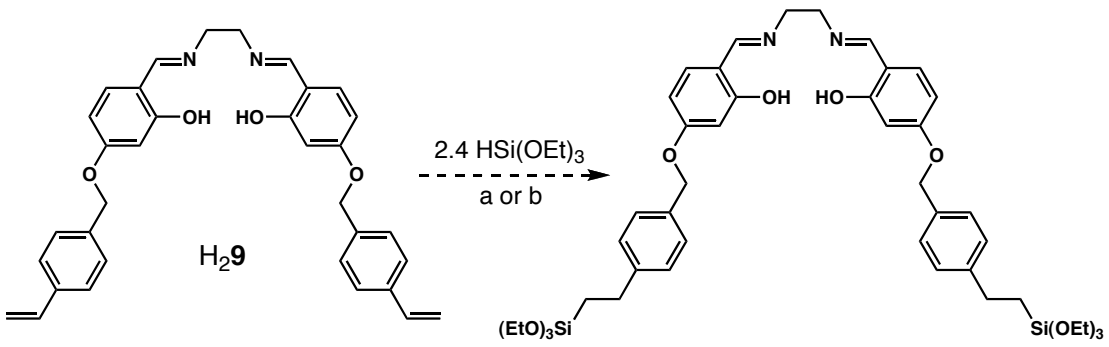

[a] Conditions: (a) H_2PtCl_6, CH_2Cl_2, 80°C, N_2; (b) Pt(0), THF, 50°C, N_2

In the approach utilized in Scheme 5-1, many of the synthetic steps cannot be performed under anhydrous conditions. This is an issue because silyl functional groups are unstable under acidic and basic conditions in the presence of a small amount of water. Corriu and coworkers have synthesized silica-based hybrid materials containing metal Schiff base complexes for dioxygen adsorption.[8] Their synthetic procedures are advantageous over the previous methods because they occur in anhydrous solvents, use a shorter preparative route, and can vary the alkoxysilyl group for different reactivities. It was reasoned that small modifications in the

experimental protocol would produce the desired ligand, alkoxysilyl-modified salen ligand (Scheme 5-4), using ethylenediamine ($NH_2CH_2CH_2NH_2$) as the diamine.

Scheme 5-4 [a]

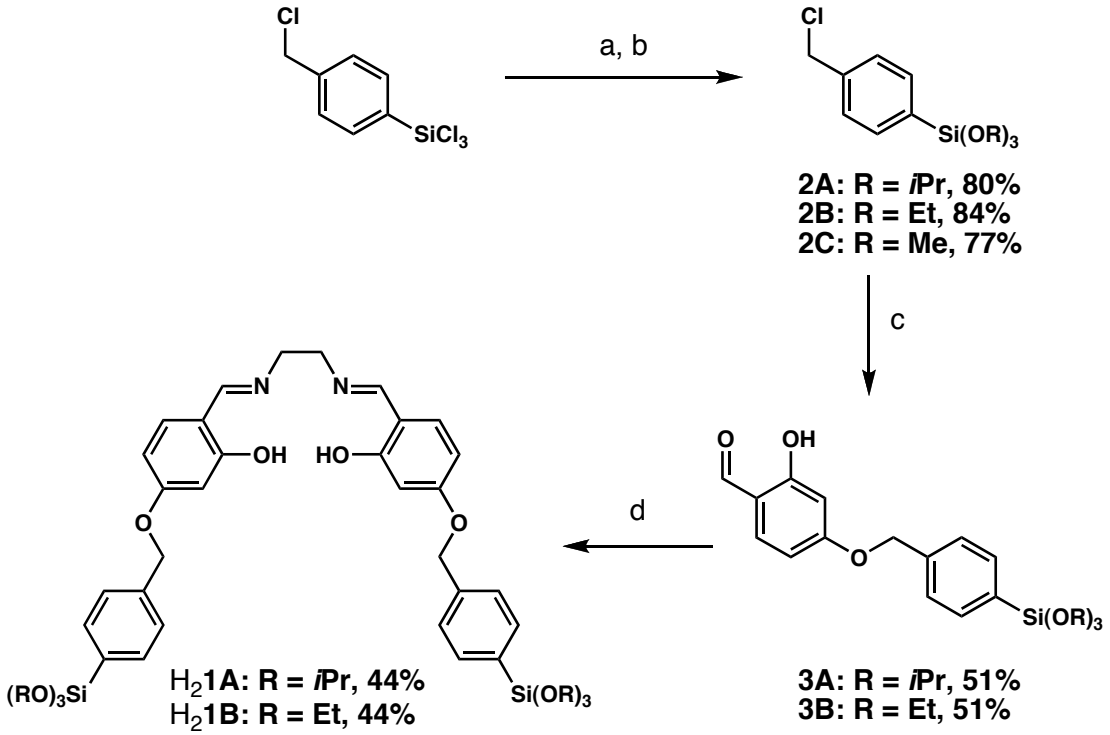

[a] Conditions: (a) 6 **R**OH (**R** = *i*Pr, Et, Me), 6 Et_3N, Et_2O, N_2, 0°C; (b) rt, N_2, 2 h; (c) 2,4-dihydroxybenzaldehyde (0.7 eq), $NaHCO_3$ (0.9 eq), KI (0.1 eq), CH_3CN, N_2, 60°C, 24 h; (d) $NH_2CH_2CH_2NH_2$ (0.5 eq), toluene, N_2, ↓↑, 45 min

The synthetic procedure for the synthesis of **2A** provides a procedure where the R-groups (alkoxy groups) can be varied easily. This variability is important because different size alkoxy groups provide different reactivities, which is an important factor during nanoparticulate formation. Generally, smaller R-groups are more reactive and will polymerize easily. This is apparent with compound **2C** because it polymerizes over time, even when it is stored under an inert atmosphere.

Compounds **2A** and **2B** are converted to their respective aldehydes, **3A** and **3B**, in decent yields. Unfortunately, the converted aldehyde from compound **2C** cannot be isolated, which is likely due to its instability under the reaction conditions. Despite using 3Å molecular sieves for the adsorption of the small amount of water present in the solvent and reaction, the methoxy groups were still too reactive. Fortunately, both compounds **3A** and **3B** readily react with ethylenediamine to form the alkoxysilyl-modified Schiff base ligands, H_2**1A** and H_2**1B**, respectively. The yields are relatively low because some polymerization occurred during the reactions, even though the reactions were done in the presence of 3Å molecular sieves. Both ligands were characterized by ^{1}H, ^{13}C, and ^{29}Si (only for H_2**1A**) spectroscopy, FTIR spectroscopy, and high-resolution mass spectrometry.

Preparation and Characterization of Co^{II}1A, Co^{II}1B, and Ni^{II}1A. The reaction conditions for the traditional methods in the preparation of Co^{II}(salen) complexes are not appropriate for H_2**1A** and H_2**1B** because they are too acidic and contain too much water, which are perfect polymerization conditions. In order to form the metal complexes, a different metal salt needed to be used. Thus, both nickel(II) acetylacetonate ($Ni(acac)_2$) and cobalt(II) acetylacetonate ($Co(acac)_2$) were used to form the desired complexes.

Since the nickel(II) alkoxysilyl salen complex (Ni^{II}**1A**) can be characterized using NMR spectroscopy, it was initially synthesized to establish the synthetic procedures needed for the formation of the metal complexes. The nickel complex was prepared by dissolving H_2**1A** in CH_2Cl_2, which formed a pale yellow solution.

The addition of a THF solution of $Ni(acac)_2$ produced a red-brown solution, which was refluxed for 2 h (Scheme 5-5). A red oil containing both Ni^{II}**1A** and acetylacetone was obtained after the solvent was removed under reduced pressure. A red precipitate formed upon addition of anhydrous pentane to the red oil, and Ni^{II}**1A** was isolated in greater than 98% yield after filtration.

The complex was structurally characterized by ^{1}H, ^{13}C, and ^{29}Si NMR spectroscopy, FTIR and absorbance spectroscopy, and mass spectrometry. The synthesis of Ni^{II}**1A** showed that acetylacetonate complexes could be used to form alkoxysilyl-modified metal complexes. However, the desired complex could only be isolated cleanly as long as the filtration process occurred quickly. If the filtration occurred slowly, it was difficult to separate acetylacetone.

Preparation of the cobalt(II) alkoxysilyl salen complexes (Co^{II}**1A** and Co^{II}**1B**) is outlined in Scheme 5-5. Since both cobalt complexes are air sensitive (see Chapter 4 for more details), the synthetic procedure differs slightly from that of the Ni(II) preparation. The reaction takes place under an inert atmosphere and is allowed to react for a longer time period because it could not be refluxed. The complexes are obtained as orange solids in good yields. If the complexes are contaminated with acetylacetone, the product is noticeably darker.

Scheme 5-5 [a]

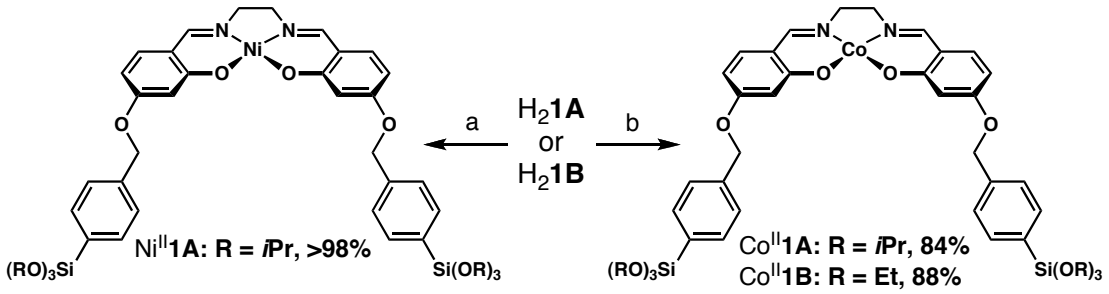

[a] Conditions: (a) $Ni(acac)_2$, THF/CH_2Cl_2, N_2, ↓↑, 2 h; (b) $Co(acac)_2$, CH_2Cl_2, Ar, rt, 12 h

Both Co^{II}**1A** and Co^{II}**1B** were characterized by absorbance, EPR, and FTIR spectroscopies, mass spectrometry, and elemental analysis. The absorbance spectra of the complexes were nearly identical to those reported for Co^{II}(salen).[14] The low-spin Co^{II} complexes were EPR active with signals originating from the ±½ doublet ground state. A representative X-band EPR spectrum of Co^{II}**1A** in CH_2Cl_2 measured at 4 K is nearly identical to those reported for Co^{II}(salen) immobilized within a porous organic polymer (Figure 5-2).[5b] This spectrum is consistent with a square-planar coordination geometry about the Co^{II} ions.

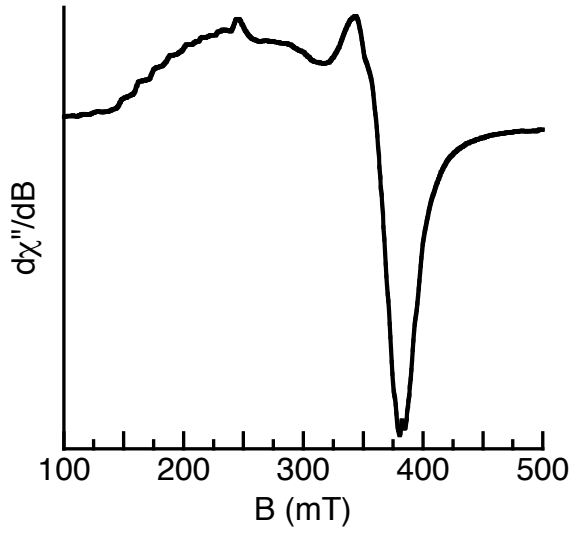

Figure 5-2. X-band EPR spectrum Co^{II}**1A** measured at 4 K.

Preparation and Characterization of Ru1A(NO)(Cl). In order to synthesize a metal nitrosyl complex that can photolytically release NO on demand, a new ruthenium nitrosyl complex was synthesized according to literature procedures used in the synthesis of similar complexes (Scheme 5-6). The conditions are generally harsh for silyl functional groups, but alkoxysilyl ruthenium nitrosyl complex (Ru**1A**(NO)(Cl)) was isolated as a brown solid. Unfortunately, the harsh reaction conditions result in a relatively low yield of 36%.

Scheme 5-6

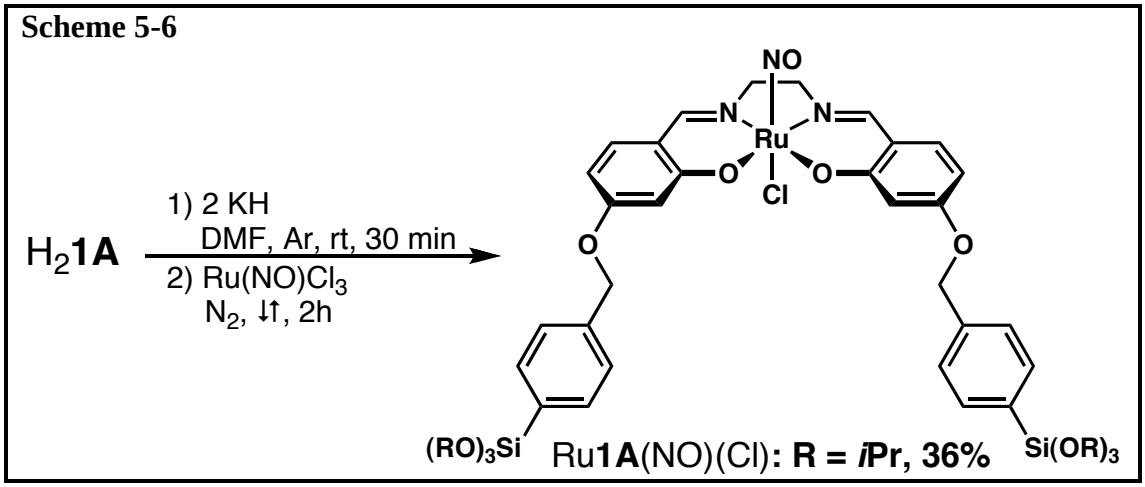

Complex Ru**1A**(NO)(Cl) was structurally characterized by ^{1}H and ^{13}C NMR spectroscopy, FTIR and absorbance spectroscopy, and mass spectrometry. ^{1}H and ^{13}C NMR spectroscopy provided evidence that the isopropoxysilyl functional groups remain intact during synthesis. The N—O stretching frequency at 1831 cm^{-1} for Ru**1A**(NO)(Cl) (Figure 5-3 solid blue line) is similar to other ruthenium nitrosyl complexes.[5b, 15] The optical spectrum for the complex also displays a band at λ_{max} 367 nm (CH_2Cl_2, ε = 1.65 x 10^4 M^{-1} cm^{-1}), which is also found in similar ruthenium nitrosyl complexes (Figure 5-4a).[5b]

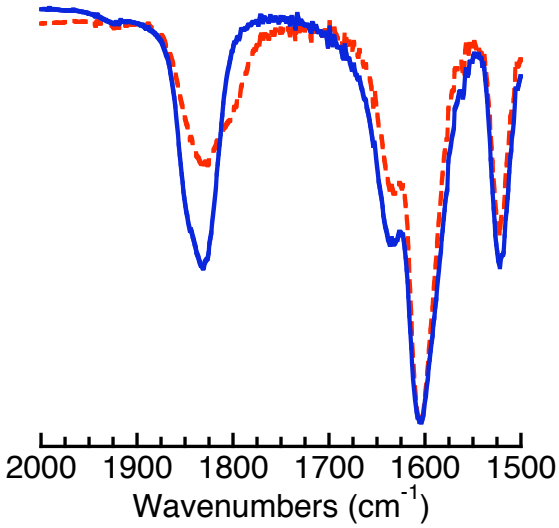

Figure 5-3. FTIR spectra for Ru**1A**(NO)(Cl) before (—) and after (- -) photolysis.

Additional evidence for the synthesis of Ru**1A**(NO)(Cl) comes from preliminary photolysis studies. When a CH_2Cl_2 solution of Ru**1A**(NO)(Cl) was irradiated with 370 nm light, a new species is formed with an absorbance band at 393 nm (CH_2Cl_2, ε = 2.1 x 10^4 M^{-1} cm^{-1}) (Figure 5-4b). In addition, the observed broad band centered at 607 nm (CH_2Cl_2, ε = 4.5 x 10^3 M^{-1} cm^{-1}) is assigned to a ligand to

metal charge transfer band characteristic of Ru(III) salen complexes.[15a] The release of NO is also observed in the FTIR spectrum with a less intense band at 1831 cm^{-1} (Figure 5-3, dashed red line). These results are consistent with what has been reported for other ruthenium nitrosyl complexes.[5b, 15a]

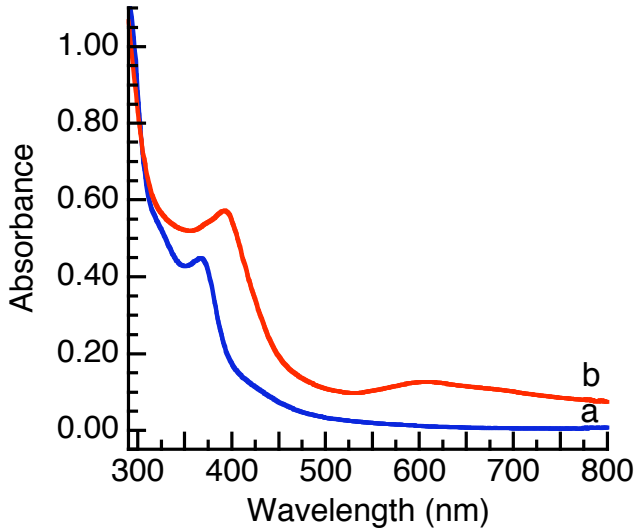

Figure 5-4. Absorbance spectra for Ru**1A**(NO)(Cl) (a) before (—) and (b) after (—) photolysis.

Preparation of Silica-based Materials. The silica-based materials were prepared by the copolymerization of the metal complex monomers with the crosslinker, tetraethylorthosilicate (TEOS), via a sol-gel polymerization process. The sol-gel process is described as a two-step inorganic polymerization (Scheme 5-7), which is initiated by an acid or base-catalyzed hydrolysis of an alkoxide to form an alcohol and water.[16] Polymer-like gels with relatively small pores are formed when the hydrolysis step is favored and condensation is the rate-determining step. Large porous colloidal particles with diameters ranging from 1-1000 nm are synthesized

when high condensation rates are favored, which is preferred for the formation of silica nanoparticles.

Scheme 5-7 [a]

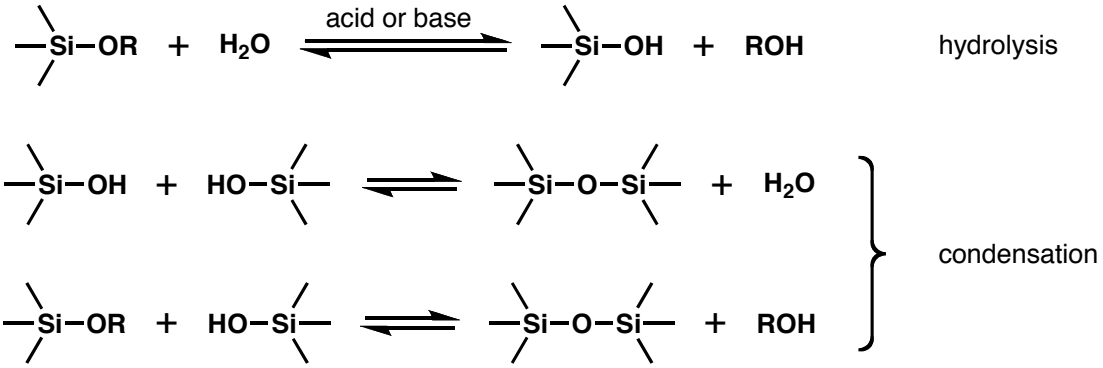

[a] Adapted from ref 15.

The procedure for the synthesis of silica-based materials was modified from a method developed by Shin and coworkers (Scheme 5-8).[1a] When Co^{II}**1A** was initially copolymerized with TEOS, it was dissolved in methanol. However, a small amount of dioxygen was present in the flask, turning the solution green, which is evidence that Co^{II}**1A** was binding O_2. Colloidal particles started forming within ten minutes after the addition of strong ammonia solution (30% NH_3 in H_2O), and the solution began turning orange shortly afterwards. Unfortunately, this process resulted in amorphous colloidal particles (Figure 5-5a).

Scheme 5-8 [a]

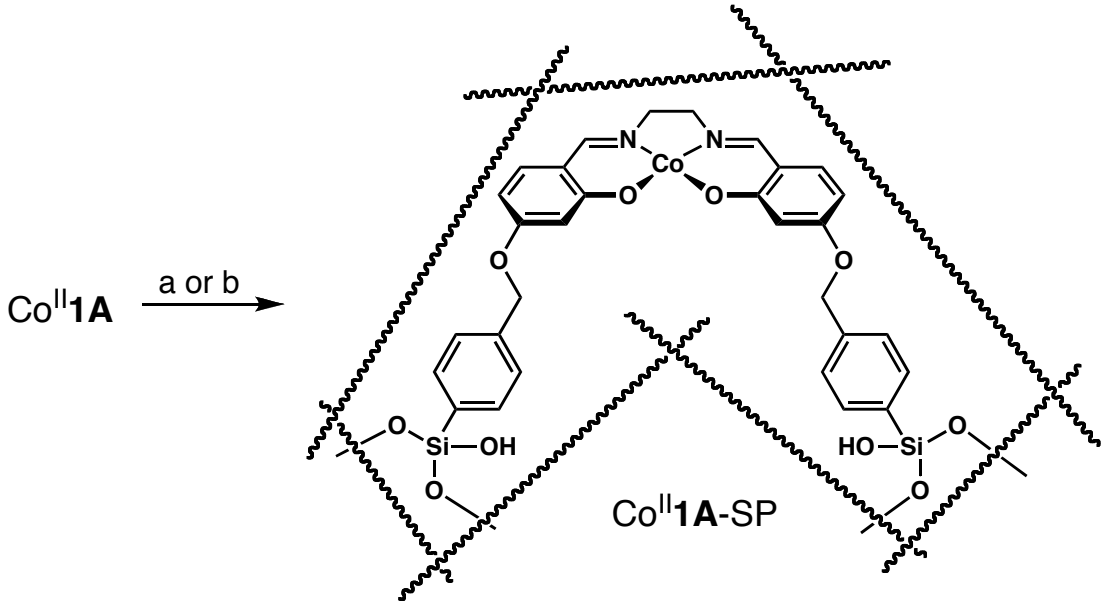

[a] Conditions: (a) TEOS, NH_3(30%)/H_2O, MeOH, N_2, rt; (b) TEOS, NH_3(30%)/H_2O, MeOH/CH_2Cl_2, Ar, rt.

In order to prevent dioxygen binding, Co^{II}**1A** was dissolved in methanol under an inert atmosphere. However, the solubility of Co^{II}**1A** in methanol was lower without the presence of dioxygen, so a small amount of CH_2Cl_2 was added to keep the solution fairly concentrated. Colloidal particles started forming within five minutes after the addition of strong ammonia solution. The particles were then washed with CH_2Cl_2, which resulted in spherical orange-tan particles (Co^{II}**1A**-SP) (Figure 5-5b). It is unknown why the presence of dioxygen prevented the formation of discrete silica-based spheres because silica particles could be synthesized in the presence of dioxygen (Figure C-1). The average diameters of these cobalt containing silica particles were 650 nm, too large to be considered nanoparticles.

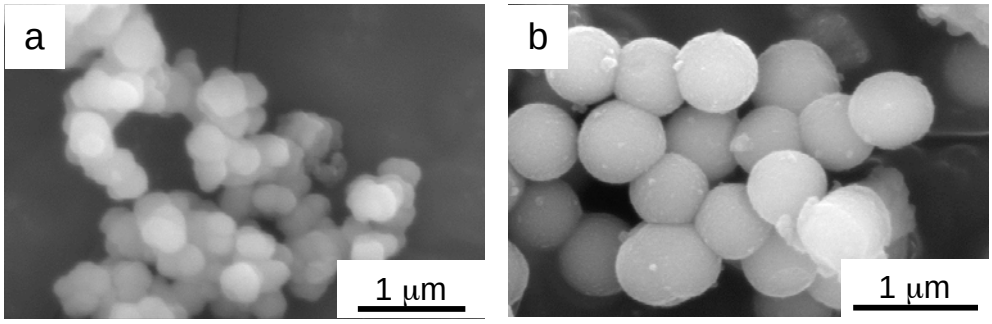

Figure 5-5. SEM micrographs of the particles formed during the copolymerization of Co^{II}**1A** and TEOS synthesized in (a) the open atmosphere and (b) an inert atmosphere.

Solubility issues prevented the copolymerization of Ru**1A**(NO)(Cl) with TEOS. Unfortunately, Ru**1A**(NO)(Cl) was approximately nine times less soluble in CH_2Cl_2 than Co^{II}**1A**. When Ru**1A**(NO)(Cl) was immobilized within silica particles, there was no evidence, via FTIR spectroscopy, that the ruthenium nitrosyl complex was copolymerized with TEOS. Limited solubility in methanol prevented the copolymerization of Ni^{II}**1A** with TEOS. When ammonia (30 wt % in water) was added to the Ni^{II}**1A** solution, a precipitate formed immediately. After the particles were washed with CH_2Cl_2, the supernatant became red, leaving a light tan precipitate. Energy dispersion spectroscopy showed no evidence that the nickel complex was copolymerized with TEOS.

Characterization of Co^{II}1A-SP. The Co^{II}**1A**-immobilized silica particles (Co^{II}**1A**-SP) were approximately 100 nm larger than the silica particles that were synthesized without the metal complexes. Shin and coworkers found the opposite trend to be true with their aminomethoxysilane monomers.[1a] One of the contributing factors involves the alkoxysilyl groups on the monomers used in each case. The NO-

releasing silica particles copolymerized TEOS with various aminomethoxysilane monomers. The methoxysilyl functional groups are smaller and more reactive than the isopropoxysilyl functional groups on Co^{II}**1A**, which allows for quicker condensation and formation of smaller particles.

Due to solubility limitations, only a small amount of Co^{II}**1A** is used during the formation of the Co^{II}**1A**-SP. Thus, there was a concern of whether cobalt was present within the particles. Energy dispersion spectroscopy (EDS) provides evidence that cobalt is present within the particles (Figure 5-6a). The copper peaks are due to the TEM grids. Elemental analyses on the silica particles also provide support for the presence of cobalt within Co^{II}**1A**-SP (Table 5-1). An increase in carbon, nitrogen, and hydrogen provides additional evidence for the immobilization of Co^{II}**1A** within the silica particles.

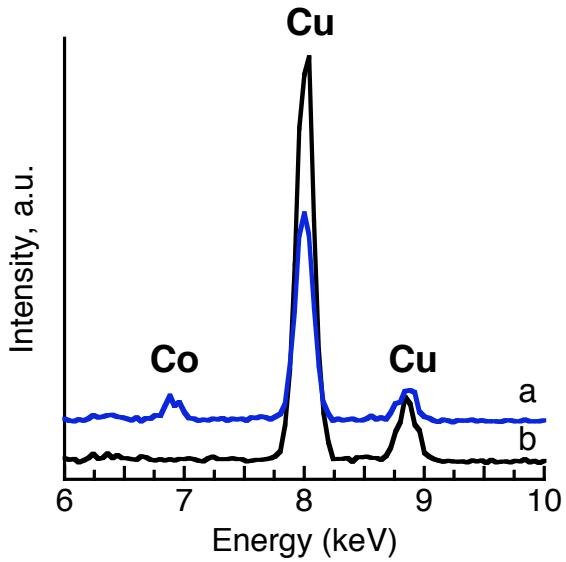

Figure 5-6. Energy dispersion spectrograph of (a) Co^{II}**1A**-SP and (b) silica particles.

Table 5-1. Results from Elemental Analyses.

	% Co	%C	%H	%N	%Si
Co^{II}**1A**-SP	1.82	11.09	1.74	2.25	24.31
Silica Particles	<0.01	0.46	0.77	0.15	30.28

The Co^{II}**1A**-SP particles were also analyzed by EPR spectroscopy. The X-band EPR spectrum of the Co^{II}**1A**-SP measured at 4 K signifies that the cobalt center has changed and has *g*-values of 5.36, 2.00, and 1.85 (Figure 5-7). The EPR spectrum indicates that there is probably more than one species present in the sample. The signal centered at $g = 2.00$ is representative of a dioxygen-bound cobalt complex (Figure 5-7, inset); comparable spectra have been reported for other dioxygen adducts of molecular Co(II) complexes.[11, 17] This finding is not surprising because the particles undergo a slight color change during the CH_2Cl_2 washes. However, more studies need to be accomplished to determine the origin of the signals centered at $g =$ 5.36 and 1.85.

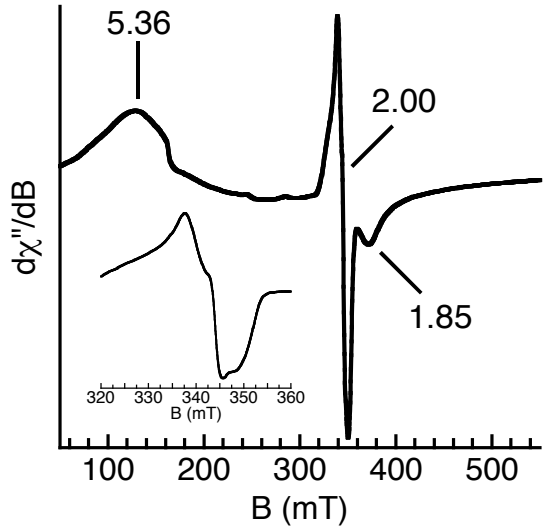

Figure 5-7. X-band EPR spectrum of Co^{II}**1A**-SP at 4 K. Inset: Higher resolution scan of the $g = 2$ region showing a signal with *g*-values of 2.04, 2.00, 1.98.

Surface area analysis of Co^{II}**1A**-SP and the silica particles without metal complexes (SP) show that both sets of particles are not porous with surface areas of 1.88 and 2.59 m^2/g and pore volumes of 0.086 and 0.030 mL/g (at P/P_0 = 1.00), respectively. These surface areas are slightly smaller than those found by Shin and coworkers.[1a] The smaller surface area for Co^{II}**1A**-SP could be due to the immobilization of Co^{II}**1A**, which is larger and less reactive than TEOS. There is also a possibility that Co^{II}**1A** is immobilized only on the surface of the silica particles, but more experiments need to be done in order to confirm the location of the metal complexes.

Preliminary Reactivity Studies of Co^{II}1A-SP with NO. Initial NO reactivity studies were performed on the Co^{II}**1A**-SP. When Co^{II}**1A**-SP was exposed to flowing NO, the particles turned noticeably darker. These particles appear to disproportionate NO into other nitrogen species, such as N_2O and N_2,[18] which is supported by FTIR spectroscopy (Figure 5-8). Two new bands are present in samples treated with flowing NO that are assigned to these nitrogen-based products (Figure 5-8b): N_2O (2220 cm^{-1})[19] and N_2 (2176 cm^{-1}).[20] The features do not disappear when the NO-exposed particles are heated under vacuum for about 24 hours (Figure 5-8c).

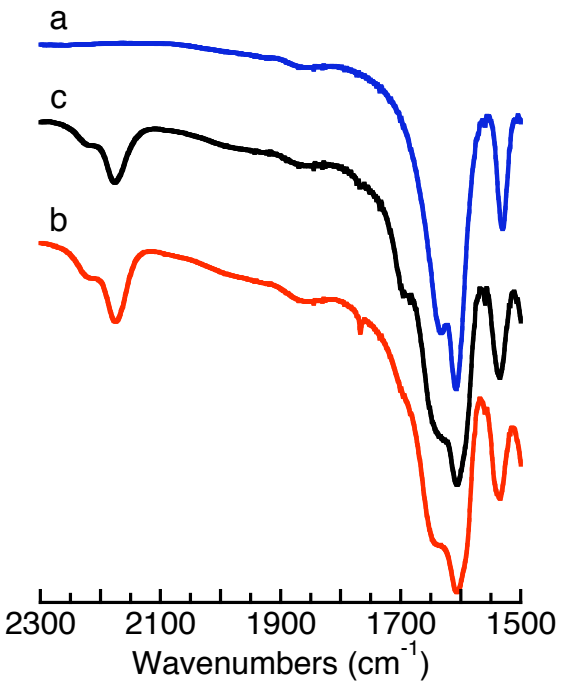

Figure 5-8. FTIR spectra (KBr pellets) of (a) Co^{II}**1A**-SP (—), (b) Co^{II}**1A**-SP + NO (—), and (c) NO-exposed Co^{II}**1A**-SP placed under vacuum at 120 °C for approximately 24 h (—).

The overall results are not particularly surprising because Co^{II}**1A**-SP is porous enough for NO to flow freely. When compared to the $[Co^{II}(salen)]_P$ system, there are a couple of differences in the disproportionation of NO. The band at 2216 cm^{-1} is not as intense, which means less N_2O is produced during the disproportionation process. Additional experiments are required to understand why less N_2O is produced. Another difference involves the stability of the disproportionation products when the NO-exposed samples are heated under vacuum. The new FTIR bands probably do not disappear while the samples are heated under vacuum because silica-based materials are chemically and thermally stable. Thus, higher temperatures are probably required to remove the NO disproportionation products, assuming that the disproportionation products can be removed.

Summary and Conclusions

Two new alkoxysilyl-modified salen ligands have been prepared. The ligands were developed to immobilize various metal complexes within silica particles. The synthesis of Co^{II}**1A** and Ni^{II}**1A** provide evidence that metal complexes can be readily synthesized using acetylacetonate salts. It was also found that H_2**1A** is stable enough to withstand the rigorous reaction conditions for the synthesis of a ruthenium nitrosyl complex. Overall, these metal complexes are advantageous because they have two points of immobilization in which they can be covalently linked within a silica matrix.

Initial immobilization studies have incorporated cobalt complexes within sub-micron silica-based spherical particles. These cobalt containing silica particles are larger than pure silica particles while having smaller average pore diameters. Preliminary reactivity studies with NO show that the particles disproportionate NO at room temperature, which is supported by vibrational spectroscopy. The Co^{II}**1A**-SP particles do not produce as much N_2O as the $[Co^{II}(salen)]_P$ system, and the disproportionation products stay bound even after the NO-exposed samples are heated under vacuum for approximately 24 hours.

In conclusion, the metal complexes can benefit from having smaller alkoxysilyl functional groups as their points of immobilization. The larger isopropoxysilyl functional groups have led to solubility issues that have prevented the immobilization of both Ru**1A**(NO)(Cl) and Ni^{II}**1A** within silica particles. The larger alkoxysilyl groups have also led to the production of larger than anticipated cobalt

containing particles. Nonetheless, the preparative routes described in this chapter provide a good foundation for the future production of silica-based nanoparticles with immobilized metal complexes.

References

1. (a) Shin, J. H.; Metzger, S. K.; Schoenfisch, M. H. *J. Am. Chem. Soc.* **2007**, *129*, 4612-4619. (b) Shin, J. H.; Schoenfisch, M. H. *Chem. Mater.* **2008**, *20*, 239-249.

2. (a) Neuman, D.; Ostrowski, A. D.; Mikhailovsky, A. A.; Absalonson, R. O.; Strouse, G. F.; Ford, P. C. *J. Am. Chem. Soc.* **2008**, *130*, 168-175. (b) Neuman, D.; Ostrowski, A. D.; Absalonson, R. O.; Strouse, G. F.; Ford, P. C. *J. Am. Chem. Soc.* **2007**, *129*, 4146-4147.

3. (a) Trewyn, B. G.; Slowing, I. I.; Giri, S.; Chen, H.-T.; Lin, V. S. Y. *Acc. Chem. Res.* **2007**, *40*, 846-853. (b) Khiterer, M.; Shea, K. J. *Nano Lett.* **2007**, *7*, 2684-2687.

4. For examples see: (a) Hetrick, E. M.; Shin, J. H.; Stasko, N. A.; Johnson, C. B.; Wespe, D. A.; Holmuhamedov, E.; Schoenfisch, M. H. *ACS Nano* **2008**, *2*, 235-246. (b) Gemeinhart, R. A.; Luo, D.; Saltzman, W. M. *Biotechnol. Prog.* **2005**, *21*, 532-537.

5. (a) Mitchell-Koch, J. T.; Padden, K. M.; Borovik, A. S. *J. Polym. Sci., Part A: Polym. Chem.* **2006**, *44*, 2282-2292. (b) Mitchell-Koch, J. T.; Reed, T. M.; Borovik, A. S. *Angew. Chem., Int. Ed.* **2004**, *43*, 2806-2809. (c) Padden, K. M.; Krebs, J. F.; MacBeth, C. E.; Scarrow, R. C.; Borovik, A. S. *J. Am. Chem. Soc.* **2001**, *123*, 1072-1079. (d) Halpenny, G. M.; Olmstead, M. M.; Mascharak, P. K. *Inorg. Chem.* **2007**, *46*, 6601-6606.

6. (a) Eroy-Reveles, A. A.; Leung, Y.; Beavers, C. M.; Olmstead, M. M.; Mascharak, P. K. *J. Am. Chem. Soc.* **2008**, *130*, 4447-4458. (b) Eroy-Reveles, A. A.; Leung, Y.; Mascharak, P. K. *J. Am. Chem. Soc.* **2006**, *128*, 7166-7167. (c) Bordini, J.; Ford, P. C.; Tfouni, E. *Chem. Commun.* **2005**, 4169-4171.

7. Perrin, D. D.; Armarego, W. L. F. *Purification of Laboratory Chemicals*, 3rd ed.; Pergamon Press: Oxford, 1988.

8. Corriu, R. J. P.; Lancelle-Beltran, E.; Mehdi, A.; Reye, C.; Brandes, S.; Guilard, R. *Chem. Mat.* **2003**, *15*, 3152-3160.

9. Canali, L.; Cowan, E.; Deleuze, H.; Gibson, C. L.; Sherrington, D. C. *J. Chem. Soc., Perkin Trans. 1* **2000**, 2055-2066.

10. Ayala, V.; Corma, A.; Iglesias, M.; Rincon, J. A.; Sanchez, F. *J. Catal.* **2004**, *224*, 170-177.

11. Sharma, A. C.; Borovik, A. S. *J. Am. Chem. Soc.* **2000**, *122*, 8946-8955.

12. Lee, G. S.; Lee, Y. J.; Choi, S. Y.; Park, Y. S.; Yoon, K. B. *J. Am. Chem. Soc.* **2000**, *122*, 12151-12157.

13. Zhao, L.; Loy, D. A.; Shea, K. J. *J. Am. Chem. Soc.* **2006**, *128*, 14250-14251.

14. (a) Pui, A.; Berdan, I.; Morgenstern-Badarau, I.; Gref, A.; Perrée-Fauvet, M. *Inorg. Chim. Acta* **2001**, *320*, 167-171. (b) Hoshino, M.; Konishi, R.; Tezuka, N.; Ueno, I.; Seki, H. *J. Phys. Chem.* **1996**, *100*, 13569-13574.

15. (a) Works, C. F.; Ford, P. C. *J. Am. Chem. Soc.* **2000**, *122*, 7592-7593. (b) Odenkirk, W.; Rheingold, A. L.; Bosnich, B. *J. Am. Chem. Soc.* **1992**, *114*, 6392-6398.

16. (a) Rolison, D. R.; Dunn, B. *J. Mater. Chem.* **2001**, *11*, 963-980. (b) Husing, N.; Schubert, U. *Angew. Chem. Int. Ed.* **1998**, *37*, 22-45. (c) Barbe, C.; Bartlett, J.; Kong, L.; Finnie, K.; Lin, H. Q.; Larkin, M.; Calleja, S.; Bush, A.; Calleja, G. *Adv. Mater.* **2004**, *16*, 1959-1966.

17. (a) Jones, R. D.; Summerville, D. A.; Basolo, F. *Chem. Rev.* **1979**, *79*, 139-179. (b) Niederhoffer, E. C.; Timmons, J. H.; Martell, A. E. *Chem. Rev.* **1984**, *84*, 137-203. (c) Tovrog, B. S.; Kitko, D. J.; Drago, R. S. *J. Am. Chem. Soc.* **1976**, *98*, 5144-5153. (d) Getz, D.; Melamud, E.; Silver, B. L.; Dori, Z. *J. Am. Chem. Soc.* **1975**, *97*, 3846-3847.

18. Tsukahara, H.; Ishida, T.; Todoroki, Y.; Hiraoka, M.; Mayumi, M. *Free Radical Res.* **2003**, *37*, 171-177.

19. Franz, K. J.; Lippard, S. J. *J. Am. Chem. Soc.* **1999**, *121*, 10504-10512.

20. (a) Franz, K. J.; Doerrer, L. H.; Spingler, B.; Lippard, S. J. *Inorg. Chem.* **2001**, *40*, 3774-3780. (b) Hilderbrand, S. A.; Lippard, S. J. *Inorg. Chem.* **2004**, *43*, 4674-4682.

CHAPTER SIX

CONCLUSIONS AND RECOMMENDATIONS

Conclusions

The overall goal of this dissertation work was to develop nanomaterials that interact with nitric oxide (NO) and study their chemical and physical properties. Precipitation with compressed antisolvent (PCA) technology is one of a few convenient methods for the preparation of nano-sized particles composed entirely of molecules. While only some initial analytical and spectroscopic results were reported for nanoparticulate metal complexes ($[M^{II}(salen)]_P$) produced by PCA technology,[1] additional studies were required to determine their chemical and physical properties. This dissertation presents microscopic and diffraction data that helped determine the molecular structure of the molecules within the nanoparticles. A compliment of spectroscopic, analytical, and diffraction data were utilized to investigate the chemical properties of the nanoparticles. Finally, the preparative routes for the synthesis of new metal complexes were described for immobilization within silica particles.

The work described in Chapter 2 provides support for the notion that the metal complex nanoparticles form lamellar (layered) structures during processing. While images from microscopy provided some evidence for the formation of lamellar structures, the strongest support came from powder X-ray diffraction (PXRD). The

PXRD data for $[Ni^{II}(salen)]_P$ and $[Co^{II}(salen)]_P$ were identical. These diffraction patterns were similar to the patterns found for unprocessed $Ni^{II}(salen)$, which means that the crystalline structures of these three metal complexes are similar. Since the major diffraction peaks at approximately 11.6° are associated with an interplanar distance of 7.5 Å, it is proposed that the crystalline structure along the c-axis forms the layers within the nanoparticles.

It was also found that these metal complex nanoparticles display unique function for O_2 binding and NO disproportionation when compared to their molecular analogs. When $[Co^{II}(salen)]_P$ is exposed to dioxygen in a Rubotherm magnetic suspension balance, a mass increase of 5.1% is observed, resulting in the formation of bridging peroxo complexes within the nanoparticles.[2] This finding further supports the lamellar structure of the nanoparticles because the crystallinity of $[Co^{II}(salen)]_P$ is preserved after the nanoparticles are exposed to dioxygen. The nanoparticles also catalyze the disproportionation of NO at room temperature, which is unique because other systems that disproportionate NO in the solid state require elevated temperatures. The NO reactivity in $[Co^{II}(salen)]_P$ is partly due to its four-coordinate nature; however, the cause(s) of how the disproportionation products stay absorbed within the nanoparticles is not understood.

Finally, various alkoxysilyl salen metal complexes have been synthesized and immobilized within silica particles. Initial immobilization studies have incorporated cobalt complexes within sub-micron silica particles. Even though these cobalt-containing particles are larger than anticipated, the preparative routes described in this

dissertation provide a good foundation for the future production of immobilized metal complexes within silica nanoparticles.

Recommendations

The findings in this dissertation provide several opportunities for different research investigations and applications. In order to further support the PXRD analysis, one immediate short-term investigation involves obtaining electron diffraction data using transmission electron microscopy. When the nanoparticles are sonicated, their structure begins to break apart and become thinner. Therefore, an electron diffraction pattern can be obtained on the sonicated samples and compared to the PXRD data. Another investigation involves using PXRD to determine the structure of the nanoparticles through the Rietveld method, which uses least squares anaylsis on specially collected diffraction data.[3]

The Rietveld analysis could also be useful in determining how the molecular structure of the nanoparticle changes after $[Co^{II}(salen)]_P$ is exposed to NO. The results obtained in Chapter 3 suggest that $[Co^{II}(salen)]_P$ could be a potential catalyst for the removal of NO_X emissions, but the nanoparticles were exposed to pure NO, which is not representative of actual combustion conditions. Another short-term project could involve exposing $[Co^{II}(salen)]_P$ to a mixture of combustion gases to determine its viability as a catalyst for the reduction of toxic emissions from automobiles.

Another project could involve studying the viability of $[Co^{II}(salen)]_P$ as a system for the storage and release of NO. Preliminary experiments have shown that

$[Co^{II}(salen)]_P$ interacts differently with NO when the gas is mixed with an inert gas, lowering its concentration (~5% in He).[4] A mass change of approximately 11% is observed,[5] and no disproportionation products are observed by infrared spectroscopy (Figure 6-1). The appearance of a broad band at 1639 cm^{-1} provides evidence for the formation of a nitrosyl complex, which is similar to other cobalt nitrosyl complexes reported in literature.[6] These nanoparticulate nitrosyl complexes have not been explored and may prove to be an effective NO-releasing system.

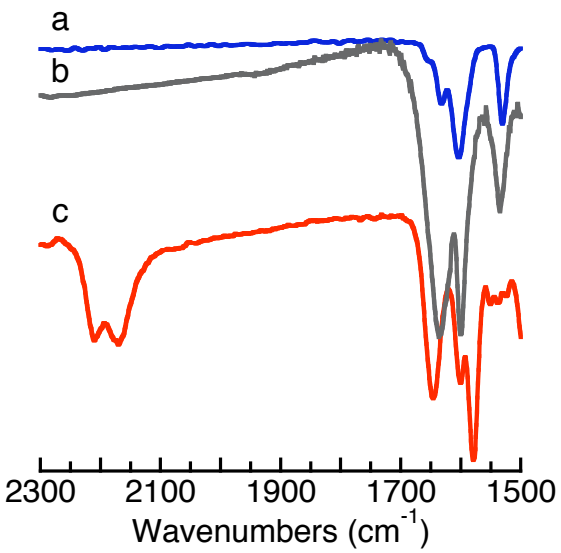

Figure 6-1. FTIR spectra (KBr pellets) of (a) $[Co^{II}(salen)]_P$ (—), (b) $[Co^{II}(salen)]_P$ + dilute NO (—), and (c) $[Co^{II}(salen)]_P$ + concentrated NO (—).

Finally, there are several opportunities for a number of short and long-term investigations involving the development of immobilized cobalt complexes within silica nanoparticles. One short-term project involves improving the synthetic procedure for the formation of Co^{II}**1A**-SP because there are some difficulties with the copolymerization of Co^{II}**1A** with tetraethylorthosilicate (TEOS). Since Co^{II}**1A** is

copolymerized with TEOS in methanol, the cobalt sites can readily become oxidized while the particles are washed. If the oxidation of these cobalt complexes can be prevented, then these cobalt-containing silica particles could be used as a NO storage and release system.

Another short-term project involves preparing metal salen complexes that contain smaller alkoxysilyl functional groups since the bulky isopropoxysilyl functional groups on Co^{II}**1A** make it difficult to form smaller silica particles. The smaller alkoxysilyl functional groups are more reactive and may provide a better platform for the formation of silica-based nanoparticles. The smaller alkoxysilyl functional groups may also increase the solubility of metal complexes in methanol, which is highly desirable during the copolymerization synthesis.

A long-term project involves probing the applicability of nanoparticulate metal complexes by coating them onto various substrates using supercritical carbon dioxide. Some preliminary studies coating $[Co^{II}(salen)]_P$ onto various supports have been performed, but the coating efficiencies were low.[5] One way to improve the coating efficiencies is to covalently bind the nanoparticulate metal complexes to the substrate. The alkoxysilyl salen metal complexes can readily be used for this study because the alkoxysilyl functional groups may hydrolyze and attach to glass and alumina substrates.

References

1. Johnson, C. A.; Sharma, S.; Subramaniam, B.; Borovik, A. S. *J. Am. Chem. Soc.* **2005**, *127*, 9698-9699.

2. Johnson, C. A.; Ottiger, S.; Pini, R.; Gorman, E.; Nguyen, J. G.; Munson, E.; Mazzotti, M.; Borovik, A. S.; Subramaniam, B. *AIChE J.* accepted pending minor revisions.

3. *The Rietveld Method*; Young, R. A., Ed.; Oxford University Press: Oxford, 1995.

4. The uptake profile was performed by Dr. Chad Johnson and reported in Reference 5.

5. Johnson, C. A. Ph.D. Thesis, University of Kansas, Lawrence, KS, 2008.

6. Clarkson, S. G.; Basolo, F. *Inorg. Chem.* **1973**, *12*, 1528-1534.

APPENDIX A

SUPPLEMENTAL INFORMATION FOR CHAPTER 3

Figure A-1. Picture of the NO-labeling study set-up.

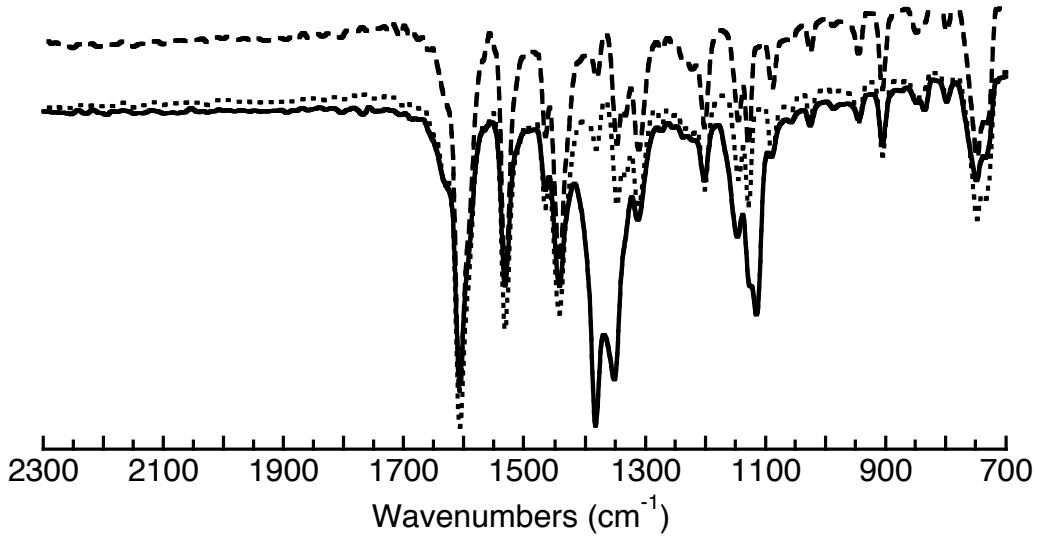

Figure A-2. FTIR spectra (KBr pellet) of (a) $[Co^{II}(salen)]_P$ (—), (b) N_2O-exposed $[Co^{II}(salen)]_P$ (- - -), and (c) N_2-exposed $[Co^{II}(salen)]_P$ (. . .).

APPENDIX B

SUPPLEMENTAL INFORMATION FOR CHAPTER 4

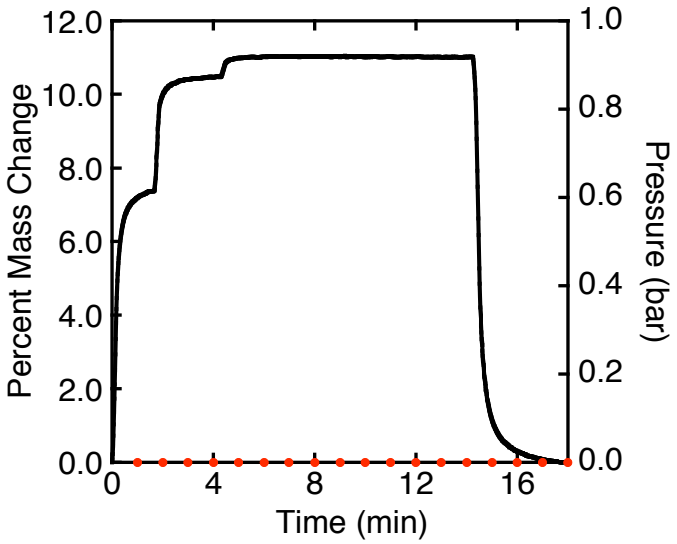

Figure B-1. TEOM profile for O_2 uptake by unprocessed Co^{II}(salen) with variable O_2 flow rates. Red dots are the corresponding pressure profiles.

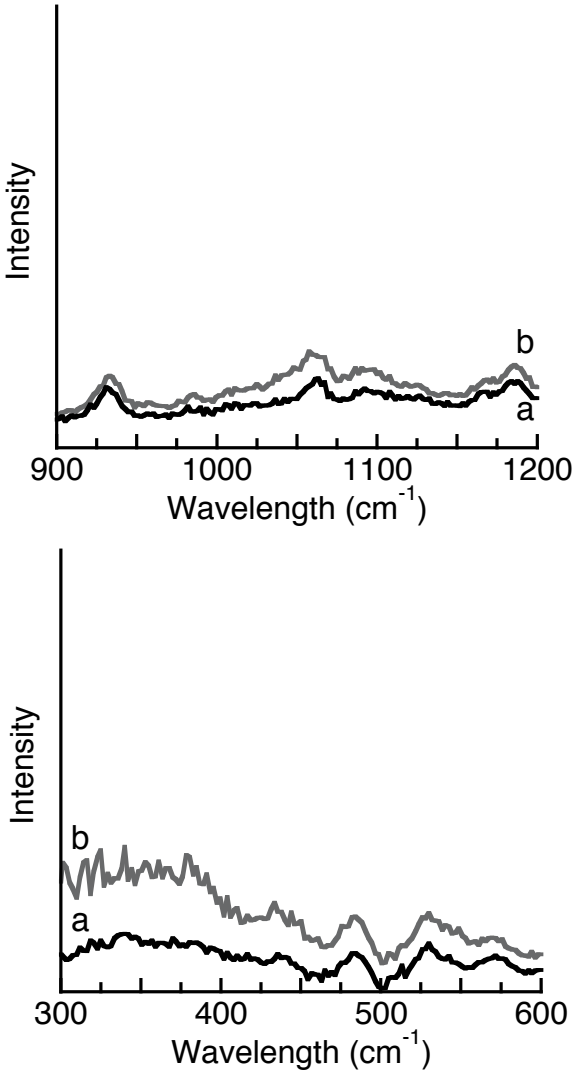

Figure B-2. Raman spectra (KBr pellets) of (a) Unprocessed Co^{II}(salen) (—) and (b) Unprocessed Co^{II}(salen) + O_2 (—)

APPENDIX C

SUPPLEMENTAL INFORMATION FOR CHAPTER 5

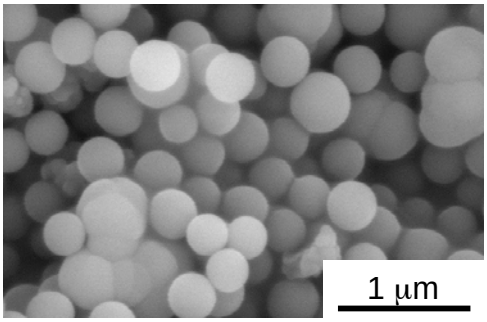

Figure C-1. SEM micrographs of silica nanoparticles polymerized without metal complexes.

Appendix D: TEOM O_2 Data

brown = fresh nanoparticles
green = nanoparticles exposed to air first

Sample	Run	Batch	notebook p	Sample Gas	Carrier Gas	Purge Gas	Carrier Gas	Carrier Tank Pressure	Carrier Tank Pressure	Sample Gass Rotometer
						(sccm)	(sccm)	(psig)	(atm)	
Unp Co(salen)	20	Aldrich (07522KD)	236b	O_2	He	21.5	13.7	45	4.06	16
$[Co(salen)]_P$	21	Co Run 3 filter (green)	237b	O_2	He	21.5	13.7	45	4.06	15
$[Co(salen)]_P$	22	Co Run 6 (brown)	238b	O_2	He	21.5	13.9	45	4.06	20
$[Ni(salen)]_P$	51	Ni Run 7 chamber	272b	O_2	He	15.4	15	50	4.40	15
$[Co(salen)]_P$	53	Co Run 7 filter brown	273b	O_2	He	15.4	15	50	4.40	17
$[Co(salen)]_P$	55	Co Run 7 filter brown	276b	O_2	He	15.4	15	50	4.40	14
$[Co(salen)]_P$	56	Co Run 7 filter brown	278b	O_2	He	15.4	15	50	4.40	15
Unp Co(salen)	57	Aldrich (07613CE)	JGN-C105	O_2	He	15.4	15	50	4.40	15
$[Ni(salen)]_P$	58	Ni Run 7 filter	279b	O_2	He	15.4	15	50	4.40	15
$[Ni(salen)]_P$	59	Ni Run 7 filter	279b	O_2	He	15.4	15	50	4.40	16
$[Ni(salen)]_P$	60	Ni Run 7 filter	279b	O_2	He	15.4	15	50	4.40	16
$[Ni(salen)]_P$	61	Ni Run 7 filter	280b	O_2	He	15.3	15	50	4.40	15
$[Ni(salen)]_P$	62	Ni Run 7 filter	JGN-C110	O_2	He	15.3	15	50	4.40	15
$[Ni(salen)]_P$	63	Ni Run 7 filter	JGN-C111	O_2	He	15.3	15	50	4.40	15
$[Co(salen)]_P$	64	Co Run 7 filter brown	281b	O_2	He	15.4	15	50	4.40	15
$[Ni(salen)]_P$	65	Ni Run 7 filter	282b	O_2	He	15.4	15	50	4.40	15
$[Ni(salen)]_P$	66	Ni Run 7 filter	JGN-C115	O_2	He	15.4	15	50	4.40	15
Unp Co(salen)	67	Aldrich (07613CE)	JGN-C116	O_2	He	15.4	15	50	4.40	15
Unp Co(salen)	68	Aldrich (07613CE)	JGN-C117	O_2	He	15.3	15	50	4.40	15
Unp Co(salen)	69	Aldrich (07613CE)	JGN-C118	O_2	He	15.4	15	50	4.40	15
Quartz	70	Ref Material 130	JGN-C119	O_2	He	15.4	15	50	4.40	15
Quartz	71	Ref Material 130	JGN-C120	O_2	He	15.4	15	50	4.40	15
$[Co(salen)]_P$	72	Co Run 7 filter brown	JGN-C121	O_2	He	15.4	15	50	4.40	15
$[Co(salen)]_P$	73	Co Run 7 filter brown	JGN-C122	O_2	He	15.4	15	50	4.40	15
$[Co(salen)]_P$	74	Co Run 7 filter brown	288b	O_2	He	15.4	15	50	4.40	15
$[Co(salen)]_P$	75	Co Run 7 filter brown	JGN-C124	O_2	He	15.4	15	50	4.40	15
Unp Co(salen)	76	Aldrich (07613CE)	JGN-C125	O_2	He	15.4	15	50	4.40	15
Unp Co(salen)	77	Aldrich (07613CE)	JGN-C126	O_2	He	15.4	15	50	4.40	15
Quartz	78	Ref Material 130	JGN-C127	O_2	He	15.4	15	50	4.40	15

Appendix E: NMR Spectra for Chapter 5

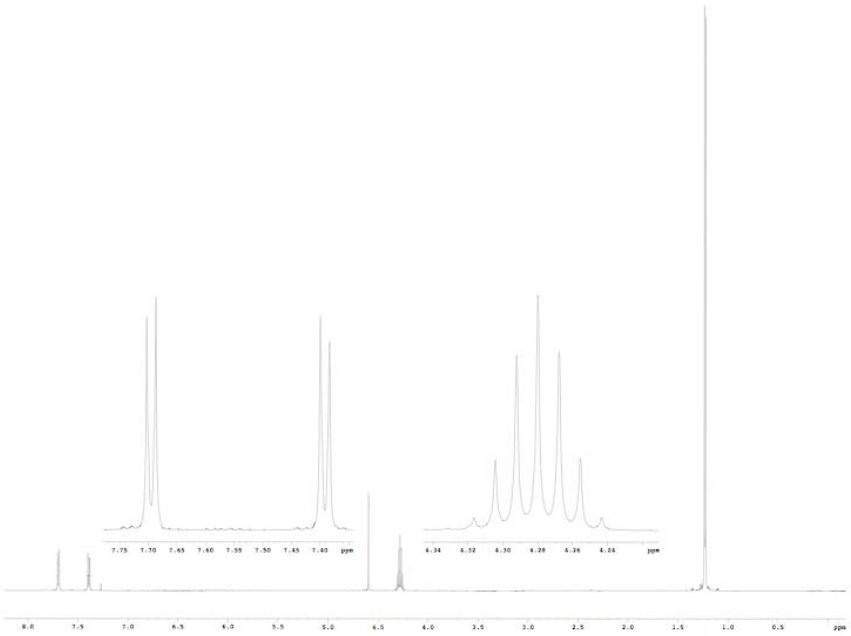

^{1}H NMR spectrum for **2A**

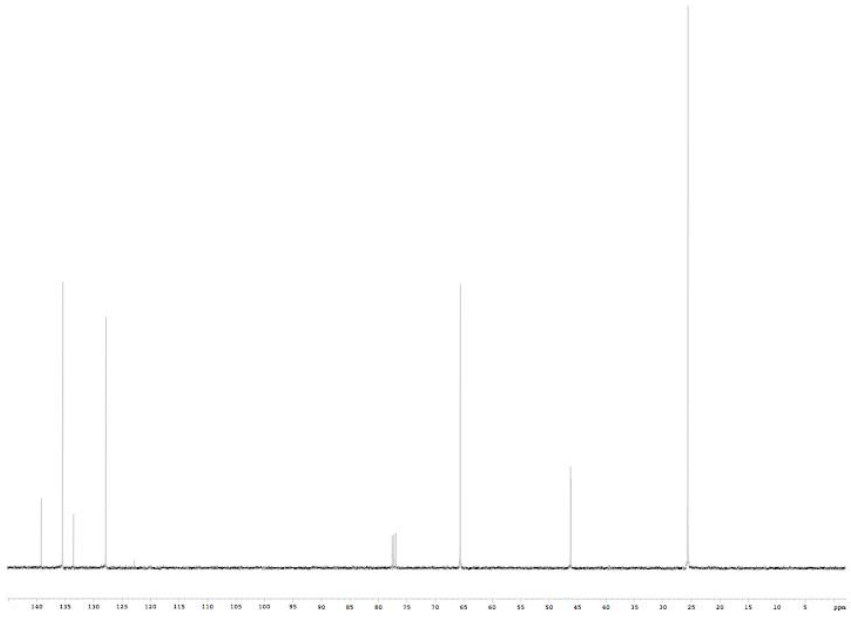

^{13}C NMR spectrum for **2A**

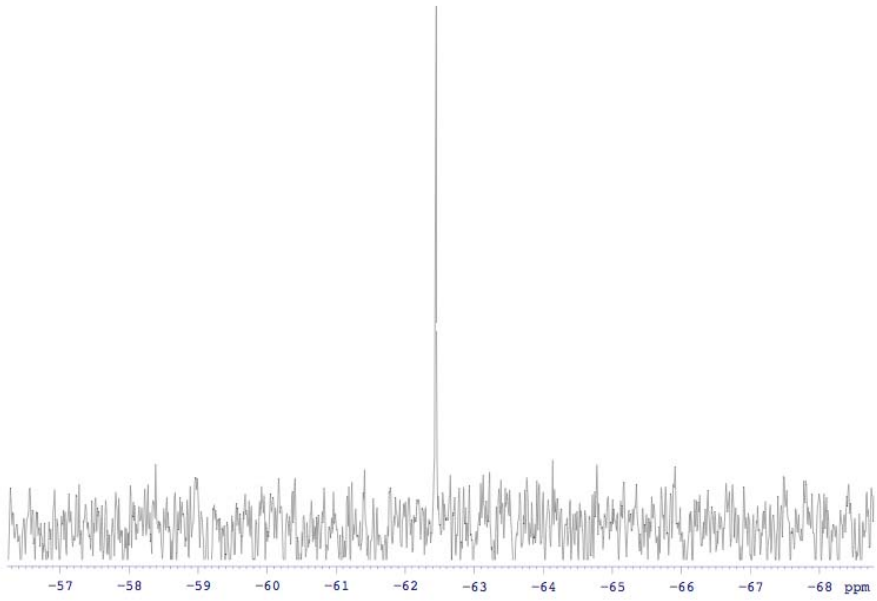

^{29}Si NMR spectrum for **2A**

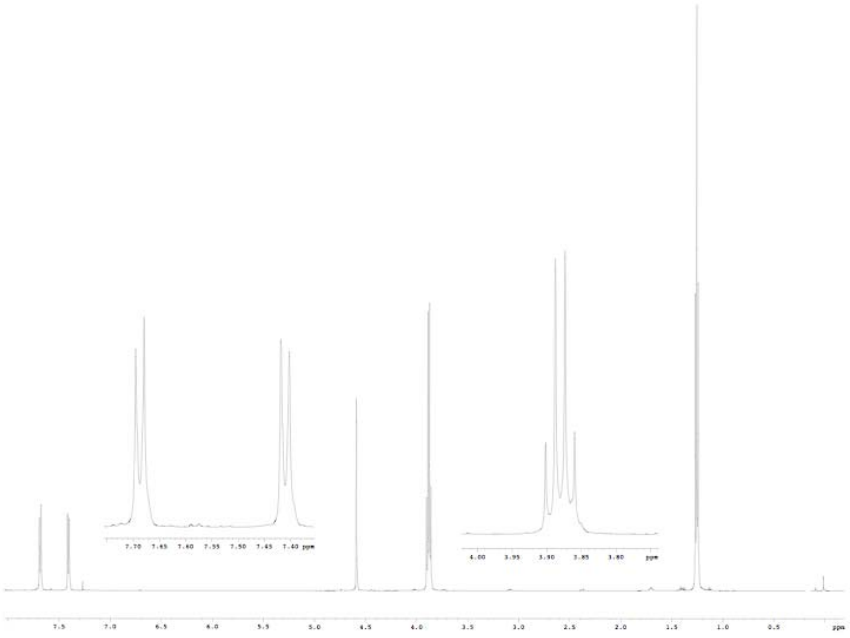

^{1}H NMR spectrum for **2B**

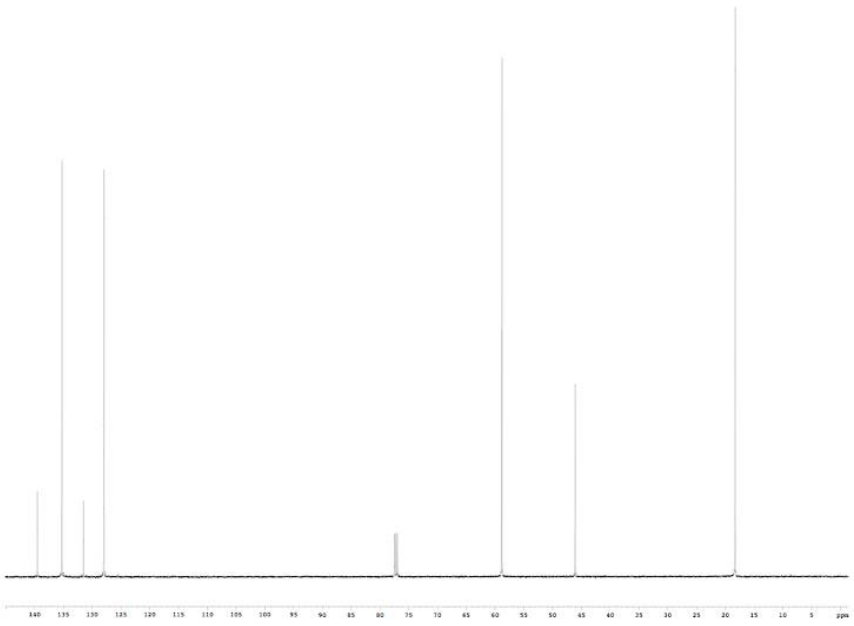

^{13}C NMR spectrum for **2B**

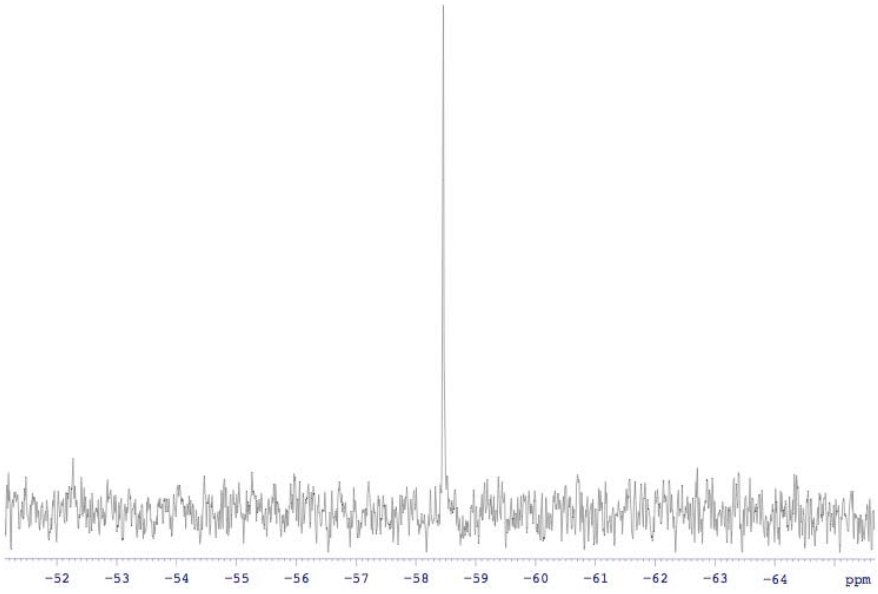

^{29}Si NMR spectrum for **2B**

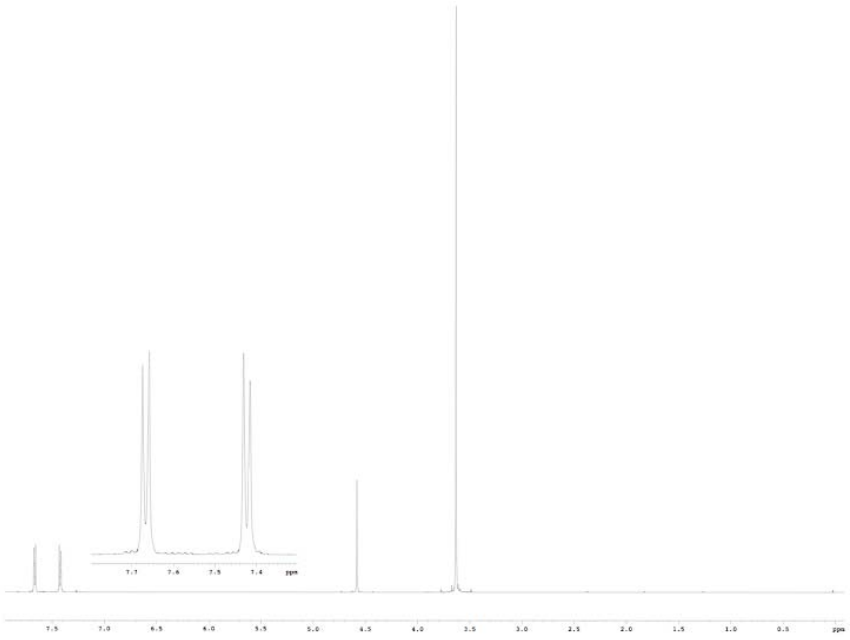

^{1}H NMR spectrum for **2C**

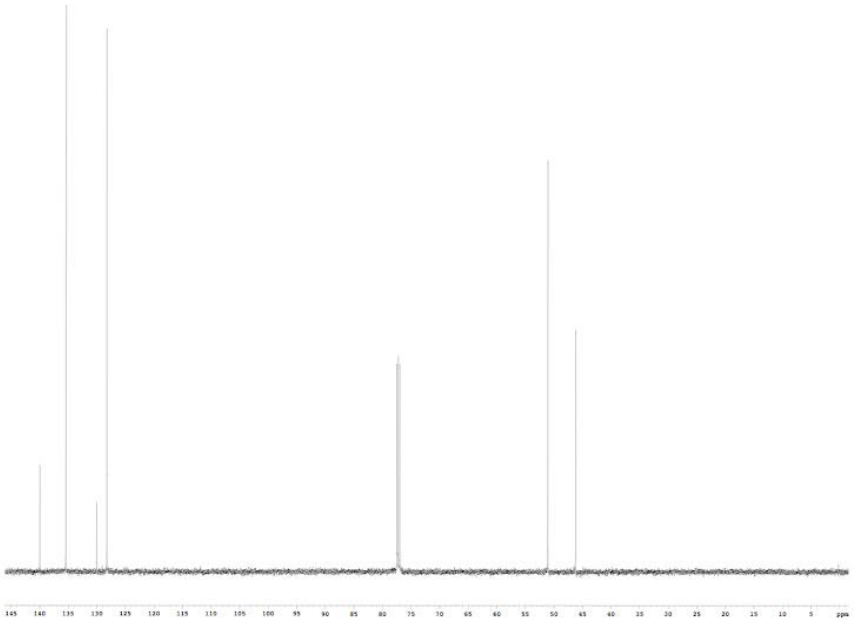

^{13}C NMR spectrum for **2C**

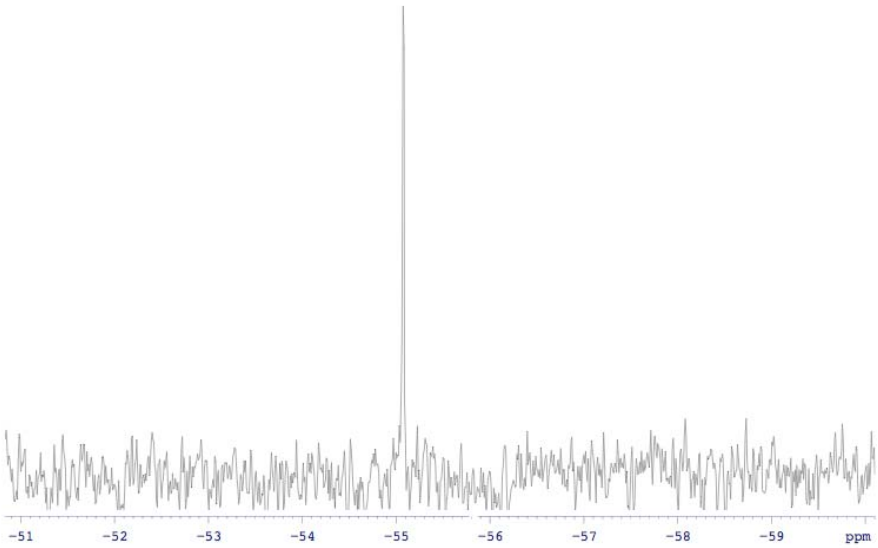

^{29}Si NMR spectrum for **2C**

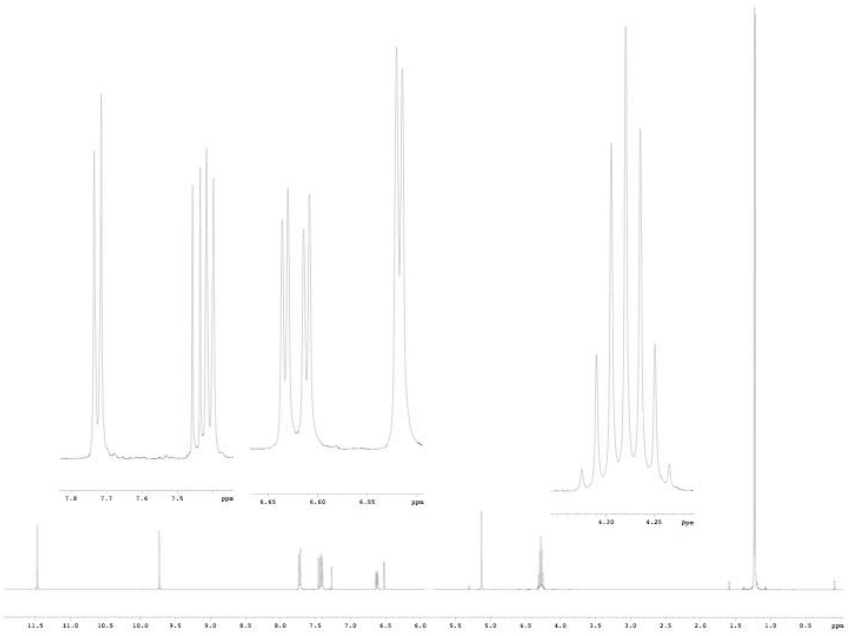

^{1}H NMR spectrum for **3A**

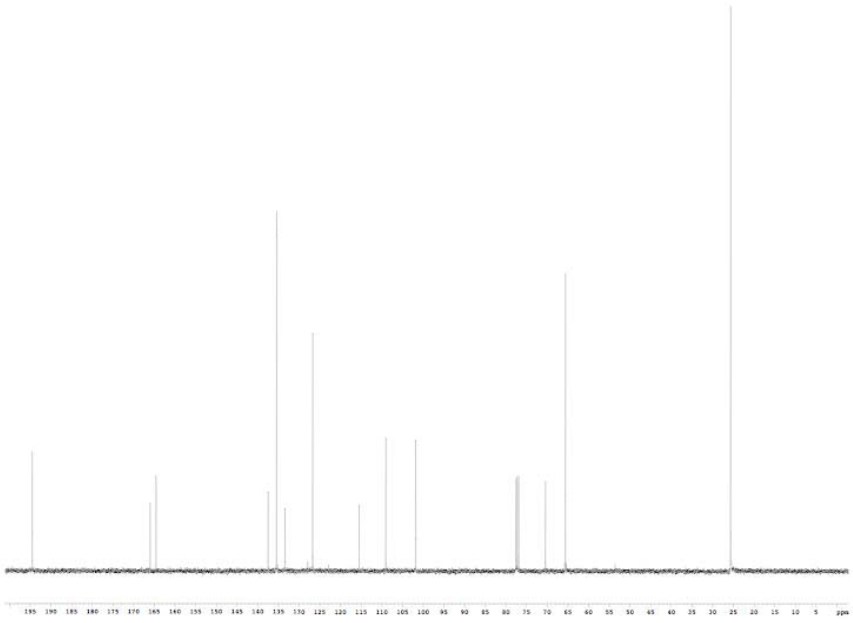

^{13}C NMR spectrum for **3A**

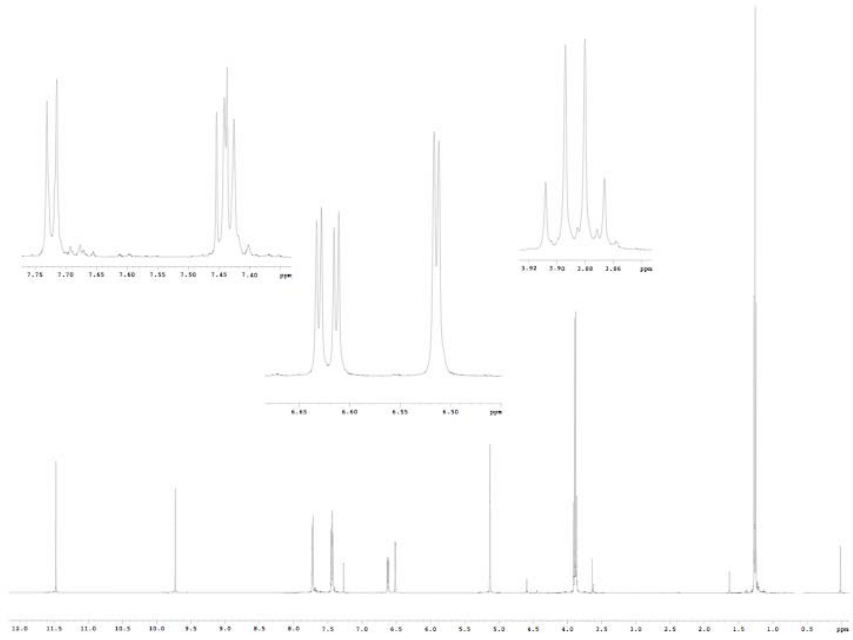

^{1}H NMR spectrum for **3B**

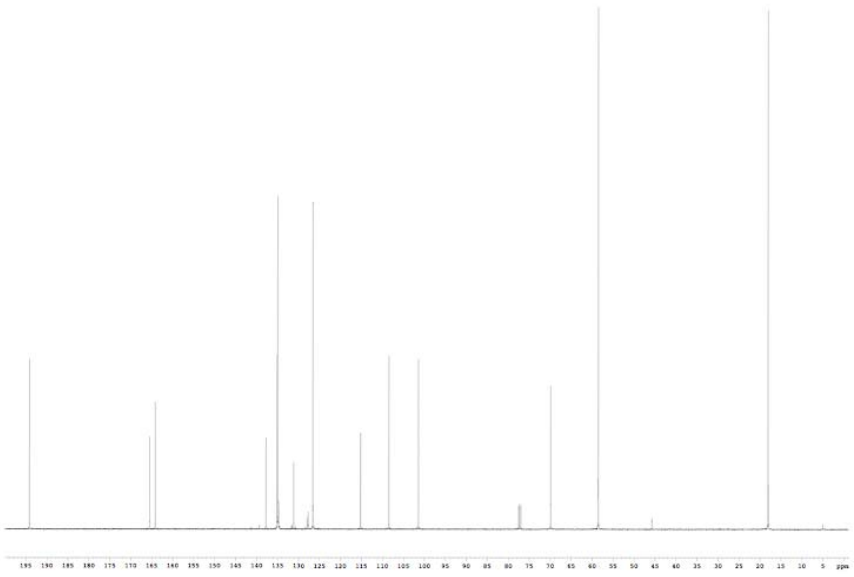

^{13}C NMR spectrum for **3B**

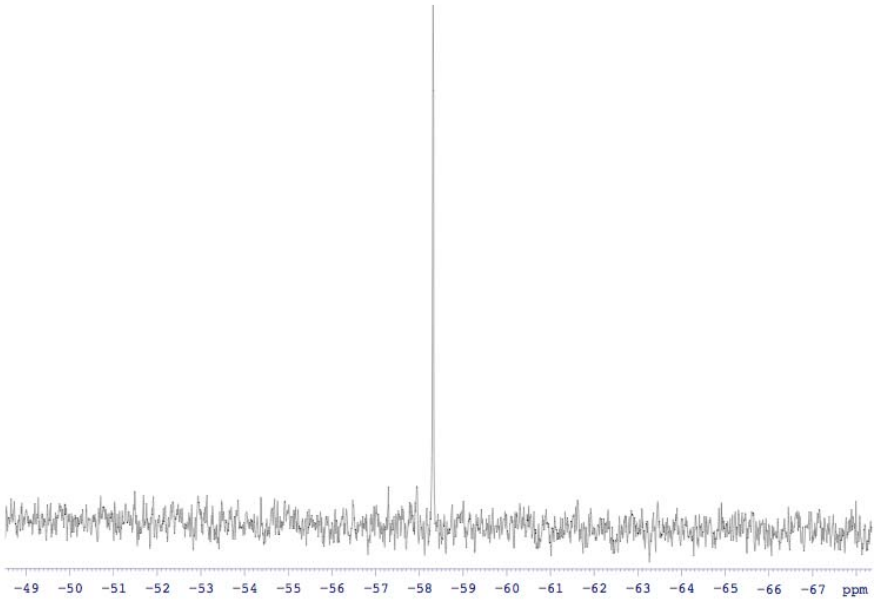

^{29}Si NMR spectrum for **3B**

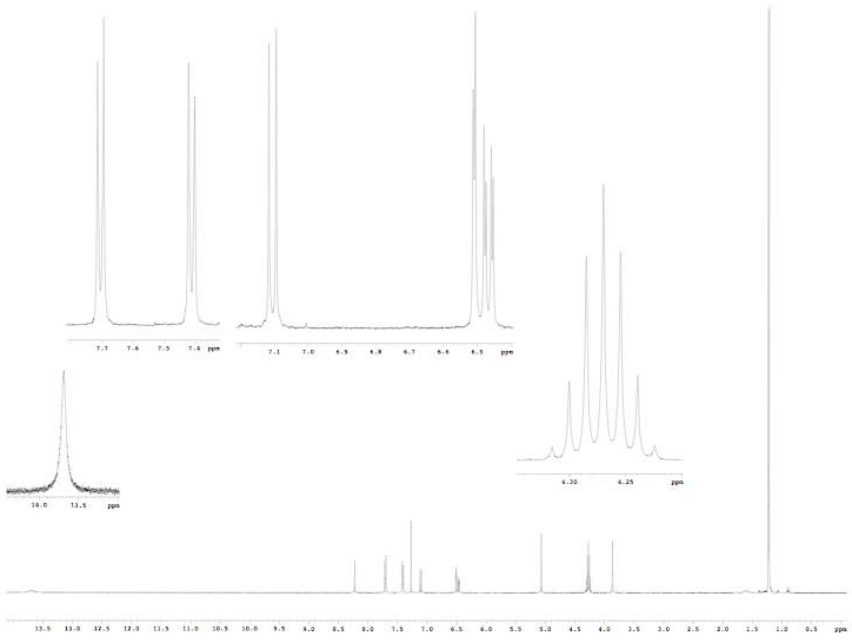

^{1}H NMR spectrum for H_2**1A**

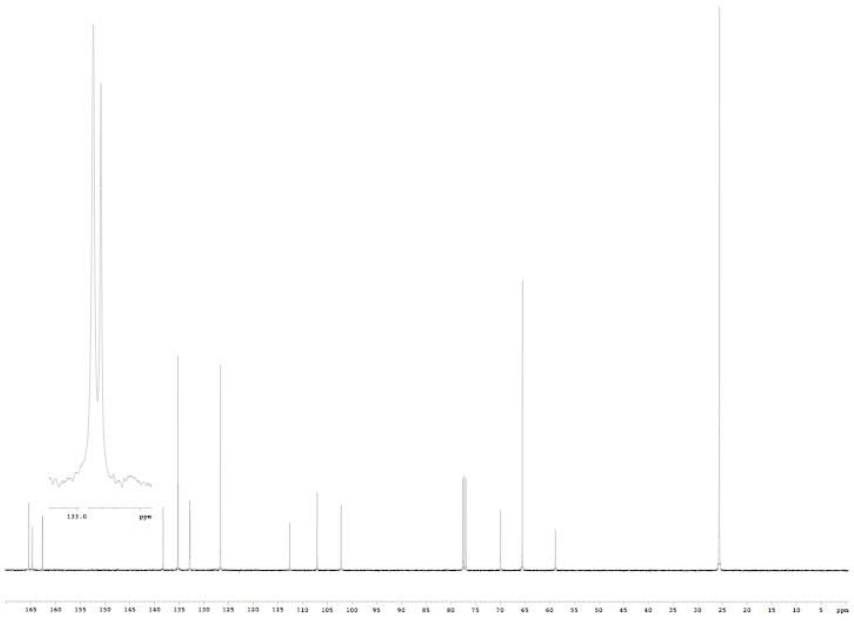

^{13}C NMR spectrum for H_2**1A**

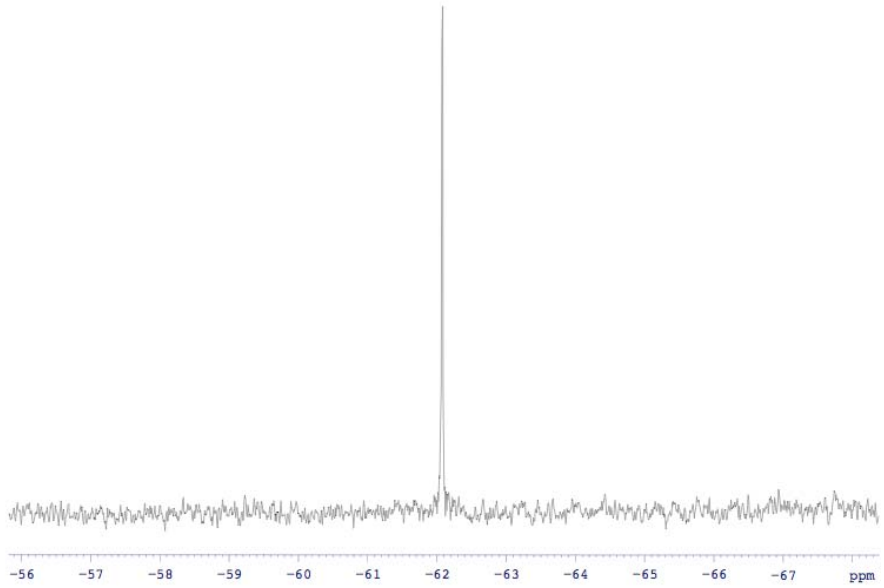

^{29}Si NMR spectrum for H_2**1A**

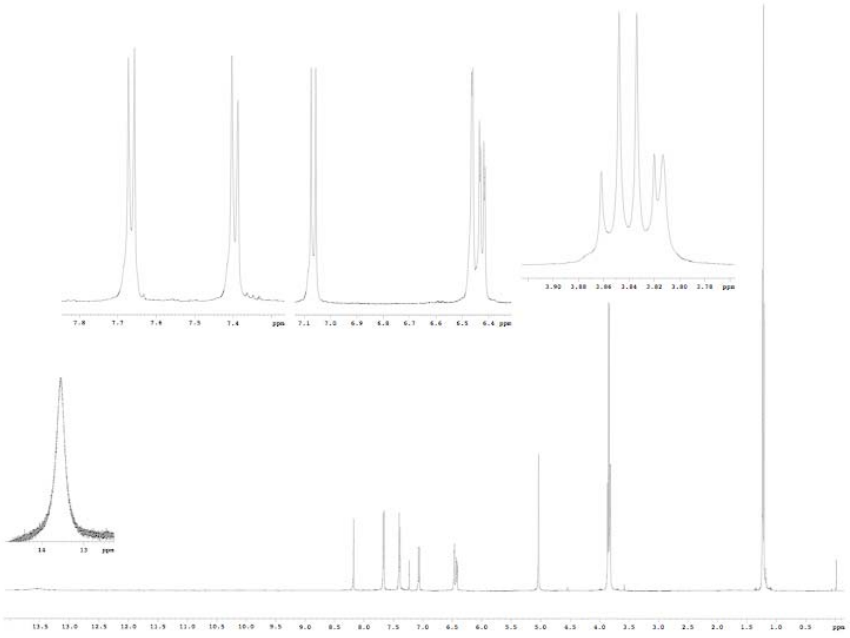

^{1}H NMR spectrum for H_2**1B**

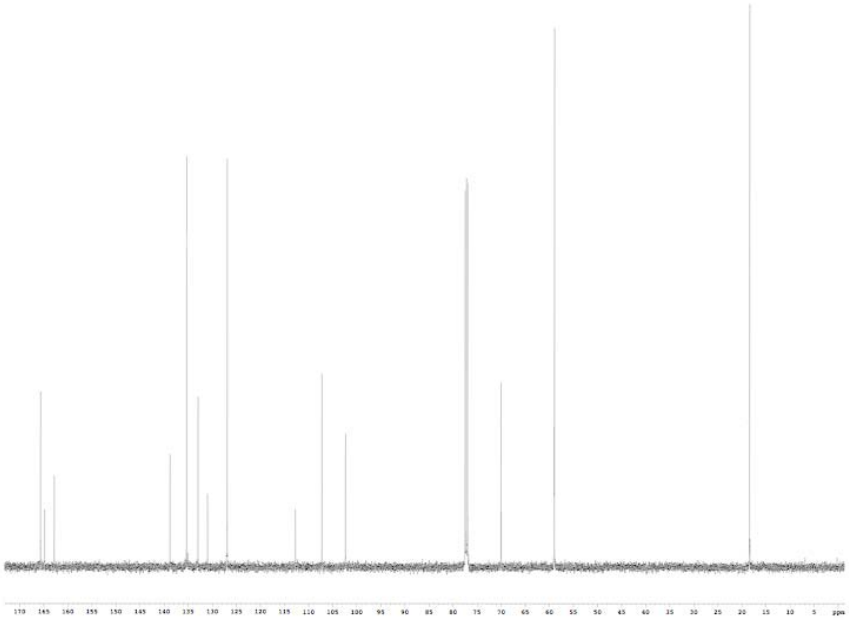

^{13}C NMR spectrum for H_2**1B**

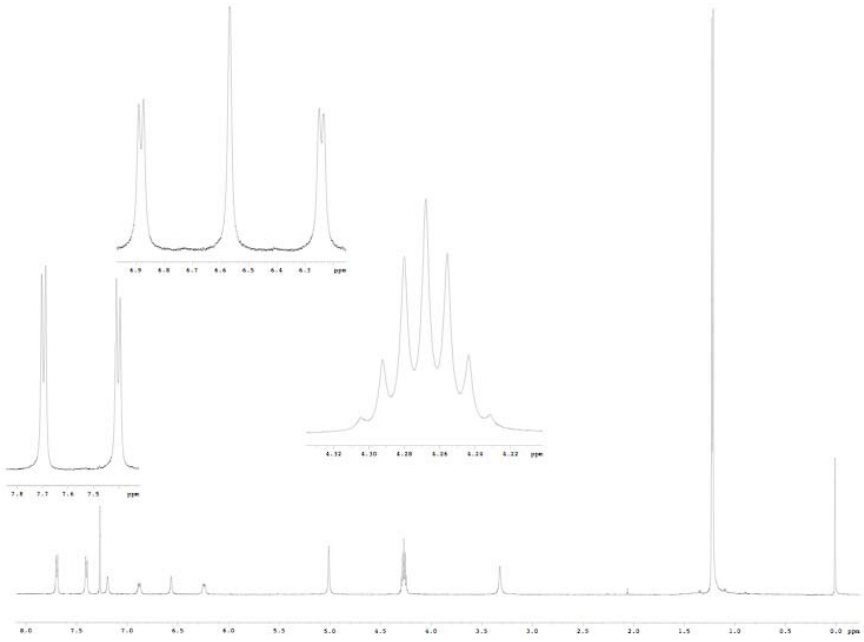

^{1}H NMR spectrum for Ni^{II}**1A**

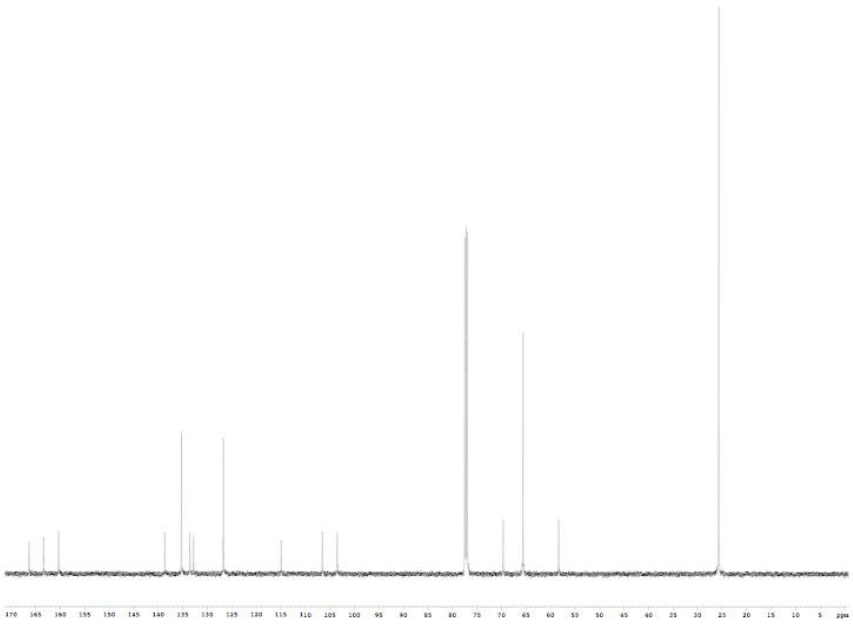

^{13}C NMR spectrum for Ni^{II}**1A**

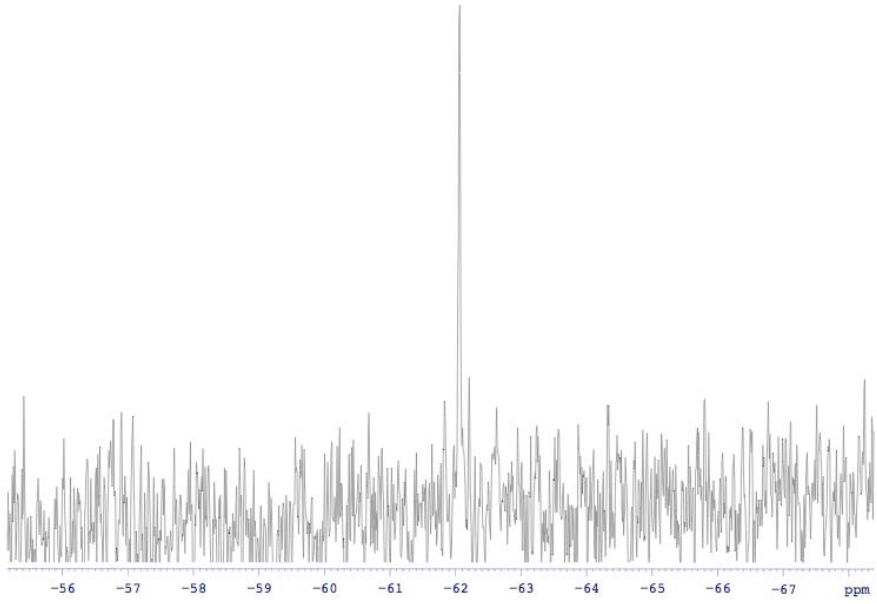

^{29}Si NMR spectrum for Ni^{II}**1A**

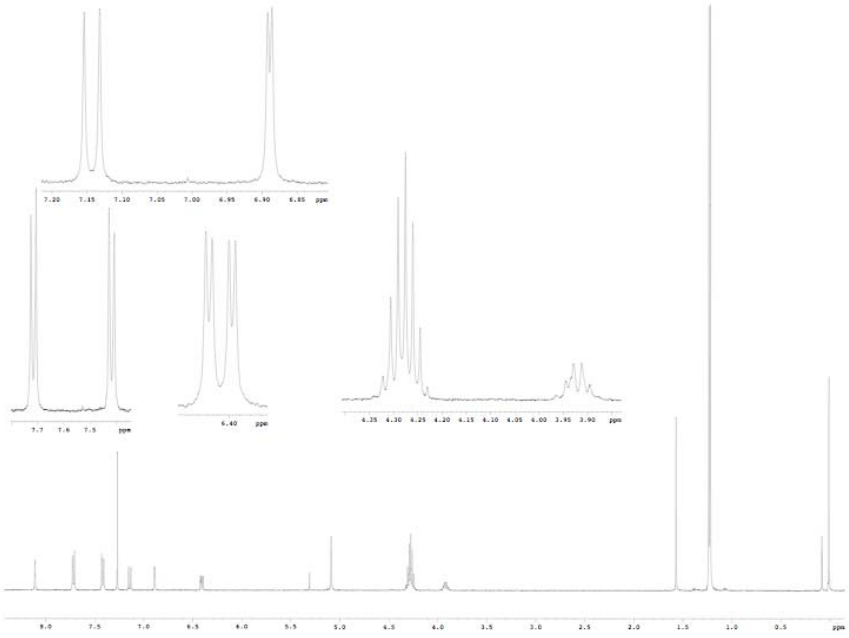

^{1}H NMR spectrum for Ru**1A**(NO)(Cl)

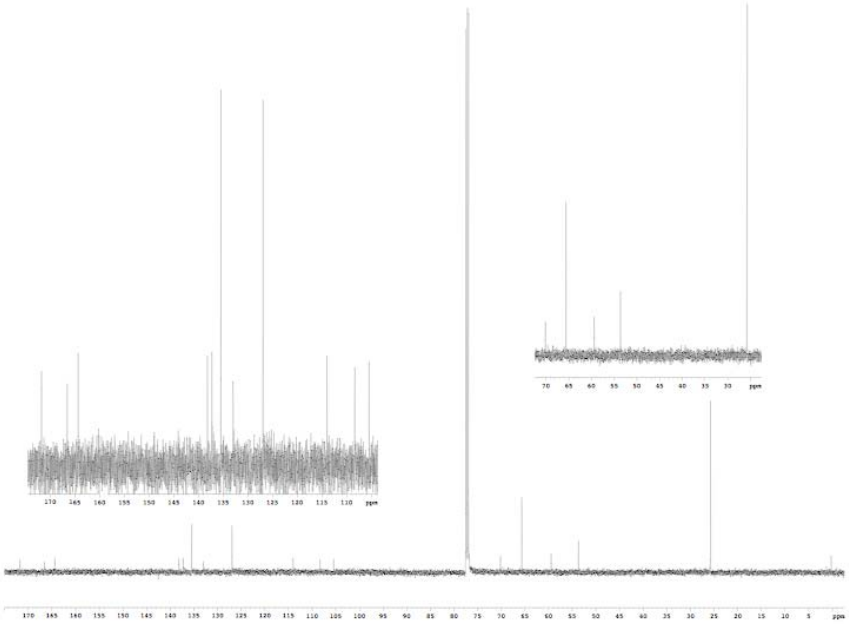

^{13}C NMR spectrum for for Ru**1A**(NO)(Cl)